DEVELOPMENT AND VERIFICATION OF THE NON-LINEAR CURVATURE WAVEFRONT SENSOR

by

Mala Mateen

A Dissertation Submitted to the Faculty of the

DEPARTMENT OF OPTICAL SCIENCES

In Partial Fulfillment of the Requirements
For the Degree of

DOCTOR OF PHILOSOPHY

In the Graduate College

THE UNIVERSITY OF ARIZONA

2015

The University of Arizona
Graduate College

As members of the Dissertation Committee, we certify that we have read the dissertation prepared by Mala Mateen, titled The Development and Verification of the Non-Linear Curvature Wavefront Sensor and recommend that it be accepted as fulfilling the dissertation requirement for the Degree of Doctor of Philosophy.

Olivier Guyon Date: May 12, 2015

Michael Hart Date: May 12, 2015

José Sasián Date: May 12, 2015

Final approval and acceptance of this dissertation is contingent upon the candidates submission of the final copies of the dissertation to the Graduate College. I hereby certify that I have read this dissertation prepared under my direction and recommend that it be accepted as fulfilling the dissertation requirement.

Dissertation Director: Olivier Guyon Date: May 12, 2015

Dissertation Director: Michael Hart Date: May 12, 2015

STATEMENT BY AUTHOR

This dissertation has been submitted in partial fulfillment of the requirements for an advanced degree at the University of Arizona and is deposited in the University Library to be made available to borrowers under rules of the Library.

Brief quotations from this dissertation are allowable without special permission, provided that an accurate acknowledgement of the source is made. Requests for permission for extended quotation from or reproduction of this manuscript in whole or in part may be granted by the copyright holder.

SIGNED: Mala Mateen

Acknowledgments

I am indebted to my advisors Olivier Guyon and Michael Hart for their guidance during the completion of this dissertation.

It has been an honor and a privilege to work with someone of Olivier's caliber. Every conversation with him has been full of boundless insights into optical phenomenon, wavefront sensing, and adaptive optics. Many of which I would have to mull over long periods of time and re-visit to comprehend in their entirety. I am grateful to Olivier for assigning me a well-defined research topic and allowing me the freedom to mold it in my own vision. With out Olivier's foresight, expertise, enthusiasm, and availability for 6 a.m. meetings, among other things, this research would not have been possible.

I will always cherish my at-the-board sessions with Michael which taught me how to understand and answer a problem. He truly taught me the meaning of feeling adaptive optics in my bones. Above all I am grateful for the faith Michael had in my ability to carry out this dissertation as it unfolded and seeped through the various crevices, nooks, and crannies which underlie a graduate education.

I am grateful to the the National Science Foundation (NSF), and to the Air Force Research Lab, in particular to the Starfire Optical Range (SOR) for their support. With out the tremendous, undeterred, support of people like Earl Spillar and Robert Johnson it would not have been possible for me to pursue this degree. I do not have words to thank Robert for the compassion and unrelenting support he has offered me through my educational tenure. Co-workers like Lee Kann, Josh Kann, Dan Roskey, Loretta Arguello, Andrea Tuffli, Michael Oliker, Michael Sichler, and Regina Hearn not only helped me with my research project but have been a pleasure to work with.

My laboratory setup was in Steward Observatory and there were key personnel there that ensured that my research would continue without major road blocks. I am grateful to the support I received from Kimberly Chapman, Manny Montoya, Vidhya Vaitheeswaran, and Johanan Codona.

I could not have asked for a better education than the one I received at the College of Optical Sciences. It has been a pleasure to have been the pupil of professors like Tom Milster, Scott Tyo, and Masud Mansuripur. I can truly say that I would not be writing these words in conclusion of a dissertation was it not for the belief Professor Mansuripur had in me. It is a treasured rarity to come across as brilliant a teacher as Professor Mansuripur and have him believe in your ability. My graduate experience would have been dry and incomplete was it not for my colorful classmates which made the demands of graduate school bearable. I will forever cherish the friendships fostered with Cecile, Esen, Anael, Stacey, and Eduardo.

I want to thank my family for their commitment in supporting my educational pursuit. This graduate path was envisioned by my father and completed as a result of my mother's dedication and perseverance. I have been heartened by the encouragement offered by my in-laws. In the most discouraging of times it was the thought of my daughter, Mysha's impressionable, future glance upon me that kept me going. Most importantly, I would not have been able to dedicate the time and commitment this work demanded without the support and understanding of my husband. The time spent on this dissertation was borrowed time from my family and I now look forward to returning that time to them.

Dedicated to:
Mysha - my 'world', my 'heaven', my 'eternity', when I hold you it's as if I hold 'infinity in the palm of my hand'.

TABLE OF CONTENTS

TABLE OF CONTENTS—*Continued*

LIST OF FIGURES

LIST OF FIGURES—*Continued*

LIST OF TABLES

Abstract

Adaptive optics (AO) systems have become an essential part of ground-based telescopes and enable diffraction-limited imaging at near-IR and mid-IR wavelengths. For several key science applications the required wavefront quality is higher than what current systems can deliver. For instance obtaining high quality diffraction-limited images at visible wavelengths requires residual wavefront errors to be well below 100 nm RMS. High contrast imaging of exoplanets and disks around nearby stars requires high accuracy control of low-order modes that dominate atmospheric turbulence and scatter light at small angles where exoplanets are likely to be found. Imaging planets using a high contrast coronagraphic camera, as is the case for the Spectro-Polarimetric High-contrast Exoplanet Research (SPHERE) on the Very Large Telescope (VLT), and the Gemini Planet Imager (GPI), requires even greater wavefront control accuracy.

My dissertation develops a highly sensitive non-linear Curvature Wavefront Sensor (nlCWFS) that can deliver diffraction-limited (λ/D) images, in the visible, by approaching the theoretical sensitivity limit imposed by fundamental physics. The nlCWFS is derived from the successful curvature wavefront sensing concept but uses a non-linear reconstructor in order to maintain sensitivity to low spatial frequencies. The nlCWFS sensitivity makes it optimal for extreme AO and visible AO systems because it utilizes the full spatial coherence of the pupil plane as opposed to conventional sensors such as the Shack-Hartmann Wavefront Sensor (SHWFS) which operate at the atmospheric seeing limit (λ/r_0). The difference is equivalent to a gain of $(D/r_0)^2$ in sensitivity, for the lowest order mode, which translates to the nlCWFS requiring that many fewer photons. When background limited the nlCWFS sensitivity scales as D^4, a combination of D^2 gain due to the diffraction limit and D^2 gain due to telescope's collecting power. Whereas conventional wavefront sensors only benefit from the D^2 gain due to the telescope's collecting power. For a 6.5 m telescope, at 0.5 m, and seeing of 0.5, the nlCWFS can deliver for low order modes the same wavefront measurement accuracy as the SHWFS with 1000 times fewer photons. This is especially significant for upcoming extremely large telescopes such as the Giant Magellan Telescope (GMT) which has a

25.4 m aperture, the Thirty Meter Telescope (TMT) and the European Extremely Large Telescope (E-ELT) which has a 39 m aperture.

1. CHAPTER ONE

"If the Theory of making Telescopes could at length be fully brought into Practice, yet there would be certain Bounds beyond which Telescopes could not perform. For the Air through which we look upon the Stars, is in perpetual Tremor;"
- Sir Issac Newton

1.1. Introduction to Adaptive Optics

1.1.1. The Atmospheric Limit

The atmosphere that lies between us and the cosmos allows spectacular glimpses of the universe. Rays travel to us from vast distances, bringing us information about the universe; they travel unchanged for up to billions of light years until they come into contact with our atmosphere, then in the final milliseconds they are changed. The atmosphere is made up of life supporting gasses which are in perpetual motion, the motion and characteristics of these gasses causes the light rays to distort. The atmosphere has three main characteristics that restrict astronomical observations; 1. opacity, due to the absorption of light at certain wavelengths; 2. luminosity, due to scattered light; 3. turbulence, due to solar heating and winds [16]. The atmosphere provides a clear window between 0.3 and $1.0\,\mu$m, covering the ultraviolet (UV), visible, and near-infrared (IR) bands. Between about 1 and $10\,\mu$m, atmospheric transmission varies considerably due to absorption by water (H_2O) and carbon dioxide (CO_2) molecules, but there are good windows at $1.25\,\mu$m (J-band), $1.6\,\mu$m (H-band), $2.2\,\mu$m (K-band), and $3.4\,\mu$m (L-band). The atmosphere is opaque to radiation below $0.3\,\mu$m and above $30\,\mu$m but becomes transmissive again at about $1\,$mm (radio) [16]. Most astronomical objects emit a broad spectrum from which a large amount of information can be deduced. Astronomical adaptive optics systems are therefore designed to operate over wide-spectral bands, over which it is essential to compensate the optical path length, independent of wavelength.

Deformable mirrors do this in the most direct way by adjusting the path length mechanically. A given change in optical path length represents a smaller phase error as the wavelength increases. While observations in the visible band at $0.5\,\mu$m are greatly impaired by turbulence, the effects at $10\,\mu$m are negligible for all except the very largest apertures. Wavefront distortion is more easily compensated at near-IR wavelengths than in the visible, which is the main reason that astronomical adaptive optics has been most successful at wavelengths between 1 and $3.4\,\mu$m [16].

Out of all of the atmosphere's characteristics, turbulence is the one that most significantly distorts the light rays reaching us. Turbulence caused by solar heating sets up convection currents that transport various masses of air pockets at different velocities. The resulting heat plumes extend up to about $3\,$km. Above this altitude, turbulence occurs in layers associated with wind shear. The highest wind velocities are encountered in the troposphere at altitudes between 10 and $15\,$km. Figure 1.1 shows an image of the Trapezium stars near the center of the Orion Nebula. The image is taken, in the visible band, with the Hubble Space Telescope (HST). The HST is in Earth orbit and is therefore able to record images above the atmosphere, at the resolution defined by physics. This is known as the diffraction limit ($\frac{\lambda}{D}$) and depends on the observing wavelength λ and the size of the telescope aperture D. Images taken with ground based telescopes suffer from atmospheric distortion which limits their resolution to the seeing limit ($\frac{\lambda}{r_0}$) defined by r_0 the coherence length of the atmosphere. Figures 1.2 and 1.3 show the same Trapezium stars imaged with a 14 inch telescope and an $8\,$m telescope. Note that the stars A, B, C, D, E, and F have similar resolution with the $14\,$inch and the $8\,$m telescope implying that when there is atmospheric turbulence the point spread function (PSF) does not depend on the size of the telescope aperture. The diffraction limited PSF and the seeing limited PSF are illustrated in Fig. 1.4. The diffraction limited PSF is formed in the absence of turbulence, when the wavefront travels from the point source, undisturbed, to the telescope aperture. In this case the size of the imaged point source depends on the size of the telescope aperture and is $\frac{f\lambda}{D}$, where f is the focal length of the imaging lens, λ is the observation wavelength, and D is the aperture diameter. The lower diagram in Fig. 1.4 shows how the size of a point source imaged through turbulence depends on the atmospheric seeing limit. In this case the

size of the telescope aperture is irrelevant provided that D is larger than r_0

Figure 1.1: Trapezium stars observed in visible with 2.4 m HST in earth orbit.
[1]

Figure 1.2: Trapezium stars observed in visible with 14 inch located in Muscat, Oman.
[2]

Figure 1.3: Trapezium stars observed in near infrared with 8 m ESO VLT in Paranal, Chile.
[3]

1.1.2. Parameters that Characterize Atmospheric Turbulence

In this section I explore the parameters, which characterize atmospheric turbulence[4] and reduce, in certain cases, the performance of large (8 to 10 m) telescope to 14 inch telescopes. These parameters are Fried's coherence length, the isoplanatic angle, and the Greenwood frequency. In the simplest terms they represent, respectively, the largest size of an aperture which can form a diffraction limited image through turbulence, the angular extent over which wavefront distortions are correlated, and the rate at which atmospheric turbulence changes.

Fried's Coherence Length : The phase structure function D_ϕ defines a small phase perturbation that occurs between points r and r'. Hufnagel and Stanley [19] showed that for a propagating wave D_ϕ is proportional to the $5/3$ power of spatial separation and is given by [19] :

$$D_\phi(r) = \Big\langle (\phi(r') - \phi(r'-r))^2 \Big\rangle = 2.91 \Big(\frac{2\pi}{\lambda}\Big)^2 \int C_n^2(h) \Big(1 - \frac{h}{z_g}\Big)\, dh\, r^{5/3} \tag{1.1}$$

[1] NASA; K.L. Luhman (Harvard-Smithsonian Center for Astrophysics, Cambridge, Mass.); and G. Schneider, E. Young, G. Rieke, A. Cotera, H. Chen, M. Rieke, R. Thompson (Steward Observatory, University of Arizona, Tucson, Ariz.)

[2] Samir Kharusi, www.samirkharusi.net/trapezium.html

[3] ESO/M.McCaughrean et al. (AIP)

[4] prescribed by Kolmogorov statistics.

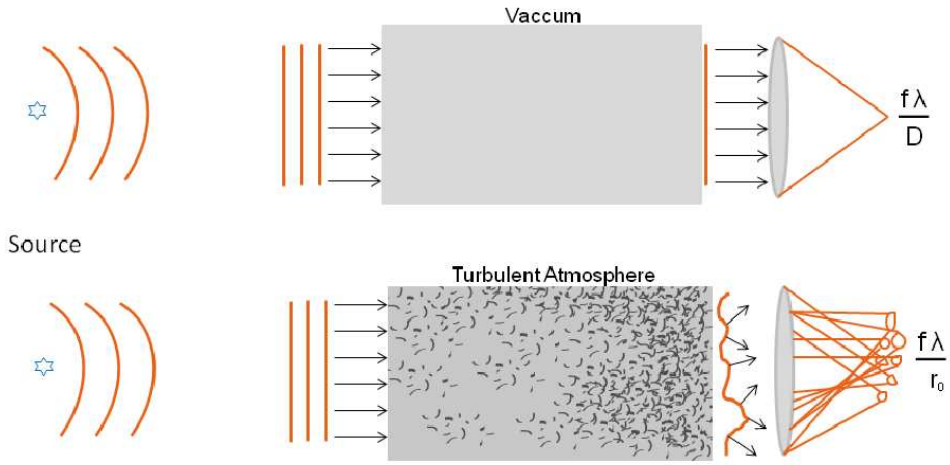

Figure 1.4: The figure illustrates how a star image is blurred by atmospheric turbulence. In the presence of turbulence the resolution depends on the atmospheric coherence length r_0 and not on the size of the telescope aperture D. Turbulence converts the diffraction limited ($\frac{\lambda}{D}$) point spread function (PSF) into a seeing limited ($\frac{\lambda}{r_0}$) PSF. The focal length of the imaging lens is f, multiplying it by the PSF gives the size of the imaged spot.

where λ is the propagation wavelength, h is the height of the turbulent layer, $C_n^2(h)$ is the refraction structure function, z_g is the distance to the source, and the integration is over the optical path from the source to the observation point. For plane waves the term $\frac{h}{z_g}$ disappears. For astronomical observations, the near-field approximation can be used, so that the coherence function at the ground is [16]

$$B_0(r) = \exp\Big[-\frac{1}{2} D_\phi(r) \Big] \tag{1.2}$$

Fried built upon this theory and developed a convenient relationship between the phase structure function and the optical transfer function (OTF). The OTF for the whole imaging system is a combination of the atmospheric transfer function $B(f)$ and the telescope transfer function $T(f)$. Fried [7] introduced the telescope resolving power which is defined as the integral of the OTF. For a telescope looking through turbulence the resolving power $\mathscr{R}$ is [16]:

$$\mathscr{R} = \int B(f)\ T(f)\ df \tag{1.3}$$

For a small aperture telescope the effects of turbulence are negligible and the resolving power will depend on the the telescope transfer function. For a large aperture telescope the resolving power depends only on the turbulence [16]:

$$\mathscr{R} = \int B(f)\ df \tag{1.4}$$

Fried also defined the parameter r_0, which is the diameter of a diffraction-limited telescope which would have the same resolving power as the atmospheric transfer function; that is r_0 is the diameter of a perfect telescope where that transfer function is equal to the resolving power [16]

$$\int T(f)\ df = \int B(f)\ df \tag{1.5}$$

This leads to the relation [16]:

$$\mathscr{R} = \int B(f)\ df = \frac{\pi}{4}\left(\frac{r_0}{\lambda}\right)^2 \tag{1.6}$$

The atmospheric transfer function may be written as [16]

$$B(f) = B_0(\lambda\ f) = \exp(-K\ f^{5/3}) \tag{1.7}$$

where K is a constant that describes the seeing conditions [16]

$$K = 3.44\left(\frac{r_0}{\lambda}\right)^{-5/3} \tag{1.8}$$

Substituting K in to Eq. 1.7 gives

$$B(f) = \exp\left[-3.44\left(\frac{\lambda\ f}{r_0}\right)^{5/3}\right] \tag{1.9}$$

By equating Eq. 1.2 and Eq. 1.9 and substituting D_ϕ the definition of r_0 in terms of the integrated turbulence is obtained [16]:

$$r_0 \cong \left[\frac{0.06\ \lambda^2}{\int C_n^2(h)\ dh}\right]^{3/5} \tag{1.10}$$

The phase structure function can now be expressed in terms of r_0 [16] [39]:

$$D_\phi(r_0) = 6.88\left(\frac{r}{r_0}\right)^{5/3} \tag{1.11}$$

Fried's coherence length r_0 is a convenient measure of atmospheric turbulence as it represents the integrated effect of the refractive index fluctuations for the entire atmosphere. Small values of r_0 correspond to strong turbulence and poor seeing, while large values correspond to weak turbulence and good seeing. The numerical value of r_0 ranges between 10 and 30 cm, in the visible band, for vertical propagation at a good seeing sight.

Anisoplanatism : The wavefront measured with a point reference source (a natural guide star) is strictly valid for an object in the same direction as the reference. Consider a single layer of turbulence at some distance h from the entrance pupil of the telescope. If the observation object is at zenith and the reference source is at some angle α then the wavefront error between the object and the reference varies as a function of the angle α. If the coherence length of turbulence is r_0, then angle over which the wavefront disturbance is well correlated must be a function of r_0/h. The isoplanatic angle θ_0 is defined as the angle at which the mean-square wavefront error, averaged over a large aperture, is $1\,\text{rad}^2$. The isoplanatic angle is extremely small, typically about $2\,$arc seconds at visible wavelengths, increasing to about $10\,$arc seconds at IR [16]. Fried defines the isoplanatic angle θ_0 in terms of the refraction structure function integrated along the optical propagation path:

$$\theta_0 = \left[2.91 \left(\frac{2\pi}{\lambda}\right)^2 \int C_n^2(h)\, h^{5/3}\, dh\right]^{-3/5} \tag{1.12}$$

then the isoplanatic error for an angle θ may be expressed as [16]:

$$< \sigma_\theta^2 >= \left(\frac{\theta}{\theta_0}\right)^{5/3} \tag{1.13}$$

Temporal Variations : Up until now we have focused on wavefront distortions caused by spatial variations, now we will discuss wavefront distortion caused by the temporal changes in the atmosphere. To first order temporal variations can be modeled as "frozen" spatial variations which are moved across the telescope aperture at velocity v. The movement across the aperture can be caused by wind or a slewing telescope. Greenwood found the residual wavefront error in terms of the ratio of the effective bandwidth of the turbulence to that of the correction servo [10].

$$\sigma^2 = \left(\frac{f_G}{f_s}\right)^{5/3} \tag{1.14}$$

here f_s is the servo bandwidth. In order to optimize wavefront correction the error σ^2 should be no more than $1\,\text{rad}^2$. The parameter f_G is a characteristic frequency of the atmospheric turbulence, known as the Greenwood frequency, and is given by:

$$f_G = \left[0.102 \left(\frac{2\pi}{\lambda}\right)^2 \int_0^\infty C_n^2(h)\, v^{5/3}(h)\, dh \right]^{3/5} \tag{1.15}$$

The value of f_G is determined from the turbulence and wind profiles and Eq. 1.14 can be used to calculate the error induced by any servo bandwidth. In the special case of a single turbulent layer with wind velocity v, the Greenwood frequency becomes [16]:

$$f_G = 0.427 \frac{v}{r_0} \tag{1.16}$$

1.1.3. Adaptive Optics - An enabling technology

In section 1.1.1 we saw how poor atmospheric seeing reduces the angular resolution of a telescope from λ/D to λ/r_0. In these circumstances building telescopes that have a diameter larger than r_0, which is generally between 0.1 and $1\,$m depending on wavelength and site, does not improve the image resolution. Putting telescopes on mountain tops offers some reprieve but is only a partial solution. Atmospheric seeing at the best sites is $0.5\,$arc-seconds at $0.5\,\mu$m which is equivalent to the diffraction limited resolution of a $20\,$cm telescope. Telescopes much larger than $20\,$cm are desired in order to collect more light and to, ideally, increase the angular resolution which allows us to detect and image, dim, closely spaced objects such as exoplanets orbiting around a host star. Putting telescopes in space, will eliminate turbulence, but is expensive (the HST cost $\$2.2\,$billion) and increases design complexity. Also current launch technology limits the size of telescopes that can be put in space which in turn limits the light collecting area and the angular resolution of the telescope. Adaptive optics (AO) allows us to use telescopes with apertures larger than r_0, to take advantage of the resolution offered by the telescope, even when we are looking at celestial objects through the atmosphere. The purpose of AO is to correct atmospheric aberrations so that objects can be imaged at the diffraction limit, even when viewed through turbulence. In IR ground-based telescopes equipped with adaptive optics can achieve higher resolution, and collect more light compared to space-based telescopes. At shorter wavelengths adaptive optics offers comparable

performance at a much reduced cost. In ground-based telescopes the AO and imaging instruments can be realigned and reconfigured easily to support different observational runs; such changes are much more difficult to make on a space-based telescope. Atmospheric turbulence is the most serious problem faced by ground-based telescopes and the primary reason for using adaptive optics, however it can also be used to correct figure errors in the primary mirror, as well as optical errors resulting from things such as temperature fluctuations and the gravity vector.

AO systems consist of three main components, a wavefront corrector, a wavefront sensor, and a control computer, embedded between the primary mirror and the science camera. The main components of an AO system are shown in Fig. 1.5. Light from a reference source such as a natural guide star (NGS) or a laser guide star (LGS) passes through the turbulent atmosphere and is collected by the primary mirror. The light from the primary mirror is reflected to a secondary mirror, before it comes to a focus. The distorted beam reflected by the secondary mirror has a reduced beam size, the beam expanding from the focus of the telescope is collimated by a lens. The corrector elements, the steering mirror (SM) and the deformable mirror (DM) are typically placed in collimated space. In certain speical cases the DM may not be placed in collimated space, as is the case for the adaptive secondary mirror for the $6.5\,\mathrm{m}$ MMT. The SM should be placed in a conjugate pupil plane so that it does not move the image of the pupil on the DM. The SM is usually several centimeters in diameter, and has two degrees of freedom. The SM is used to remove image motion. The DM is typically placed at a conjugate pupil. For the $6.5\,\mathrm{m}$ MMT the secondary mirror serves as the DM and is the system stop. The DM must be as large as the optical beam and for large telescopes can be as large as $40\,\mathrm{cm}$ in diameter consisting of 2000 actuators. The DM corrects higher order aberrations. A beam splitter placed down stream from the DM splits the light between the wavefront sensor and the science camera. The wavefront sensor senses and then reconstructs the wavefront, the information is converted to electrical signal and sent to the wavefront correctors via the control loop. The wavefront correctors apply the opposite signal to the incoming wavefront in order to correct the distorted wavefront. The speed at which the control loop needs to operate in order to correct the wavefront depends on the Greenwood frequency. Typically for astronomical

AO to correct wavefront distortion resulting from turbulence, the control loop needs to operate at several hundred Hertz to a few Kilo-Hertz in order to keep up with the changing atmosphere. The science camera records the compensated image.

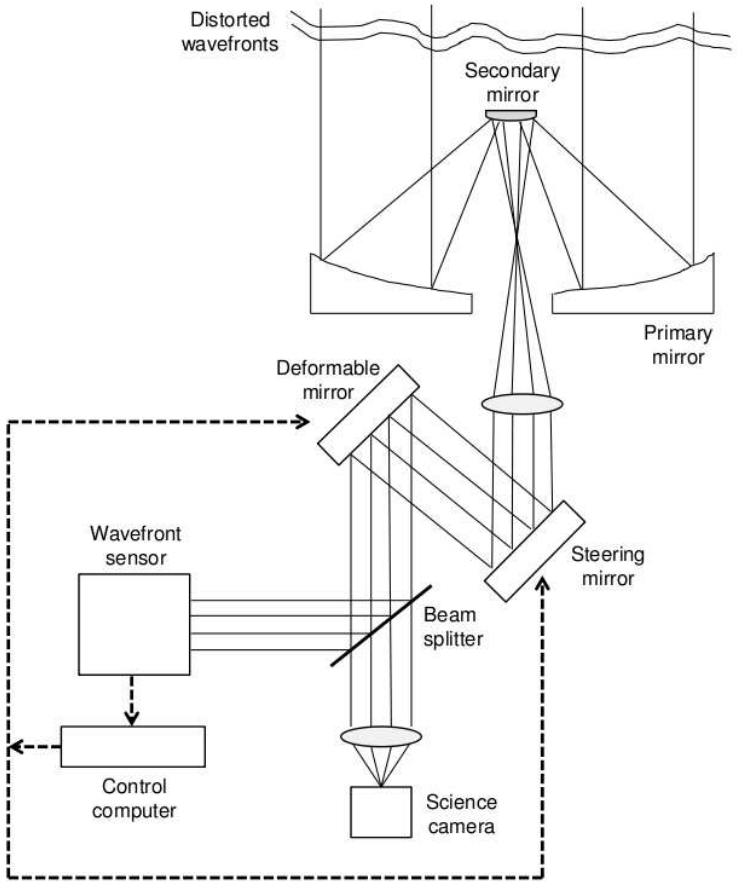

Figure 1.5: Schematic of a Cassegrain telescope with an adaptive optics (AO) system. Light from the focus of the telescope diverges to fill a lens which collimates the light. The collimated light is sent to the steering mirror (SM) which corrects wavefront tip and tilt. Light is reflected from the SM to the deformable mirror (DM) which corrects high order aberrations. The DM reflects light to a beam splitter which splits the light between the wavefront sensor and the science camera. The wavefront sensor senses and then reconstructs the wavefront which is sent via a control computer to the SM and the DM establishing a closed loop. The DM and the SM apply the opposite of the signal sent by the wavefront sensor in order to correct the wavefront.

1.2. What is a Wavefront Sensor

A wavefront sensor is needed to convert phase aberrations into intensity which can then be recorded by a detector. Phase aberrations caused by, atmospheric turbulence, deformations in the optical surface, and or local temperature fluctuations, distort the incident wavefront. Just as a Young's double slit interferometer splits an incoming wave into two different waves that emerge from the two slits with a phase-shift, turbulence splits the incident wave into several different waves that traverse different path lengths and have phase-shifts with respect to one another. The intensity or the interference pattern of these waves encodes the phase-shift which is used to reconstruct the wavefront. When the interferring waves originate from the same point in space and time they are considered to be respectively, spatially and temporally coherent. Spatial coherence is lost when the signal is produced by interferring points on an extended source of angular extent $\theta > \theta_0$, where θ_0 is isoplantic angle. For this reason high performance wavefront sensors lose sensitivity when a LGS, which is typically about $1''$, is used as the reference source. Pupil plane spatial coherence can also be lost if the wavefront sensor exposure time is long enough for the phase to change by more than 1 radian. Temporal coherence can be lost if light originating from different parts of an extended source reaches the pupil with a time delay $\tau = t_1 - t_2$, such that the optical path difference OPD $= v\tau/\lambda \geq 1$ radian. When the interfering electromagnetic waves have the same wavelength they are considered to be spectrally coherent. Coherent interference results in optimal intensity signal whereas incoherent interference results in an attenuated intensity signal.

Ideally a wavefront sensor should posses the following three characteristics; sensitivity to a wide range of spatial frequencies, large dynamic range, and linearity. Sensitivity is the wavefront sensors ability to use the available photons in the most efficient manner. Guyon [11] has formulated that ideally the radian root-mean-square (RMS) error Σ in measuring a single mode should be $\Sigma = 1/\sqrt{N_{ph}}$, if the wavefront sensor is able to measure phase and not amplitude in the pupil. Here N_{ph} is the number of available photons. Dynamic range refers to the wavefront sensors ability to correct wavefront aberrations. Large dynamic range wavefront sensors are those that can measure phase errors larger than 1 radian. Lastly there should be a linear relationship between the wavefront

sensor output signal (intensity) and the input wavefront aberrations. Guyon [11] [13] shows that it is not possible to have a wavefront sensor with all three characteristics. The Shack-Hartmann (SH), Curvature, and the Modulated Pyramid (MPy) wavefront sensors are linear, have a large dynamic range but have poor sensitivity. The Fixed Pyramid (FPy) wavefront sensor, Zernike phase contrast mask (ZPM), and the pupil plane Mach-Zehnder interferometer (PPMZ) are linear, have high sensitivity but low dynamic range. The non-linear Curvature (nlC) and non-linear Pyramid (nlPy) wavefront sensors are sensitve, have a high dynamic range, but are non-linear. Since all three characteristics cannot be embodied in a single wavefront sensor it is important to define the observational goal and identify a suitable wavefront sensor, including considerations such as budget, design complexity, operational challenges, available talent, and time constraint.

1.3. Wavefront Sensing Performance Gap: A comparison between the nlCWFS and the SHWFS

The objective of this dissertation is to build a highly sensitive wavefront sensor for astronomical AO with a NGS. The proposed wavefront sensor will enable diffraction-limited AO imaging of dim exoplanets in the visible. AO systems routinely deliver diffraction-limited images at near-IR and mid-IR wavelengths on 8 to 10 m telescopes, however the reconstructed wavefront quality is poorer than required. For example obtaining high quality diffraction-limited images at visible wavelengths requires residual wavefront errors to be below 100 nm RMS [13]. Commonly used wavefront sensors such as the SHWFS are unable to deliver such low wavefront errors because they are unable to use the spatial coherence of the full aperture. In order to deliver high wavefront errors the nlCWFS uses only NGSs as a reference. Using extended LGSs as the reference source causes cone-anisoplanatism leading to attenuation of the interference signal, as discussed in section 1.2. For this reason high accuracy wavefront sensing is fundamentally challenging with LGSs. The goal of this dissertation is therefore to develop a NGS wavefront sensor.

The detection of an Earth-like planet orbiting a nearby star requires obtaining an extraordinarily high contrast at small angular separations. There is a significant performance gap between laboratory obtained contrasts and on-sky performance. The High Contrast Imaging Testbed (HCIT)

at NASA JPL has achieved better than 10^{-9} raw contrast at $4\ \lambda/D$ in the visible [38]. Comparatively the Extreme-AO systems currently being built, such as SPHERE (ESO-VLT) and GPI (Gemini) expect to deliver a 10^{-4} contrast at $5\ \lambda/D$ in near-IR [13]. The current performance gap can largely be attributed to inefficient wavefront sensing. In order to improve wavefront sensing we have to move away from ineffecient high-order systems which are mostly designed around the SHWFS.

The SHWFS is quite robust and can measure large wavefront errors however it does not efficiently use the available photons. In a SHWFS the pupil plane is split into several subapertures and a wavefront slope is measured per subaperture as the off-axis deviation of the focal plane spot. Splitting the pupil into subapertures causes the SHWFS to lose spatial coherence leading to poor sensitivity to low order modes that require interference distances to be larger than the subaperture size. The angular size of the focal plane spot imaged onto each subaperture is λ/d whereas at the diffraction limit it would be λ/D. Here d is the size of the SH subaperture. It is important to be able to sense and correct low order modes as they dominate atmospheric turbulence and scatter light at small angular separations where an exoplanet could be found. Typically the subaperture size is on the order of r_0, making it larger can potentially improve the SH's spatial coherence. However this will lead to aberrated PSFs since the angular resolution will be governed by the atmospheric seeing limit. Therefore sensitivity to low order modes cannot be gained by reducing the number of subaperutres. In addition having a small number of subapertures limits the number of modes that can be corrected. A large number of actuators and correspondingly large number of subapertures are required to correct a large number of modes. However increasing the number of subapertures lowers the SNR within a subaperture, since the total number of available photons is constant, leading to further degradation in sensitivity. This means that a compromise has to be made between being able to correct a large number of modes and maintaining sensitivity to low order modes.

The non-linear curvature wavefront sensor (nlCWFS) is based on the conventional curvature wavefront sensor but uses a non-linear reconstruction algorithm. The nlCWFS uses Fresnel propagation to convert phase aberrations into intensity and is not constrained by the conventional

curvature wavefront sensor's (cCWFS) requirement where the wavefront signal needs to be a linear function of the wavefront aberration. With the nlCWFS wavefronts can be propagated, short distances to convert high spatial frequencies in to intensity, and long distances to convert low spatial frequencies in to intensity. In essence, because the nlCWFS does not split the pupil, it maintains its full spatial coherence; allowing interference between points with small separations (high spatial frequencies) as well as between points with large separations (low spatial frequencies). In order to sense a low order mode like tip-tilt points from opposite ends of the aperture should be interfered, which the nlCWFS allows. The nlCWFS can measure tip-tilt with a λ/D resolution whereas the SHWFS measures tip-tilt with a λ/r_0 resolution. Therefore when sensing tip-tilt the gain in sensitivity for the nlCWFS over the SHWFS is D/r_0. This is equivalent to the nlCWFS being able to sense the wavefront with the same accuracy as a SHWFS, but with $(D/r_0)^2$ fewer photons. The gain in sensitivity when sensing other spatial frequencies follows with D being replaced by the integration spacing appropriate for that particular spatial frequency.

I conclude that the nlCWFS as opposed to the SHWFS is able to work at the sensitivity limit set by physics. The nlCWFS is ideal for high contrast imaging as well as imaging bright targets with short exposure times. It is sensitive to both low and high spatial frequencies. Since the nlCWFS extracts phase information from speckles, which are λ/D in size, it is able to sense at the diffraction limit as opposed to the SHWFS which senses at the seeing limit. When background limited the nlCWFS has a net gain of D^4, because it benefits from D^2 gain due to the diffraction limit and a D^2 gain due to the telescopes collecting power whereas convenetional wavefront sensor only have a D^2 gain due to the telescopes collecting power. This difference become significant for extremely large telescopes.

2. CHAPTER TWO

"Everything should be made as simple as possible, but not simpler. "

- Albert Einstein

2.1. The non-linear Curvature Wavefront Sensor

2.1.1. Development

The non-linear Curvature Wavefront Sensor (nlCWFS) is derived from the Curvature Wavefront Sensor (CWFS) proposed by François Roddier in 1988 [32] to measure the curvature of the wavefront instead of its slope. The principle of this sensor is presented in Figure 2.1. A telescope of focal length f images the source in its focal plane, labeled as the nominal focus. A local wavefront curvature that produces an excess of illumination in a plane before the focus will produce a lack of illumination in a plane after the focus. The CWFS consists of two detectors placed in the out of focus planes referred to as Fresnel planes. One detector records the irradiance distribution in the plane of excess illumination and the second records the irradiance distribution in the plane where there is a lack of illumination.

The two Fresnel planes can also be placed on either side of the pupil plane: both representations are equivalent as a defocused focal plane image is also a defocused pupil plane image. Hence the light intensity is measured in planes optically conjugated on either sides of the pupil [33]. A vibrating membrane (VM), which acts as a variable length element in the focal plane is used to alternate between the Fresnel planes. The distance z from the pupil plane to the Fresnel plane, conjugated to the detector array is given by [14]:

$$z = -\frac{f_1^2}{f_m} \tag{2.1}$$

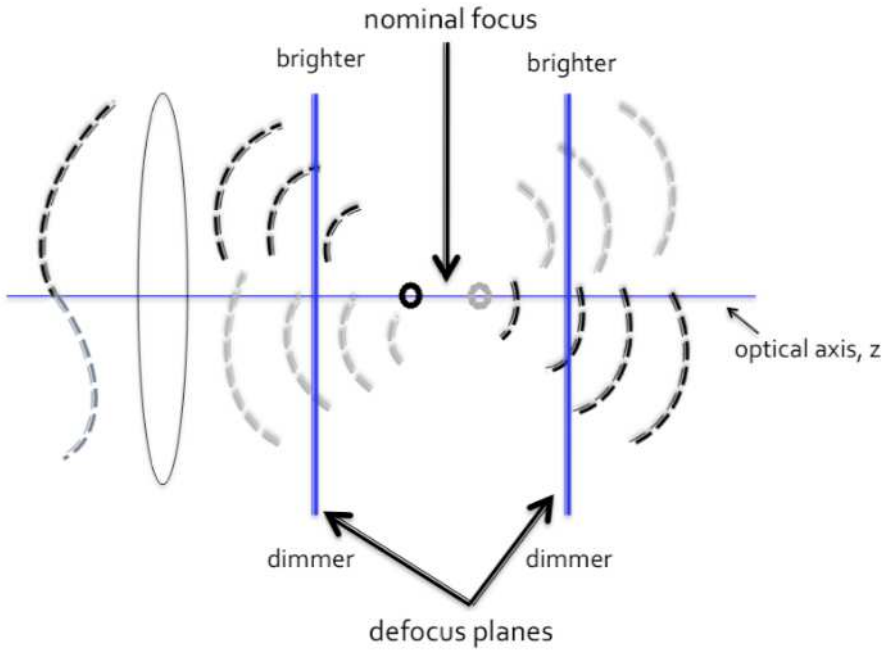

Figure 2.1: Principle of curvature wavefront sensing proposed by Roddier [32]. As the wavefront passes through nominal focus its curvature reverses sign. A detector placed on either side of the focus can record the intensity of the wavefront in the two planes.

where f_1 is the focal length of the beam delivered to the VM and f_m is the VM's focal length. CWFSs rely on Fresnel propagation over the distance z to transform phase aberrations into intensity fluctuations. Consider a complex amplitude $W(\mathbf{v}, z)$, where $\mathbf{v}$ is the 2D coordinate on a plane perpendicular to the optical axis and z is the coordinate along the optical axis. A pupil plane optical path difference (OPD) aberration of spatial frequency $\mathbf{f}$, spatial phase θ, and amplitude h corresponding to the complex amplitude [11, 14]:

$$W(\mathbf{v}, 0) = \exp\left[j\frac{2\pi h}{\lambda}\,\sin(2\pi\mathbf{v}\cdot\mathbf{f} + \theta)\right] \tag{2.2}$$

is transformed, after propagation over a distance z, in to

$$W(\mathbf{v}, z) = \exp\left[e^{jd\phi} \times j\frac{2\pi h}{\lambda}\,\sin(2\pi\mathbf{v}\cdot\mathbf{f} + \theta)\right]. \tag{2.3}$$

here $e^{jd\phi}$ is called the transfer function, z is embedded in $d\phi$ and the relationship is developed below. I now explore what the transfer function means and the information it contains. According to the

Huygens-Fresnel principle we can compute the scalar fields in a plane (x_2, y_2) at $z = z_2$ in terms of the fields in the plane (x_1, y_1) at $z = z_1$. Consider a point on the plane (x_1, y_1) as a point source with amplitude and phase given by the weight u(x_1, y_1). Each of these sources radiates a spherical wave, and the fields at observation point (x_2, y_2) can be computed by adding up all of the individual contributions. Mathematically we can write:

$$u_2(x_2, y_2) = \int\int_{-\infty}^{\infty} u_1(x_1, y_1) \frac{z_{12}}{j\lambda r_{12}} \frac{e^{jkr_{12}}}{r_{12}} dx_1 dy_1. \tag{2.4}$$

Equation 2.4 is the Kirchhoff approximation to the Rayleigh-Sommerfeld diffraction integral. The kernel $e^{jkr_{12}/r_{12}}$ gives spherical waves. The Fresnel approximation takes the spherical wave and approximates it with quadratic phase curvature [2]:

$$u_2(x_2, y_2) = \frac{e^{jkz_{12}}}{j\lambda z_{12}} \int\int_{-\infty}^{\infty} u_1(x_1, y_1) \exp\left[j\frac{\pi}{\lambda z_{12}}[(x_2 - x_1)^2 + (y_2 - y_1)^2]\right] dx_1 dy_1. \tag{2.5}$$

we recognize this to be the Fresnel transform of the field in the aperture given by $u_1(x_1, y_1)$. Using properties of the convolution integral we can write the above expression as a convolution [2]:

$$u_2(x, y) = u_1(x, y) \otimes h_{12}(x, y). \tag{2.6}$$

where we define the impulse as:

$$h_{12}(x, y) = \frac{e^{jkz_{12}}}{j\lambda z_{12}} \exp\left[jk\frac{\pi}{\lambda z_{12}}(x^2 + y^2)\right]. \tag{2.7}$$

The Fresnel kernel is $\epsilon = \frac{x_2}{\lambda z_{12}}$ and $\eta = \frac{y_2}{\lambda z_{12}}$ which is the 2D spatial frequency of the wave. We relate the phase term in Eq. 2.7 to the phase $d\phi$ in Eq. 2.3. This gives $d\phi = \pi|f|^2 z\lambda$, where f is the 2D spatial frequency given by the Fresnel kernel. Solving for z when $d\phi$ is $\pi/2$ gives:

$$z = \frac{1}{2|f|^2\lambda}. \tag{2.8}$$

Here z is the Fresnel propagation distance. If the propagation distance z is such that $d\phi = \pi/2$,

$W(\mathbf{u}, z)$ is real: Fresnel propagation has transformed the phase aberration in to a pure intensity aberration. If $d\phi$ is a multiple of 2π, the propagated complex amplitude wave is a copy of the original wave and is purely phase. This effect that replicates spatial frequencies at periodic intervals is known as the Talbot Effect and the distance z at which the magnitude of the amplitude repeats is known as the Talbot distance [36]. For high order aberrations (high spatial frequency) the conversion of phase into intensity occurs at smaller Fresnel distances than for low order aberrations (low spatial frequency). Here and through out this work the Fresnel distance refers to the propagation distance between the pupil plane and the Fresnel plane.

In a conventional CWFS the contrast obtained between defocused image planes can be related to the geometrical shape of the wavefront. The distance z at which conjugate planes are chosen selects the spatial frequencies the wavefront sensor will be sensitive to. The contrast between the defocused images $W_+ = |W(\mathbf{v}, z_+)|^2$ and $W_- = |W(\mathbf{v}, z_-)|^2$ is

$$C = \frac{W_+ - W_-}{W_+ + W_-} = \tanh\,[2\sin(d\phi)\frac{2\pi h}{\lambda}\sin(2\pi\mathbf{vf} + \theta)]. \tag{2.9}$$

For low spatial frequencies, $d\phi$ reaches $\pi/2$ at large z, but for high spatial frequencies $d\phi$ reaches $\pi/2$ at small z much closer to the pupil plane. For spatial frequencies which can be corrected by the AO system, If the phase error is less than 1 radian implying that $d\phi < 1$ and $4\pi h\,\sin(d\phi)/\lambda \ll 1$, then Eq. 2.9 can be approximated to:

$$C \approx 4\pi^2 f^2\; z\; h\; \sin(2\pi\mathbf{vf} + \theta) \tag{2.10}$$

This is an important result which states, that in the regime where this approximation is valid, the contrast obtained between defocused image planes, is equal to the Laplacian of the wavefront. In this regime the wavefront sensor is linearly related to the wavefront error. The linear relationship between contrast and the geometrical shape of the wavefront leads conventional CWFSs to operate in the linear regime. AO systems prefer to operate in the linear regime as it is easier to implement a linear control algorithm than a non-linear one, for closed loop operation. Equations 2.9 and 2.10

show that with larger z the conversion from phase to intensity is more efficient, z acts as an optical gain in the CWFS and therefore should be chosen large. There are however limits to how much z can be increased. If the constraint $d\phi \ll \pi$ is not satisfied then the WFS signal is no longer linear and Eq. 2.10 is no longer valid. Conventional curvature wavefront sensing relies on linearity of the WFS measurement for which the contrast C measured should be proportional to the second derivation of the wavefront. If $d\phi > \pi$, sin($d\phi$) and $d\phi$ can have opposite signs, in which case the CWFS will produce a signal with a sign opposite to the actual wavefront. Eq. 2.10 would then lead to runway amplification at high spatial frequencies [14]. This constrains $d\phi$ to be less than π at high spatial frequencies. For $d\phi < \pi$ and with the Fresnel kernel substitution for spatial frequency ($f = \frac{x}{\lambda z}$) where z defines the optical axis and x is the one dimensional aperture,

$$z = \frac{2D^2}{N^2\lambda} \quad (for\ d\phi = \frac{\pi}{2}). \tag{2.11}$$

Here z is the propagation distance that I mention at the beginning of the section. D is the pupil diameter, N is the linear number of wavefront sensor elements across the pupil, and λ is the wavelength of observation. In Eq. 2.8 the expression for z is given for $d\phi = \frac{\pi}{2}$ and for a specific spatial frequency f. In order to increase the optical gain of the system z has to be increased but how much z can be increased is limited by linearity constraints ($d\phi < \pi$). Optical gain is important because it allows us to detect dim objects under good seeing conditions. It also makes it possible to score on bright targets in poor seeing when the AO control loop has to operate at kilohertz speeds in order to correct the fast changing atmosphere. In such seeing conditions having a high optical gain allows for wavefront sensing and correction even with short (fractions of a second) integration time on a target. Optical gain is the key to observe in such photon starved situations. For a sensor to be sensitive to high spatial frequencies it requires a high number of elements; however a qualitative model exploring the range of z distances shows that as the number of elements increases, the Fresnel distance shrinks in order to maintain Nyquist sampling for the highest spatial frequency measured, and sensing of low-order aberrations becomes increasingly inefficient as $d\phi$ is much smaller than $\pi/2$ and phase has not yet fully turned into amplitude. Therefore, the ability

of a CWFS to efficiently sense low-order aberrations decreases as the element density increases. A compromise needs to be made between two opposing requirements. A high number of elements is necessary to achieve high Strehl ratios on bright guide stars, and a low number of elements is needed to maintain sensitivity for faint guide stars. This means that the CWFS can either be tuned for high-order aberrations and bright targets (small Fresnel distance) or low-order aberrations and faint targets (large Fresnel distance) but can not efficiently measure both. This limitation is referred to as the noise-propagation effect [11]. Even if a CWFS is tuned to sense low order aberrations the selection of the Fresnel plane distance is limited by the linearity constraints discussed above. The range of z is limited to $d\phi$ being much less than $\pi/2$.

2.1.2. non-linear Curvature Wavefront Sensor Concept

The non-linear Curvature Wavefront Sensor (nlCWFS) developed in this dissertation moves away from relating the curvature of the wavefront to the contrast measured by the detector. The nlCWFS is therefore not constrained by the linearity regime in which it is mathematically permissible to relate the Laplacian of the wavefront to the recorded contrast. The nlCWFS extracts information from speckles that develop as phase is propagated from the pupil plane. Figure 2.2 shows the propagation of a complex field away from the pupil plane along direction z. The pupil diameter is $1.5\,\mathrm{m}$ and the field wavelength is $790\,\mathrm{nm}$. The column of images on the right side show intensity measurements made in different Fresnel planes. The Fresnel planes close to the pupil show tight speckles which encode high spatial frequencies and convert phase into intensity at relatively small propagation distances. Fresnel planes further away from the pupil show diffused speckles which encode low spatial frequencies, that are converted into signal at relatively larger propagation distances. In Fig. 2.2 at $z \approx 22\,\mathrm{km}$ we can see that the light rays begin to cross over one another. In this domain the points in the image plane can no longer be traced back to points in the pupil plane. This is the beginning of the non-linear regime where the shape of the wavefront is no longer linearly related to the contrast obtained in conjugate planes on either side of the pupil.

The nlCWFS is able to sense low and high spatial frequencies simultaneously by recording

the pupil plane wavefront in different Fresnel planes and uses a Gerchberg-Saxton reconstruction algorithm to recover the wavefront in the pupil plane. The Fresnel planes can be selected as far as the lowest spatial frequency, and as close as the highest spatial frequency present in the wavefront. Any number of Fresnel planes can be selected, however we limit them to four to make the reconstructor feasible for a real time adaptive optics system. Four Fresnel planes, that represent the range of spatial frequencies present in the pupil plane wavefront, are selected. The four Fresnel planes can be positioned at any desired distance with respect to the pupil and need not be conjugated on either side of the pupil plane.

The non-linearity of the proposed wavefront sensor imposes a significant penalty on the speed of the the AO control loop. Boot-strapping off of a traditional, linear CWFS could potentially expedite wavefront correction as the initial compensation is done linearly. The linear algorithm would correct all phase aberrations in the ≈ 1 radian domain before passing on the less aberrated wavefront to the time consuming, non-linear algorithm used by the nlCWFS. The non linear Gerchberg-Saxton reconstruction process is described in section 2.2.1. In order to boot-strap off of a traditional, linear CWFS conjugate pairs of Fresnel planes need to be selected on either side of the pupil plane. In later simulations and optical designs discussed in chapters 3 and 5 the selection of conjugate pairs is abandoned due to limited optical-bench space or wavelength selection constraints for chromatic compensation.

2.2. Converting Wavefront Sensor Signal to Wavefront Estimate

2.2.1. non-linear Curvature Wavefront Sensor

I have chosen to implement a Gerchberg-Saxton [8] non-linear reconstruction algorithm, however other reconstruction algorithms may exist. A Gerchberg-Saxton iterative loop is used to reconstruct the phase sensed with the nlCWFS. The Gerchberg-Saxton reconstruction algorithm, illustrated in Figure 2.3 works by propagating complex fields between planes to recover the phase information in the pupil plane. The propagation is carried out by computing the Fresnel diffraction integral given

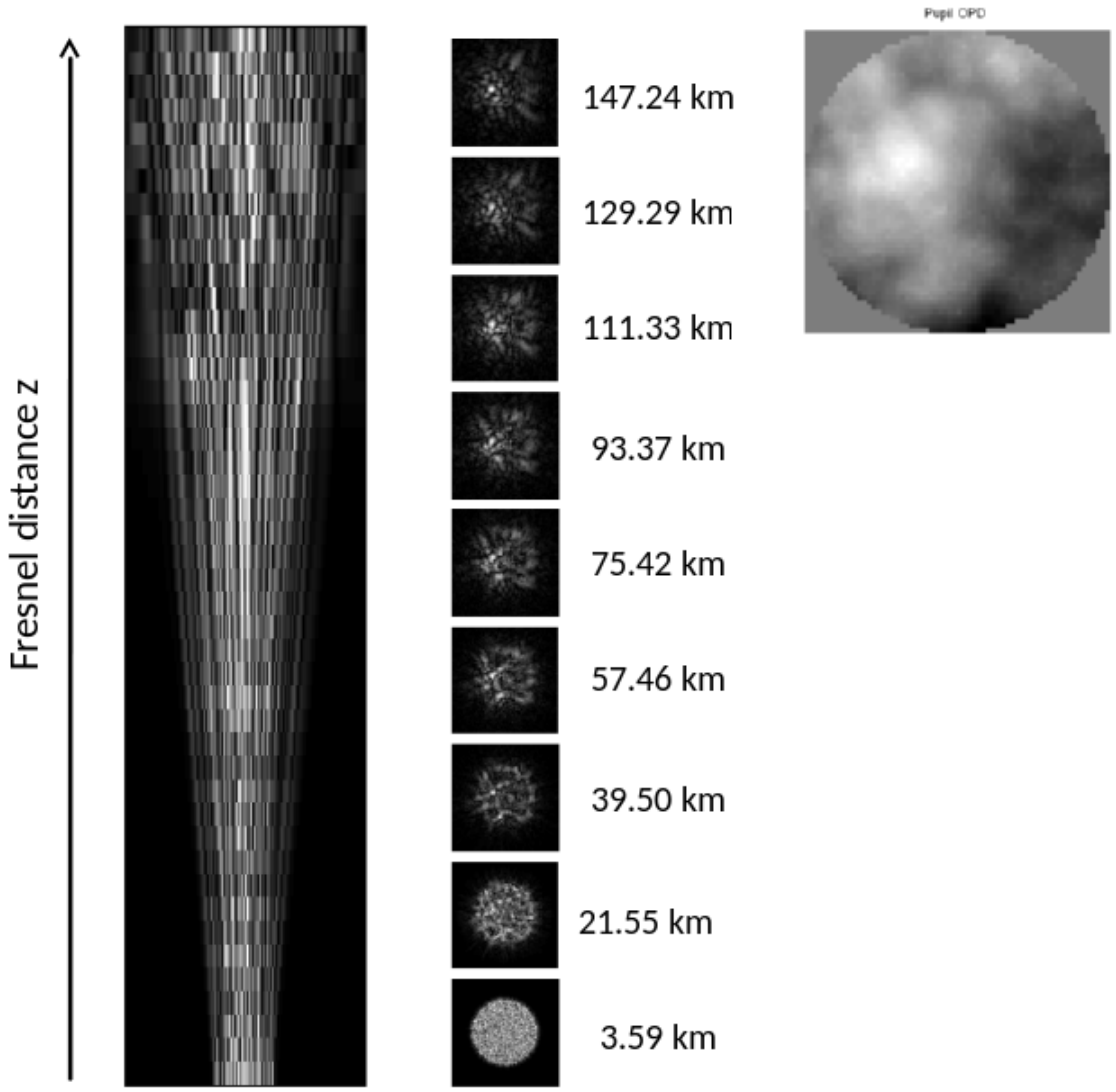

Figure 2.2: The diverging light rays show how the rays become non-linear at large Fresnel distances. The arrow points away from the pupil plane and represents Fresnel distance. The column of images on the right show the speckles recorded at different Fresnel distances. High spatial frequencies encoded in tight speckles are converted to signal at a relatively small propagation distance, where the signal is linear. Low spatial frequencies encoded in diffused speckles are converted to signal at relatively larger propagation distances. The signal becomes non-linear at $z \approx 22\,\text{km}$ where the light rays begin to cross over each other. The pupil plane OPD is shown in the top right corner.

in Eq. 2.5 or the equivalent convolution integral given in Eq. 2.6. As mentioned in section 2.1 in making the Fresnel approximation we approximate a spherical wave as a quadratic phase curvature by eliminating the third term in the binomial expansion of the square root [9]:

$$\sqrt{1+b} = 1 + \frac{1}{2}b - \frac{1}{8}b^2 + ... \tag{2.12}$$

where $b = (\frac{x_2-x_1}{z})^2 + (\frac{y_2-y_1}{z})^2$, x_1 and y_1 refer to points in the source plane, and x_2 and y_2 refer to points in the observation plane. In the Fresnel approximation the maximum phase change induced by dropping the third term, $\frac{b^2}{8}$ in the binomial expansion must be much less than 1 radian. The Fresnel approximation is strictly accurate as long as the propagation distance, the aperture size, and the observing wavelength satisfy the relation[1] [9]:

$$z^3 >> \frac{\pi}{4\lambda}\Big[(x_2-x_1)^2 + (y_2-y_1)^2\Big]^2_{max} \tag{2.13}$$

If the aperture is limited to having a radius L_1 and the observations are restricted to a circle of radius L_2 then we can write,

$$(x_2-x_1)^2 + (y_2-y_1)^2 \leq (L_1+L_2)^2 \tag{2.14}$$

now the validity of the Fresnel region can be expressed as,

$$z^3 >> \frac{\pi(L_1+L_2)^4}{4\lambda} \tag{2.15}$$

The nlCWFS records intensity in four Fresnel planes on either side of the pupil plane. Since we can not measure phase with a sensor the Gerchberg-Saxton loop has no phase information at Fresnel plane (FP) 1, it assumes zero phase. Complex field 1 is constructed using the square root of the recorded intensity in FP 1 and zero phase. Complex field 1 is then propagated to FP 2 and acquires some phase, PH 1 as a result of the propagation. Phase PH 1 is saved. Complex field 1

[1] This is an overly stringent condition, and accuracy can be expected for much shorter distances [9].

also has a new amplitude after the propagation, this amplitude is thrown away. Complex field 2 is constructed by using the square root of the intensity recorded at FP 2 and PH 1. Complex field 2 is propagated to FP 3, again the propagation acquired amplitude is thrown away and the phase PH 3 is stored. Complex field 3 is created from the square root of the intensity recorded in FP 3 and PH 3. The process is repeated at FP 4 and complex field 4 is created which is then propagated back to the pupil plane. At the pupil plane a flat amplitude constraint is applied and a complex field is created from this flat amplitude plus the propagated phase. The loop repeats as the complex field is propagated to FP 1. The loop repeats till the solution converges and we have reconstructed the pupil plane wavefront to with in the photon noise limit. Here I take a slight detour to explain what the photon noise measurement error is by explaining what the photon noise error per mode is and how the error is combined when multiple modes are present. For a single phase aberration mode in the pupil plane the photon noise measurement error for a wavefront sensor operating at the limit set by physics is [11],

$$\Sigma = \sqrt{2/N_{ph}} \tag{2.16}$$

where Σ is the error in reconstructing an individual mode and is measured in radian RMS integrated over the pupil plane. N_{ph} is the total number of photons available for the measurement. To obtain the total error σ resulting from the combination of modes present in the wavefront, the individual mode errors are added in quadrature,

$$\sigma \approx \sqrt{\Sigma_1^2 + \Sigma_2^2 + ... + \Sigma_n^2} \tag{2.17}$$

where n denotes the total number of modes present. For Kolmogorov turbulence we can approximate most of the energy to lie with in the first 30 or so spatial frequencies, equivalent to 3113 modes. Optimal Gerchberg-Saxton reconstruction is achieved when the wavefront residual approaches σ. The wavefront residual for a relatively dim source σ_{test} can then be scaled by the wavefront residual obtained for the bright source σ_{bright}.

$$\sigma_{test} = \sqrt{N_{bright}/N_{test}} * \sigma_{bright} \tag{2.18}$$

where N_{bright} and N_{test} are the number of photons available for the bright source and test source, respectively. An illustration of the Gerchberg-Saxton loop is shown in Figure 2.4. The amplitude and the phase are shown at the four Fresnel planes for the 50^{th} iteration of the Gerchberg-Saxton loop. The pupil plane phase, the reconstructed phase, and their residual is also shown. The relatively flat residual of 0.14 radian RMS integrated over the pupil shows how good the reconstruction is.

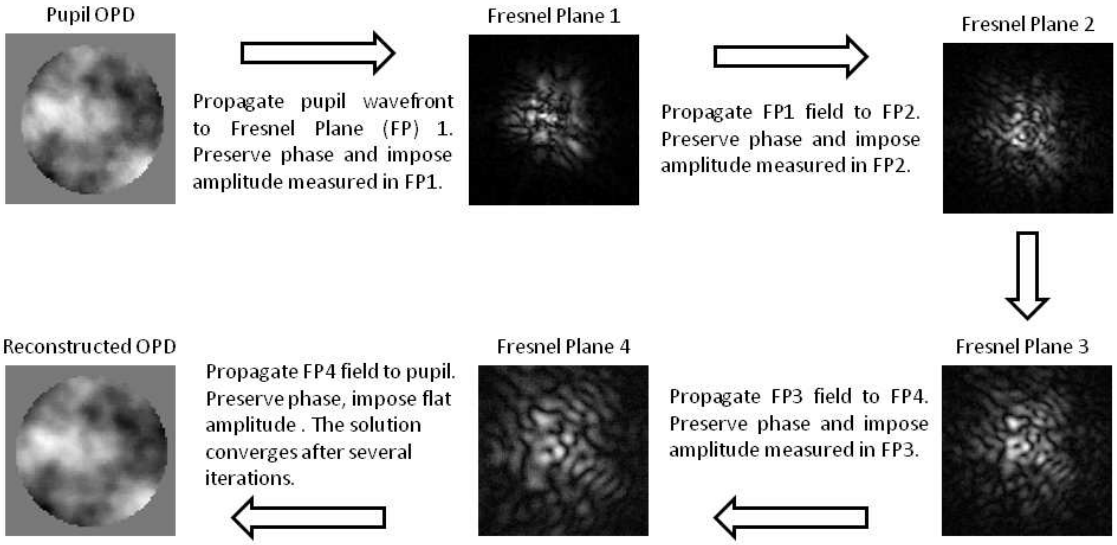

Figure 2.3: The Gerchberg-Saxton reconstruction algorithm is illustrated. The pupil plane optical path difference (OPD) shown in the top right corner is propagated to Fresnel plane (FP) 1 where the phase acquired due to propagation is preserved and the amplitude thrown out. The amplitude measured at FP 1 is imposed and a complex field is constructed using the propagated phase and the measured amplitude. The complex field in FP 1 is propagated to FP 2. A complex field similar to the one constructed in FP1, is constructed at each of the consecutive FPs and the field at the final FP (here FP 4) is propagated back to the pupil plane. At the pupil plane a flat field is imposed. It takes several iterations of the Gerchberg-Saxton loop to converge to the pupil plane phase.

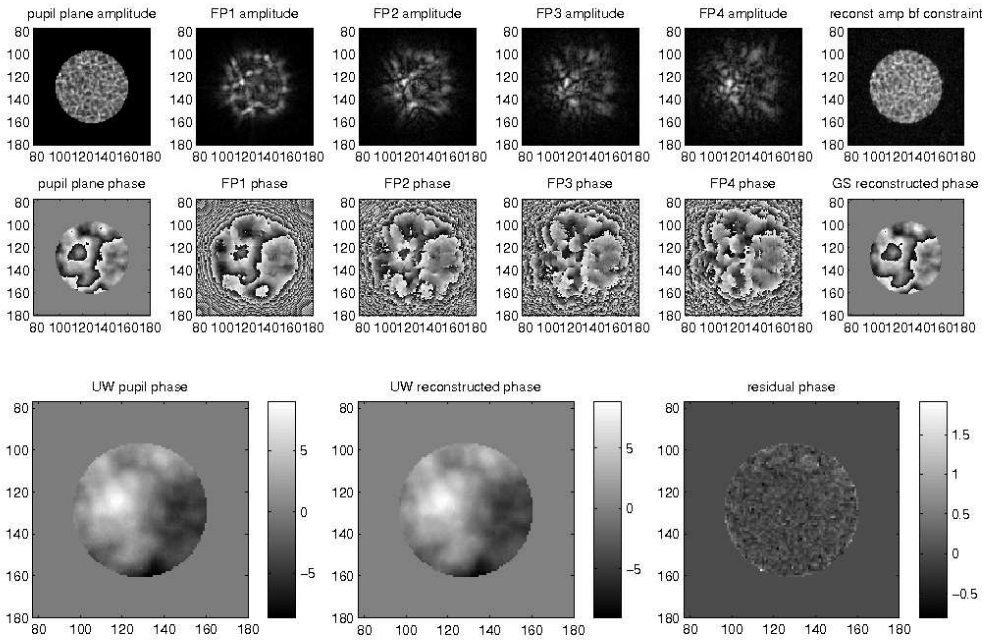

Figure 2.4: nlCWFS Gerchberg-Saxton reconstruction. The top row shows the amplitude in the pupil and at each of the Fresnel planes. The middle row shows the phase in the pupil and in each of the Fresnel planes. The third row shows the input phase, the reconstructed phase and the residual between the two. Reconstruction after 50 iterations of the Gerchberg-Saxton loop is shown.

2.2.2. Shack-Hartmann Wavefront Sensor

The Shack-Hartmann gradient sensor consists of an array of identical positive lenslets, placed in the pupil of the optical beam to be measured. The lenslets cover the entire aperture and correspond to the number of sub-apertures across the wavefront sensor. An unresolved point source serves as a reference and can be separately brought to focus by each lenslet, thus producing an array of spots in the focal plane [16]. When a plane wave is incident on the aperture, each spot is located on the optical axis of its corresponding lenslet. However when a distorted wavefront is incident on the aperture, the spots are displaced from their respective optical axis producing a local gradient, $\alpha(x, y)$, in x and y. In the focal plane each spot is displaced by a distance $s(x, y) = \alpha(x, y)\ f$, where f is the lenslet focal length. Fig 2.5 illustrates the SH sensing process, it shows the SH lenslet array which is placed in a conjugate pupil and the focal plane where the CCD records the image. The figure shows the image forming on SH subapertures which are divided into 2×2 quad cells. Each quad cell consists of several CCD pixels, which are not shown. The SHWFS reconstruction is performed by determining gradients based on the central point spread function (PSF) spot displacement within a sub-aperture, and for each sub-aperture. The spot displacements due to three different wavefronts are shown in Fig. 2.5. A plane wavefront is incident on the SHWFS in Fig. 2.5 A. and it produces no spot displacement. A tilted wavefront is shown in Fig. 2.5 B. which moves all the spots linearly along the y-axis. An aberrated wavefront shown in Fig. 2.5 C. displaces all the spots in different directions. A reconstruction matrix is computed based on the gradients. For this dissertation, SHWFS reconstruction was performed using the wave-optics package WaveProp [4]. Phase reconstruction with a 32 subaperture SHWFS is shown in Figure 2.6.

2.3. Fourier Decomposition

In this section I talk about Fourier modes, how phase can be decomposed into Fourier modes, and the use of Fourier modes to reconstruct the wavefront. The eventual goal of a wavefront

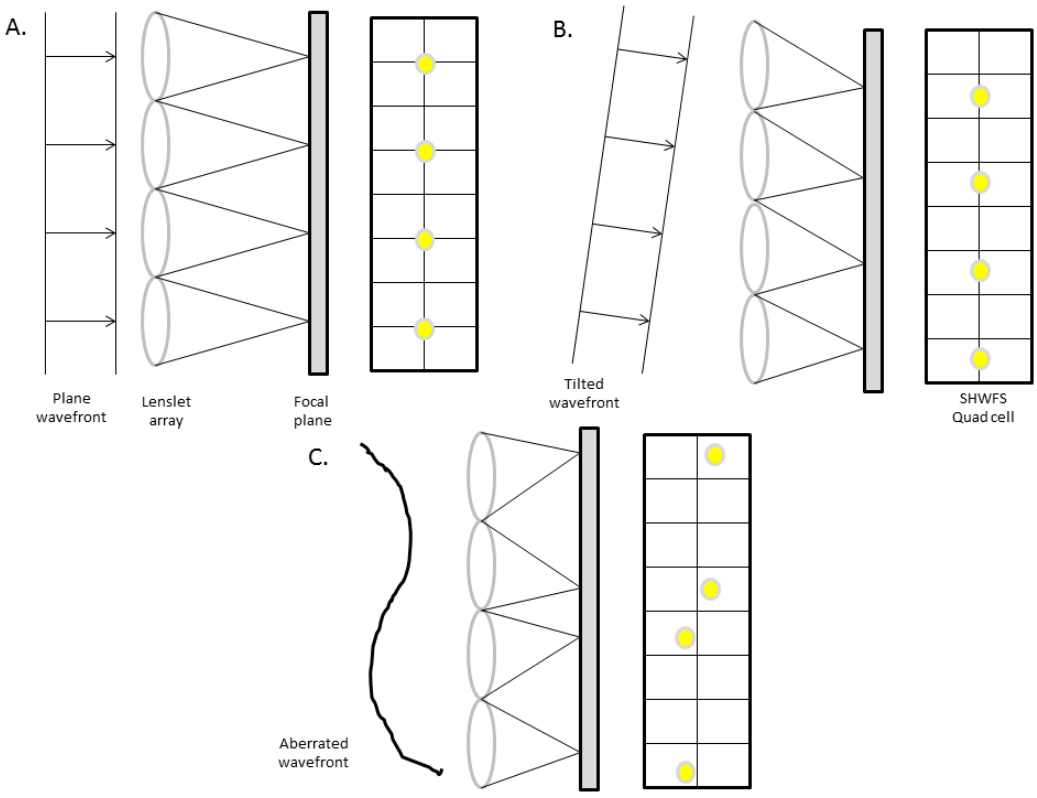

Figure 2.5: The Shack-Hartmann Wavefront Sensor (SHWFS) elements are shown. An identical array of lenslets is placed in a conjugate pupil and a CCD is placed in the focal plane of the lenslet array. Each subaperture can consist of several CCD pixels. The figure shows a four SH subapertures comprising of a 4 CCD pixels each. Figure A. shows a plane wave incident on the lenslet array, it causes no displacement in the focal plane spots. Figure B. shows a tilted wave incident on the lenslet array, it causes linear displacement of the spots along the y-axis. Figure C. shows an aberrated wave incident on the lenslet array, it produces different displacements in all of the focal plane spots. The focal plane spot displacements are converted into x and y gradients.

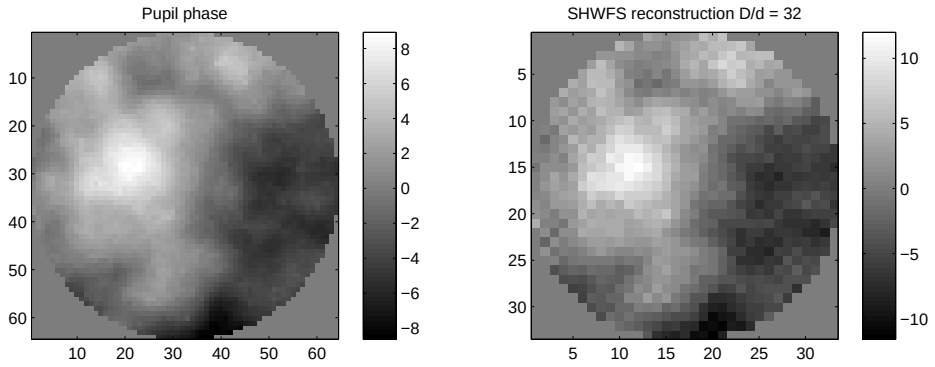

Figure 2.6: SHWFS reconstruction for $D/d = 32$, where D is the telescope aperture and the d is the size of the Shack Hartmann subaperture. The input pupil phase and the SH reconstructed phase are shown. A single realization of the atmosphere is considered.

sensor is to reconstruct the wavefront and Fourier reconstruction is one method to do so. Fourier decomposition instead of Zernike decomposition of the pupil plane phase is carried out. Zernike decomposition is widely used in optical astronomy where the measured image irradiance I_i is a convolution of the object irradiance I_o with the PSF $|h|^2$ [9]:

$$I_i = |h|^2 * I_o \tag{2.19}$$

where h^2 is the irradiance PSF, and $*$ is the convolution symbol. In the spatial frequency domain the incoherent pupil plane spectrum is correspondingly obtained by multiplying the Fourier transform of the source irradiance with the optical transfer function (OTF) [9]:

$$\mathcal{F}[I_i] = [H \star H][G_o \star G_o] \tag{2.20}$$

here G_o is the spectrum of I_o, H is the OTF, and $\star$ is the auto-correlation symbol. The telescope aperture considered in this work, and most telescope apertures are in fact circular in shape. The

Fourier transform of the circular aperture gives the PSF and the inverse Fourier transform gives the OTF which returns the circular aperture. Since my goal is to decompose the spectrum contained in this circular aperture, into modes it is straight forward to select a basis set which is orthogonal on a circular aperture, like Zernike modes. Fourier modes are not orthogonal on a circular aperture and therefore lead to a more complex decomposition approach. Fourier modes, are however a more natural choice. All pupil plane wavefronts represented in the spatial domain have a corresponding spectral representation in the image plane. The pupil and image plane wavefronts are Fourier pairs. Decomposing the pupil plane wavefront in to Fourier modes taps into the natural relationship that exists between frequency spectrum and image intensity and therefore more effectively represents atmospheric turbulence.

To represent the pupil plane phase differences as a set of Fourier modes one must solve the equation $BF = P$ where F is an array of Fourier coefficient amplitudes, B represents the Fourier basis set matrix, and P is an array comprised of the 2D phase map collapsed in to a single dimension (N^2). The matrix B has dimension $M \times N^2$, where M is the number of modes used to reconstruct the phase map. We measure the phase map P and generate the Fourier basis set B. The Fourier coefficient amplitudes F of size M are obtained by multiplying the phase map by the inverse of the Fourier basis set, $F = B^{-1}P$. The fact that B is not orthogonal on a circular aperture, means that its eigenvectors are not independent. In other words B is a singular matrix that cannot be diagonalized or inverted. A pseudo inverse via singular value decomposition (SVD) needs to be performed. If B was a symmetric matrix we could write its eigenvalue equation as:

$$Q^{-1}BQ = \Lambda = \begin{pmatrix} \lambda_1 & & & \\ & \lambda_2 & & \\ & & \ddots & \\ & & & \lambda_N \end{pmatrix} \tag{2.21}$$

$$B = Q\Lambda Q^{-1} \tag{2.22}$$

where Q contains the eigenvectors of the symmetric matrix B. Λ is the eigenvalue matrix which contains the eigenvalues λ of B along its diagonal. Since B is not symmetric we can not directly find its eigenvalues and are left with the option of finding its singular values. Two sets of singular matrices are constructed, U which contains vectors u of BB^t, and V which contains v of B^TB. Even though B is not a symmetric matrix BB^T and B^TB are symmetric matrices whose eigenvectors can be chosen orthonormal. Singular vectors $v_i, ...v_r$ are in the row space of B and the output vectors $u_1, ...u_r$ are in the column space of B. The singular values $\sigma_1, ...\sigma_r$ are all positive numbers which form the diagonal matrix Σ.

$$Bv_1 = \sigma_1 u_1, \quad ... \quad , Bv_2 = \sigma_2 u_2, \quad ... \quad , Bv_r = \sigma_r u_r \tag{2.23}$$

$$BV = U\Sigma \tag{2.24}$$

The square of the singular values are equal to the λs of Eq. 2.21. The singular values of BB^T and B^TB are $\sigma_i^2 = \lambda_i$ and if $Bv = \sigma u$ then $B^{-1}u = v/\sigma$. Singular values of the diagonal matrix Σ are plotted in Figure 2.9. The pseudo inverse $B^\dagger$ is given in Eq. 2.25. The Fourier coefficient amplitudes are obtained by multiplying the pseudo inverse $B^\dagger$ by the input phase map.

$$B^\dagger = V\ \Sigma^{-1}\ U^T \tag{2.25}$$

An $N \times N$ Fourier basis set B is constructed to equally represent the even and odd modes. The total number of spatial frequencies used to reconstruct the pupil plane phase depends on Nyquist sampling; for a 64×64 phase map, Nyquist sampling allows spatial frequencies with 32 cycles per aperture (CPA) to be resolved. The number of modes per spatial frequency depends on how many angular representations of a given spatial frequency are selected. Consider a wave represented as $e^{i\theta}$ and evaluated every $\theta = \frac{n*\pi}{2}$ radian, where n is an integer that ranges from 1 to $4 \times \#$ of CPA. According to this criteria each sine and cosine wave is sampled four times per CPA and so there will be four cosine and sine modes for a spatial frequency of 1 CPA, eight cosine and sine modes for

2 CPA, twelve cosine and sine modes for 3 CPA, so on and so fourth. For my specific basis set there are $\frac{N^2}{2} - \frac{N}{2}$ unique sine and cosine modes. I number the total modes generated to go from 1 to N^2 and empirically determine the zero frequency mode or piston to be at number $\frac{N^2}{2} - \frac{N}{2}$. An example of an 8×8 basis set shown in Fig. 2.7, illustrates cosine modes 1 to 28 and Fig. 2.8 illustrates sine modes 1 to 28. As a result of the periodicity of the cosine and sine functions and because cos(θ) = cos(-θ) and sin(-θ) = -sin(θ) there will be duplicate modes which must be eliminated in order to prevent underestimating a spatial frequency present in the pupil plane phase. Modes after the zero frequency repeat and are therefore excluded. The $(\frac{N^2-N)}{2})^{th}$ sine mode is also eliminated because it is zero and therefore has no contribution. In figures 2.7 and 2.8, SF 1 is represented by modes 19, 20, 21, and 27. Spatial frequency of 2 CPA consist of modes 10, 11, 12, 13, 14, 18, 22, and 26, making up a total of 8 sine and 8 cosine modes . Similarly spatial frequency of 3 CPA consists of modes 1 to 7, 9, 15, 17, 23, and 25, making up a total of 12 sine and 12 cosine modes. As a result of the angular orientation selected above each consecutive spatial frequency will contain an additional 8 modes. The modes are normalized to 1 radian root-mean- squared (RMS). A Fourier basis set of size 64×64, consisting of 4096 modes, is generated to decompose the simulated and laboratory-obtained phase maps. A selection of the 4096 modes is used to reconstruct the wavefront. Mode selection can depend on several parameters such as photon noise, sensor resolution, and on the frequency make-up of the turbulent wavefront. In the remainder of this section I explore these parameters and the effect they have on mode selection.

Photon noise enters the equation because the Fourier reconstructed wavefronts are eventually used to carry out a sensitivity comparison between the nlCWFS and the SHWFS. Sensitivity refers to the wavefront sensor's ability to convert a phase aberration into a signal which can be measured. A sensitive wavefront sensor measures minimum wavefront errors in the presence of photon noise. The sensitivity analysis is governed by Poisson statistics and is carried out by conducting a Monte-Carlo experiment on a turbulent wavefront for a thousand different photon noise realizations. For the simulations carried out in this dissertation 6.8×10^4 photons were used and the error due to photon noise goes as $1/\sqrt{N}$. The wavefront sensor's sensitivity to a particular mode is found by

Figure 2.7: Even or Cosine modes for an 8×8 Fourier basis set. There are a total of 28 cosine modes. A selection of the modes represent spatial frequencies of up to 3 cycles per aperture (CPA).

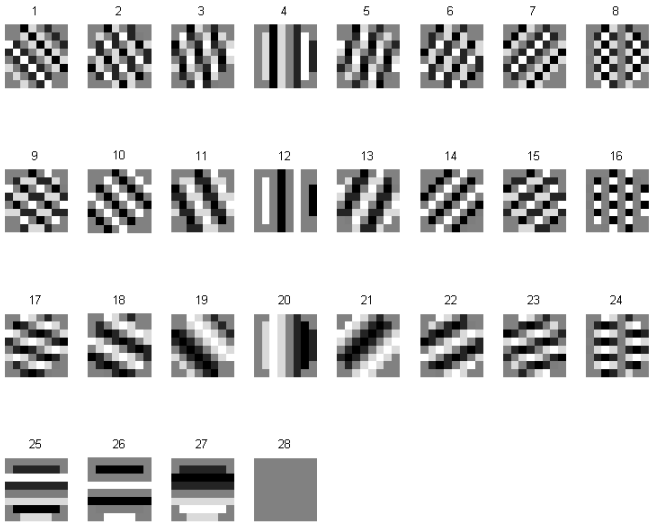

Figure 2.8: Odd or Sine modes for an 8×8 Fourier basis set. There are a total of 28 sine modes. a selection of the modes represent spatial frequencies of up to 3 cycles per aperture (CPA).

computing the standard deviation of the mode amplitude over a thousand measurements, where the only source of measurement error is photon noise. In this section I want to determine how well the Fourier reconstructor can reconstruct an individual mode in the photon limited regime. As a result of the presence of photon noise, Fourier reconstruction of a mode is mediated as a delicate balance between noise amplification and full modal recovery. There is a trade-off between, using a large number of singular values to compute the pseudo-inverse which allows full modal recovery, and using a small number of singular values so as to eliminate noise amplification. Figure 2.9 shows that most of the normalized diagonal singular values are close to one, however singular values beyond 2900 begin to drastically drop off and eventually approach zero. Figure 2.10 is a zoom in of Figure 2.9 and shows the variation in singular values between the cut-off values of 10^{-15} and 10^{-5}. Singular values with small amplitudes need to be multiplied by a large factor to recover the mode, this causes the the photon noise to also get multiplied by a large factor and leads to noise amplification. On the other hand selecting a high singular value cut-off to compute the pseudo-inverse, results in incomplete recovery of the Fourier modes. In selecting the singular value cut-off I want to retain enough singular values so as to fully reconstruct the spatial frequencies present in the wavefront with out adding too much noise.

I substantiate the claim, that when the singular value cut-off is set too high, incomplete modes are recovered, by experimenting with three cosine modes, SF3M4, SF6M5, and SF10M7, shown in Figures 2.11, 2.12, and 2.13 respectively. In the mode names, SF refers to spatial frequency and M refers to mode number. I want to check how the Fourier amplitude for the modes varies as the number of singular values selected in Σ changes. I Fourier reconstruct modes SF3M4, SF6M5, and SF10M7 while varying the cut-off value between 10^{-2}, 10^{-5}, and 10^{-10}. The modes are reconstructed with spatial frequencies ranging between 1 and 30 CPA. Figure 2.14 shows that for singular values selected above 10^{-2}, $100\,\%$ of mode SF3M4 is recovered for spatial frequencies of 3 and 4 CPA, $98\,\%$ of the mode is recovered for spatial frequency of 5 and 6 CPA, and $92\,\%$ to $85\,\%$ of the mode is recovered between spatial frequencies 7 to 16, respectively. Figure 2.15 shows that for singular values selected above 10^{-2}, $100\,\%$ of mode SF6M5 is recovered for spatial

frequency 6, $99\,\%$ of the mode is recovered for spatial frequency 7, and $95\,\%$ to $85\,\%$ of the mode is recovered for spatial frequencies 8 to 16, respectively. Figure 2.16 shows that for singular values selected above 10^{-2}, $100\,\%$ of mode SF10M7 is recovered for spatial frequency 10, $98\,\%$ for spatial frequency 11, and between $92\,\%$ and $86\,\%$ of the mode is recovered for spatial frequencies 12 to 16, respectively. For all three modes tested selecting the singular value cut-off to be above 10^{-2} or 10^{-5} leads to incomplete recovery of the modes at most spatial frequencies. When the singular value cut-off is above 10^{-10} $100\,\%$ of the modes are recovered for spatial frequencies up to 17. This preliminary analysis indicates that I should select singular values above 10^{-10} however this analysis is incomplete with out exploring the effect of noise amplification.

To see how the selection of singular values affects noise amplification I select 1 radian RMS of mode SF3M4 from above and perform a Gerchberg-Saxton reconstruction of the mode a thousand times, changing the photon noise realization at each iteration. The recovered mode is decomposed into 3113 Fourier modes spanning 30 spatial frequencies. The Gerchberg-Saxton and Fourier reconstruction of mode SF3M4 is shown in Figure 2.17. The standard deviation of the mode amplitude for SF3M4 is computed over the 1000 iterations. As the number of singular values used increases to include those with very small numbers the standard deviation drastically increases indicating noise amplification, see Fig.2.18. Selecting a singular value cut-off equal to 10^{-2} gives a relatively low standard deviation for the amplitude of mode SF3M4 over the first 16 spatial frequencies. Due to the noise amplification the singular value cut-off equal to 10^{-10}, which previously seemed ideal can no longer be used and the sensible choice is to use the singular value cut-off equal to 10^{-2}. When using the 10^{-2} cut-off value I have to compensate for the incomplete recovery of the mode. A compensation factor is determined for each of the 3113 modes used to reconstruct the phase and is applied when the mode amplitudes are calculated and later used for the sensitivity analysis in chapter 3.

The third and last parameter to explore for Fourier reconstruction is sensor resolution. For the SHWFS considered $\frac{D}{d} = 32$ limiting its spatial frequency range to 8 CPA at full resolution (i.e. 4 subapertures per wave) and to 16 CPA at Nyquist sampling (i.e. 2 subapertures per wave). The nlCWFS has 64 pixels across the aperture and is therefore sensitive to up to 16 CPA at full resolution (4 pixels per wave) and 32 CPA at Nyquist (2 pixels per wave). Even though the SHWFS Nyquist resolution is limited to 16 CPA I use spatial frequencies above 16 CPA to Fourier reconstruct the pupil plane phase. This is because the pupil plane wavefront, which is based on Kolmogorov turbulence, typically contains spatial frequencies above 16 therefore decomposing the wavefront into a larger number of spatial frequencies leads to better reconstruction. A comparison of Fourier reconstruction using 16 and 30 spatial frequencies, for the SHWFS and the nlCWFS, shows that using the higher number of spatial frequencies leads to lower wavefront residuals. Figure 2.19 shows that for the SHWFS when 16 spatial frequencies are used the RMS wavefront error is 0.71 radian and when 30 spatial frequencies are used the RMS wavefront error is 0.64 radian. There is almost a 10% improvement with the doubling of spatial frequencies. The experiment is repeated for the nlCWFS using an identical wavefront, source brightness, and photon noise realizations. Figure 2.20 shows that for the nlCWFS, Fourier reconstruction using 16 spatial frequencies results in an RMS wavefront error of 0.29 radian and using 30 spatial frequencies results in an RMS wavefront error of 0.16 radian. The nlCWFS reports a 46% improvement in wavefront reconstruction when the number of spatial frequencies used are almost doubled. In going from 16 to 30 CPA, the nlCWFS lowers the wavefront error $36\,\%$ more than the SHWFS. This is because the nlCWFS extracts phase information from speckles and utilizes the non-linear correlation that exists between high and low spatial frequencies to better reconstruct them. The nlCWFS therefore does a better wavefront reconstruction when it has information of the higher spatial frequencies. In conclusion even though the resolution of the wavefront sensors considered in this dissertation is 16 CPA; I use spatial frequencies of up to 30 CPA to perform the Fourier reconstruction. However, since the purpose of this dissertation is to carry out a sensitivity comparison between the nlCWFS and the SHWFS, the sensitivity analysis is limited to the first 16 spatial frequencies as no meaningful comparative result

can be obtained beyond the Nyquist resolution of the SHWFS.

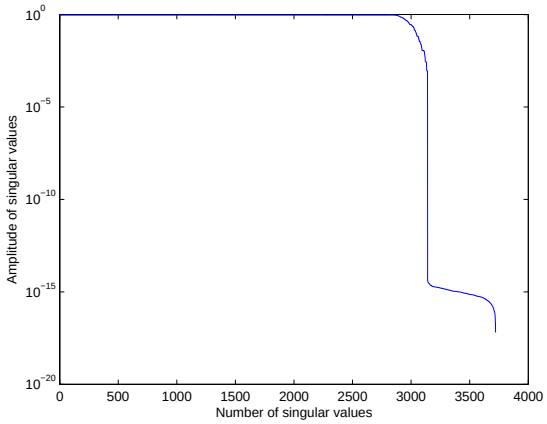

Figure 2.9: The plot shows singular values that make up the diagonal matrix Σ. The normalized amplitudes of the singular values range from $\approx 4 \times 10^{-16}$ to 1.

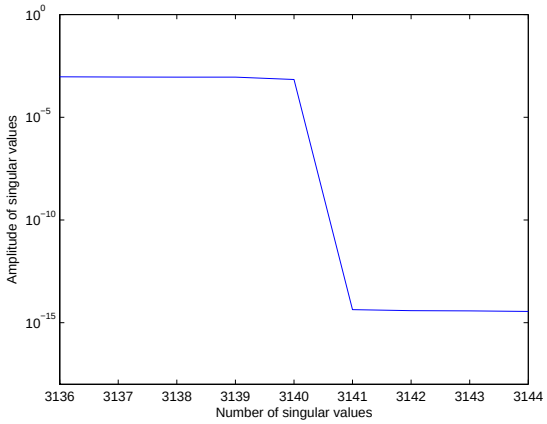

Figure 2.10: A zoom in of the singular value curve emphasizing the different singular values between the cut-off values of 10^{-15} and 10^{-5}.

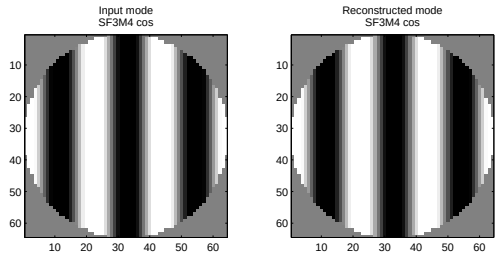

Figure 2.11: The original and reconstructed mode SF3M4 is shown. The mode is normalized to 1 radian RMS. The display intensity scale for both figures is between -1 and 1.

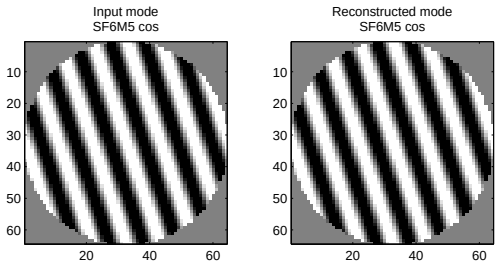

Figure 2.12: The original and reconstructed mode SF6M5 is shown. The mode is normalized to 1 radian RMS. The display intensity scale for both figures is between -1 and 1.

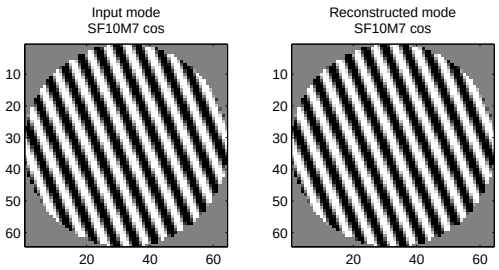

Figure 2.13: The original and reconstructed mode SF10M7 is shown. The mode is normalized to 1 radian RMS. The display intensity scale for both figures is between -1 and 1.

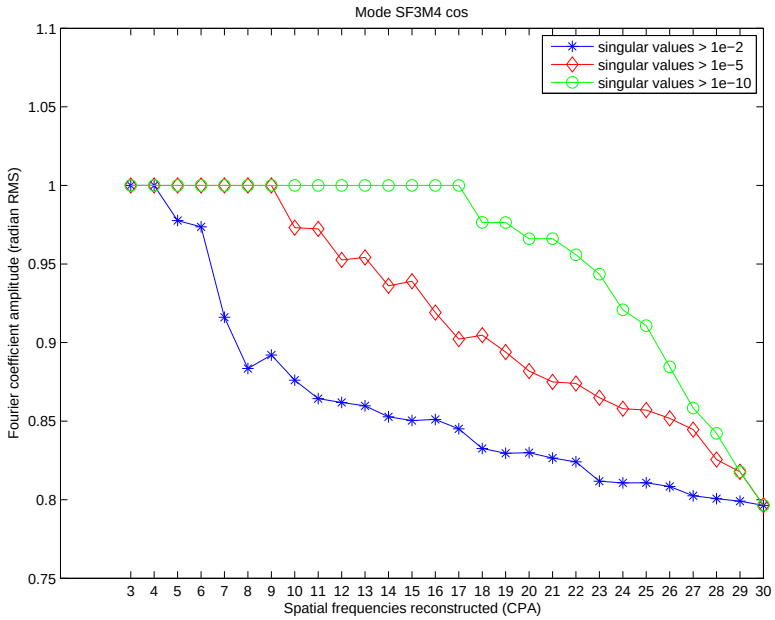

Figure 2.14: This graph shows modal reconstruction using three different cut-off values (10^{-2}, 10^{-5}, 10^{-10}) for the eigenvalues of the diagonal matrix Σ. Mode SF3M4 is reconstructed to 1 radian RMS. The Fourier coefficient amplitude of cosine mode SF3M4 is plotted as a function of spatial frequencies used to reconstruct the mode.

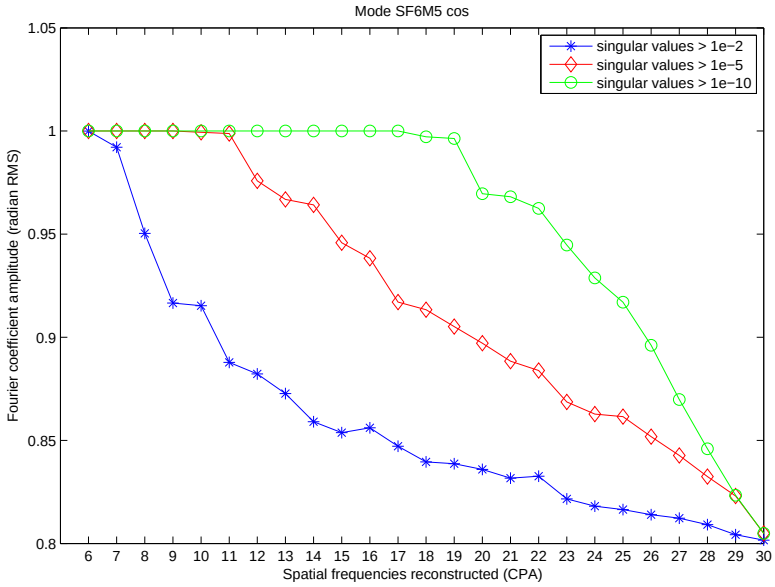

Figure 2.15: This graph shows modal reconstruction using three different cut-off values (10^{-2}, 10^{-5}, 10^{-10}) for the eigenvalues of the diagonal matrix Σ. Mode SF6M5 is reconstructed to 1 radian RMS. The Fourier coefficient amplitude of cosine mode SF6M5 is plotted as a function of spatial frequencies used to reconstruct the mode.

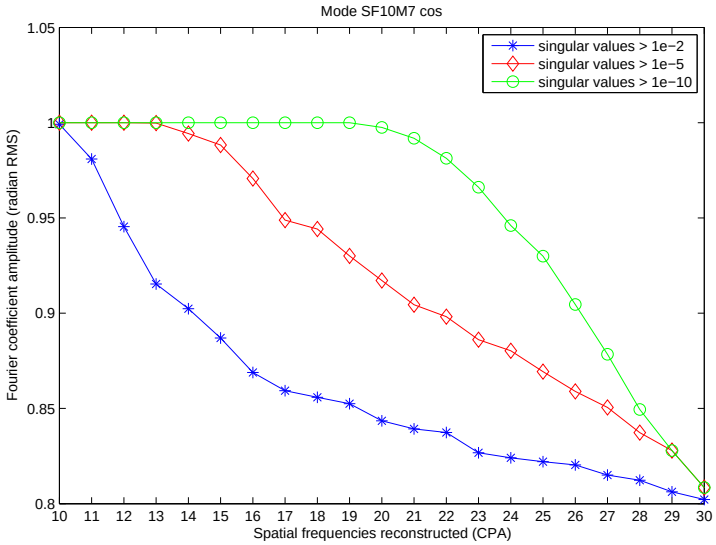

Figure 2.16:]

This graph shows modal reconstruction using three different cut-off values ($10^{-2},\ 10^{-5},\ 10^{-10}$) for the eigenvalues of the diagonal matrix Σ. Mode SF10M7 is reconstructed to 1 radian RMS. The Fourier coefficient amplitude of cosine mode SF10M7 is plotted as a function of spatial frequencies used to reconstruct the mode.

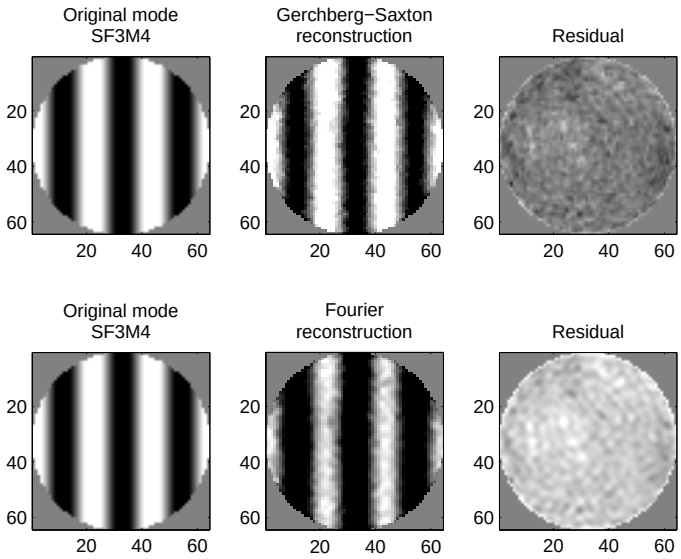

Figure 2.17: In the top row, the first figure shows mode SF3M4, the second figure shows the Gerchberg-Saxton reconstruction of mode SF3M4, and the third figure shows the residual. In the bottom row the first figure again shows SF3M4, the second figure shows Fourier reconstruction of mode SF3M4 using spatial frequencies up to 16 CPA, and the third figure is the residual. For the noise amplification analysis the Fourier reconstruction of mode SF3M4 is carried out using different singular value cut-offs; the results are shown in Fig. 2.18.

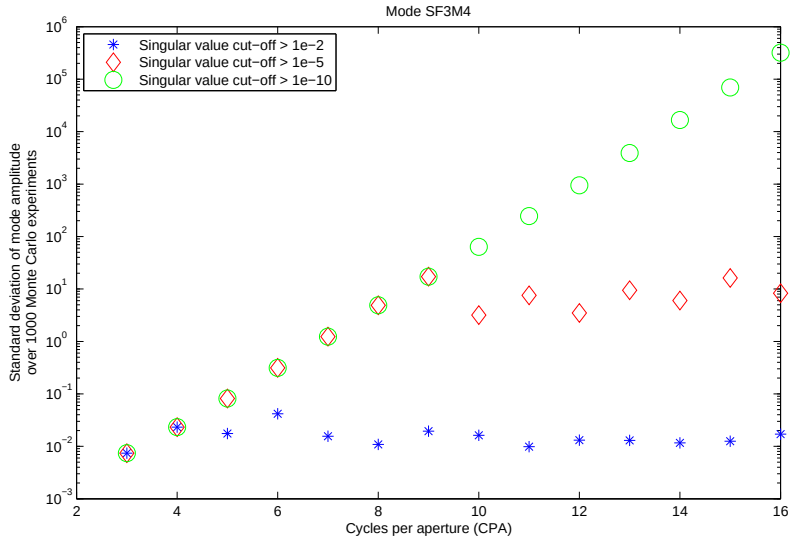

Figure 2.18: Noise amplification analysis. Mode SF3M4 is reconstructed via Gerchberg Saxton reconstruction 1000 times with a different photon noise realization for each iteration. Fourier reconstruction of the mode is then performed a 1000 times to obtain the mode amplitude for the three singular cut-off values under consideration. A standard deviation of the amplitude of mode SF3M4 is computed over the 1000 iterations. The standard deviation is plotted as a function of the spatial frequency for singular value cut-offs equal to 10^{-2}, 10^{-5}, and 10^{-10}. The standard deviation of the mode rises drastically for the later two singular value cut-offs indicating noise amplification.

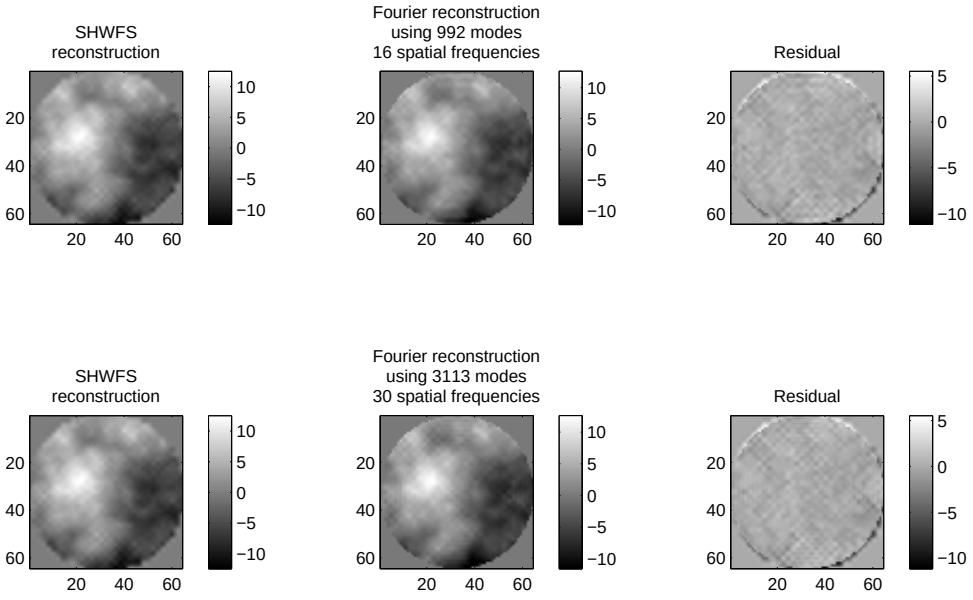

Figure 2.19:]
The figure shows Fourier reconstruction of the wavefront sensed by the SHWFS. A comparison is done between using 16 and 30 CPA. When spatial frequencies 1 to 16 CPA are used to Fourier reconstruct the wavefront the residual RMS is 0.71 rad. When spatial frequencies 1 to 30 CPA are used, the residual RMS is 0.64 rad. This demonstrates that the SHWFS benefits from using a larger number of spatial frequencies because using a larger number of spatial frequencies is more representative of the inherent makeup of the atmospheric spectrum.

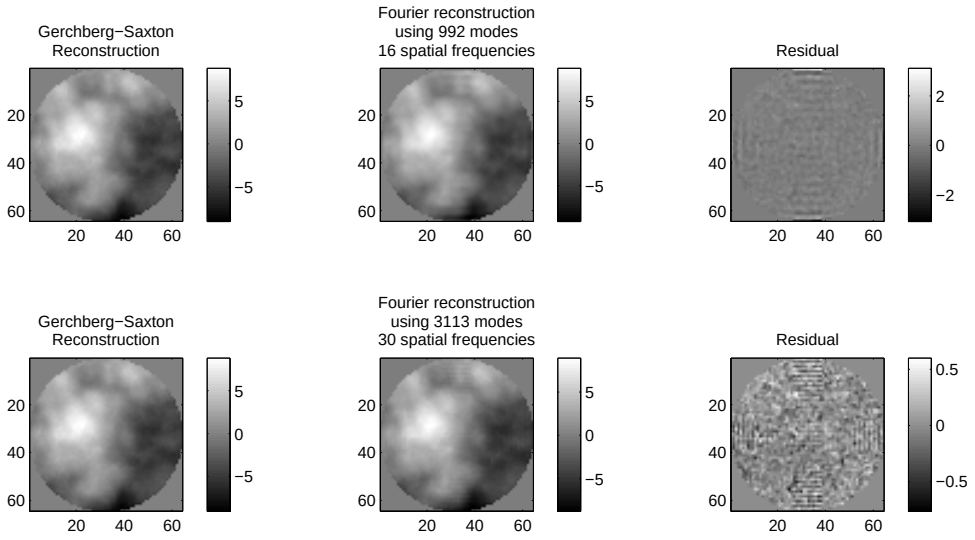

Figure 2.20: The figure shows Fourier reconstruction of the wavefront sensed by the nlCWFS. A comparison is done between using 16 and 30 CPA. When spatial frequencies 1 to 16 CPA are used to Fourier reconstruct the wavefront the residual RMS is 0.29 rad. When spatial frequencies 1 to 30 CPA are used, the residual RMS is 0.16 rad. This demonstrates that the nlCWFS benefits from using a larger number of spatial frequencies because it is able to utilize the non-linear correlation that exists between low and high spatial frequencies.

3. CHAPTER THREE

"A good idea is worth more than a large telescope"

- R. O. Redman

3.1. Wave Optics Simulation

Theoretical results based on perturbation analysis, carried out by Guyon [13] suggests that the nlCWFS is significantly more sensitive than the SHWFS at low spatial frequencies. To test the theory and compare the sensitivity of the nlCWFS with the SHWFS we carry out wave-optics simulations, using WaveProp [4] and AOTools toolboxes for $Matlab^{TM}$. The simulations performed are open loop as the goal here is to determine how well the wavefront can be sensed, not how well it can be corrected. An electromagnetic field of wavelength $790\,\text{nm}$ originates from a point source, $10^5\,\text{m}$ away and is propagated to the telescope. The size of the telescope aperture is $D = 1.5\,\text{m}$. The number of photons simulated for wavefront sensing is 6.7×10^4, which corresponds to $0.1\,\text{ms}$ integration time on a magnitude 10 source in a $0.16\,\mu\text{m}$ wide bandwidth with $20\,\%$ system efficiency. The simulated electromagnetic field consists of 256×256 grid points spread across $4 \times D$; 64×64 of the central grid points have phase information. Two phase screens are used to simulate a two-layer atmosphere prescribed with Kolmogorov statistics. Fried's coherence length r_0 for the two screens is the same but the but the C_n^2 profile is integrated over different path lengths. The Bufton wind profile is used and the velocity is set to $12.5\,\text{ms}^{-1}$. An example of realistic atmospheric parameters for the Starfire Optical Range is: atmospheric coherence length $r_0 = 0.075\,\text{m}$ and isoplanatic angle $\theta_0 = 9.4\,\mu\text{rad}$ at $500\,\text{nm}$. According to the scaling formulas given in Eq. 3.1 and Eq. 3.2 these atmospheric parameters translate to $D/r_0 = 12.7$, and $\theta_0 = 16.2\,\mu\text{rad}$ at $790\,\text{nm}$ when looking at zenith [16].

$$r_0(\lambda_2) = r_0(\lambda_1)\left(\frac{\lambda_2}{\lambda_1}\right)^{6/5} \tag{3.1}$$

$$\theta_0(\lambda_2) = \theta_0(\lambda_1) \left(\frac{\lambda_2}{\lambda_1}\right)^{6/5} \tag{3.2}$$

The Greenwood frequency at $790\,\text{nm}$ is $f_g = 171\,\text{s}^{-1}$. The tilt removed wavefront distortion for Kolmogorov turbulence averaged over an aperture of diameter D expressed as a root-mean-square (RMS) value in units of radians of optical phase is [16]:

$$< \phi >= 0.376 \left(\frac{D}{r_0}\right)^{5/6} \tag{3.3}$$

According to Eq. 3.3 for $D = 1.5\,\text{m}$ and $r_0 = 0.12\,\text{m}$ a realistic wavefront will have 3 radians of RMS error. The wavefront simulated for the sensitivity analysis has an RMS error equal to 3.48 radian and is shown in Fig. 3.1. The simulation parameters are listed in Table 3.1.

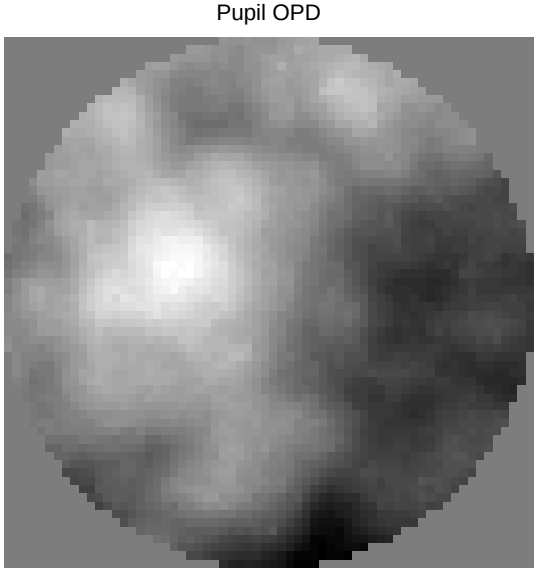

Figure 3.1: The simulated pupil plane wavefront after tilt removal has an RMS error of 3.48 radians.

The number of samples across the nlCWFS equal the number of grid points across the phase map, 64×64. The nlCWFS records intensity of the propagated electromagnetic field at four Fresnel planes (FP). In reality the Fresnel planes will be split in wavelength; for the simulations the same wavelength is used for all four Fresnel planes. This simplification is acceptable since the difference

in photons between the four wavelength splits is small and ranges between 5.9×10^{-4} and 6.7×10^{-4} photons. Since the light for the four Fresnel planes is meant to be split in wavelength and not intensity, all four detectors see all the incident light with the exception of interaction of light by intermediate surfaces. As a result in the simulations the detector at FP 1 receives $100\,\%$ of the incident photons. The remaining three detectors receive a fraction of the incident light to account for absorption and reflection by the intermediate dichroics and optics. The detectors at FP 2, FP 3 and FP 4 suffer the loss of $5\,\%$, $10\,\%$, and $15\,\%$ of the incident photons, respectively due to the addition of intermediate optics. I experimented with several Fresnel plane distances in my Gerchberg-Saxton [8] algorithm and found the following to give the best results. FP 1 is located $287.3\,$km from the pupil plane, FP 2 is located $574.6\,$km from the pupil plane, FP 3 is located $861.9\,$km from the pupil plane, and FP 4 is located $1149.2\,$km from the pupil plane, along the z-axis. The Fresnel plane selections correspond to Fresnel numbers of NF 1 = 25, NF 2 = 12, NF 3 = 8, and NF 4 = 6. The intensities recorded in the four FPs are used by the Gerchberg-Saxton algorithm to reconstruct the pupil plane wavefront through the method described in chapter 2. The SHWFS divides the telescope pupil in to 32 subapertures. Each SH subaperture d_{sa} consists of a 2×2 quad cell, the SHWFS reconstruction process is outlined in chapter 2. Simulations assume both detectors to be perfect with $100\,\%$ quantum efficiency and no read noise. The only source of error in the simulations is photon noise.

3.2. Mode Coupling Analysis for the non-linear Curvature Wavefront Sensor

The nlCWFS derives its information from speckles which are tight, bright, specks of light at small Fresnel distances and become diffuse spots of light at large Fresnel distances. The speckles correlate high and low spatial frequencies in a non-linear manner and it is important to determine whether the Gerchberg-Saxton or the Fourier reconstruction leads to mode coupling. If there is evidence of mode coupling in either of the processes it needs to be properly addressed and accounted for in the sensitivity analysis. To test whether or not there is mode coupling I reconstruct two types of wavefronts, one is the original wavefront which consists of the pupil plane aberrated phase and

Table 3.1: Simulations Parameters

Parameter	nlCWFS	SHWFS
Telescope diameter	1.5 m	
WFS wavelength	790 nm	
RMS wavefront error	3.48 rad	
Integration time	0.001 s	
Source brightness	6.7×10^4 photons	
Fried's coherence length	0.12 m @ 790 nm	
Isoplanatic angle	16.2 μrad @ 790 nm	
Greenwood frequency	171 s^{-1} @ 790 nm	
WFS detector readout noise	0	
WFS detector quantum efficiency	1	
WFS subapertures	not applicable	32
Fresnel plane distances	287 km, 575 km, 862 km, 1149 km	not applicable
WFS detector sampling	64 pixels across pupil	2×2 pixels per subaperture
Spatial frequency control range	16 CPA at 2×Nyquist 32 CPA at Nyquist	8 CPA at 2×Nyquist 16 CPA at Nyquist

the second is the perturbed wavefront which is generated by adding 0.1 radian of a single mode to the original wavefront. Two modes, SF3M4 and SF10M7 used for the perturbation analysis, are shown in Figure 3.2. The original wavefront is shown in Figure3.3A, 0.1 radian of mode SF3M4 is added to the original wavefront to create the perturbed wavefront in Figure 3.3B. The difference between the original and the perturbed wavefronts is shown in Figure 3.3C where mode SF3M4 plus some noise is recovered. The recovered mode has an RMS value of 0.175 radian averaged over the circular pupil compared to the 0.1 radian RMS value of the original mode. Similarly 0.1 radian of mode SF10M7 is added to the the original wavefront shown in Figure 3.4A to create the perturbed wavefront shown in Figure 3.4B. The difference between the original and the perturbed wavefronts is shown in Figure 3.4 . The RMS of residual integrated over the circular aperture is 0.175 radian compared to the 0.1 radian RMS value of mode SF10M7 added as the perturbation. A difference of 0.075 radians is with in the photon noise limit and tells us that the Gerchberg-Saxton reconstruction does not suffer from mode coupling.

I now move on to analyzing whether or not there is Fourier mode coupling. The difference between the Fourier reconstructed perturbed map and the original phase map is taken to see whether the added mode is retrieved. Figure 3.3D & Fig. 3.4D show the Fourier reconstruction

of the original phase map. Fourier reconstruction of the perturbed phase map is shown in Figure 3.3E where the perturbation equals 0.1 radian of mode SF3M4, and in Figure 3.4E where the perturbation equals 0.1 radian of mode SF10M7. The difference, between the Fourier reconstructed perturbed map and the original phase map shown in Figure 3.3F and Figure 3.4F is taken to see whether respectively, mode SF3M4 and mode SF10M7 are recovered. In both cases the mode recovered from the perturbation analysis has a value of 0.174 radian RMS integrated across the circular aperture compared to 0.1 radian RMS of the original mode used for the perturbation. The results show that after Fourier reconstruction the mode is recovered with in the photon noise limit. If there was mode coupling we would not have been able to recover the individual mode, instead we would see contributions from other modes in addition to the mode that was added. The fact that there is no mode coupling means that the Gerchberg Saxton and the Fourier decomposition processes accurately ascribes energy to the spatial frequencies present in the pupil plane wavefront.

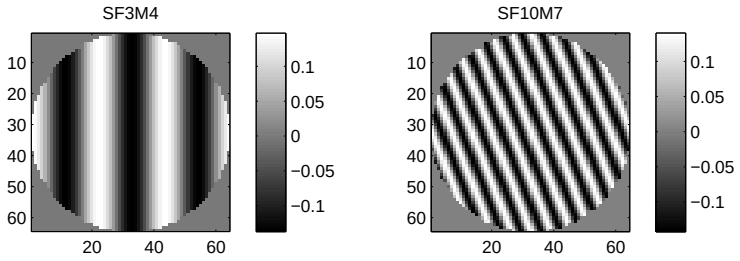

Figure 3.2: The first figure shows 0.1 radian of mode SF3M4 which is the fourth mode of spatial frequency 3. The second figure shows 0.1 radian of mode SF10M7 which is the seventh mode of spatial frequency 10.

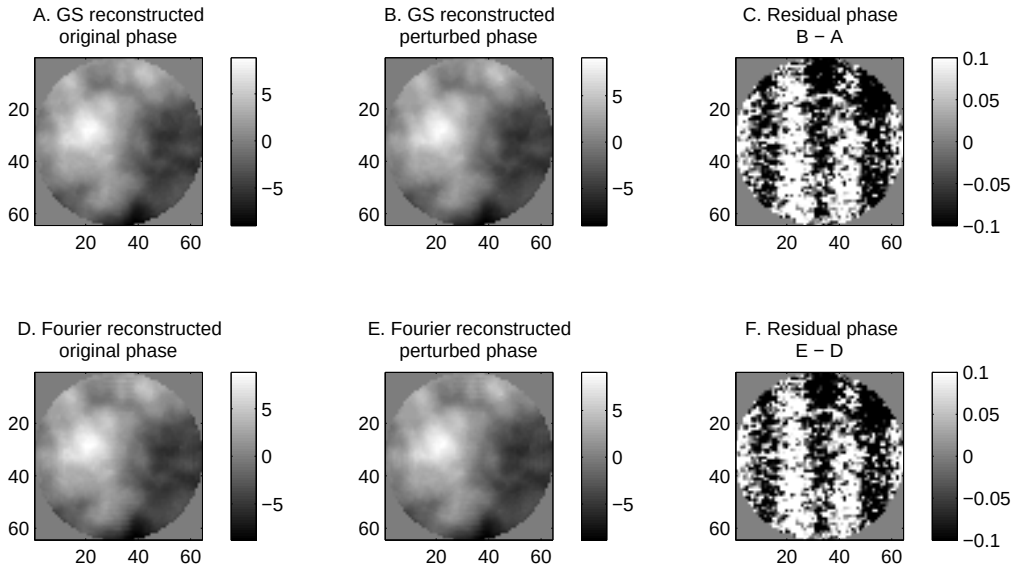

Figure 3.3: Mode coupling analysis. Figure A is the Gerchberg-Saxton (GS) reconstruction of original phase map. The original phase map is then perturbed with 0.1 radian RMS of cosine mode SF3M4. Figure B shows the GS reconstruction of the perturbed phase. Figure C is the residual, computed from subtracting A from B, showing that the perturbed mode is recovered. Figures D and E are the Fourier reconstruction of the original and perturbed phase maps. Figure F is the residual computed from subtracting E from D. Figure F shows that the perturbed mode SF3M4 cos is recovered after Fourier reconstruction.

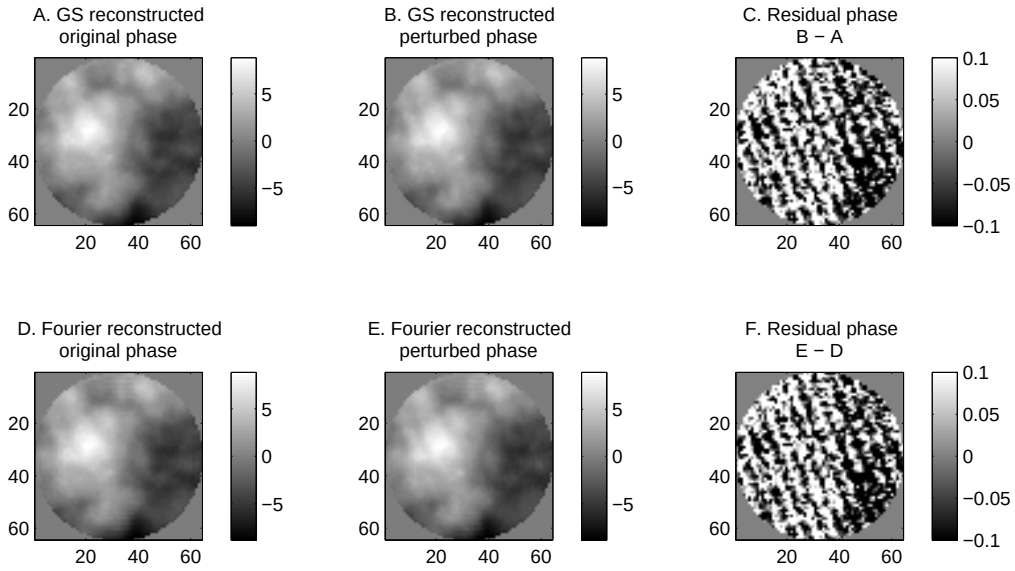

Figure 3.4: Mode coupling analysis. Figure A is the Gerchberg-Saxton (GS) reconstruction of original phase map. The original phase map is then perturbed with 0.1 radian RMS of cosine mode SF10M7. Figure B shows the GS reconstruction of the perturbed phase. Figure C is the residual, computed from subtracting A from B, showing that the perturbed mode is recovered. Figures D and E are the Fourier reconstruction of the original and perturbed phase maps. Figure F is the residual computed from subtracting E from D. Figure F shows that the perturbed mode SF10M7 cos is recovered after Fourier reconstruction.

3.3. Sensitivity Comparison

To carry out a sensitivity comparison between the nlCWFS and the SHWFS, I determine the ability of each sensor to reconstruct the spatial frequencies present in the pupil plane wavefront. The pupil plane spectrum is a combination of several Fourier modes and the ideal wavefront sensor is able to reconstruct all the Fourier modes with minimal error. The following formula relates two physical quantities, Σ and N through the scalar β [11],

$$\beta = \Sigma * \sqrt{N} \tag{3.4}$$

here Σ is the error per Fourier mode given in radians, N is the number of photons incident on the detector, and β represents the sensitivity of the wavefront sensor to a Fourier mode. If photon noise is the only contributing source of error then I can determine the error per Fourier mode given a signal-to-noise-ratio (SNR). For a fixed SNR a lower error or Σ implies a lower β which in turn implies that the WFS requires fewer photons to reconstruct a Fourier mode and is thus a more sensitive WFS.

A Monte Carlo experiment is conducted in which the pupil plane wavefront is generated a thousand times, with photon noise being the only variable parameter between iterations. The thousand wavefronts are reconstructed with each of the sensors and then decomposed into Fourier modes. The standard deviation of the Fourier mode amplitude is determined over the thousand iterations and gives the error per mode, which is Σ from Eq. 3.4. In the case of the nlCWFS photon noise is added at each Fresnel plane. For the SHWFS photon noise is added at a single detector plane. The detectors are modeled to be noise free and have a quantum efficiency of 1, therefore the only source of error is photon noise.

For the sensitivity analysis I want to determine the error or standard deviation, due to photon noise, in reconstructing each Fourier mode. I compute the standard deviation of the amplitude of the 3113 Fourier modes over a thousand iterations and compute β per spatial frequency for the nlCWFS and the SHWFS. The number of photons needed to reconstruct each Fourier mode to 1

radian RMS is equal to β^2. For the nlCWFS and the SHWFS β^2 is plotted as a function of spatial frequency in Figure 3.5. The Wavefront sensor sensitivity is determined for up to 16 spatial frequencies. The simulated results show that at the lowest spatial frequency the nlCWFS requires ≈ 71 times fewer photons than the SHWFS. On average the nlCWFS requires 12 times fewer photons than the SHWFS to reconstruct spatial frequencies of 1 to 10 cycles per aperture (CPA). Theoretical estimates based on perturbation analysis predict that, on average, the nlCWFS requires ≈ 14 times fewer photons than the SHWFS to reconstruct the first 10 spatial frequencies [13]. The simulated results agree well with the theoretical predictions. I note that the source brightness and other parameters used in the theoretical analysis slightly differ from the more realistic, site, and telescope specific parameters used in the simulations. For instance the theoretical source is much brighter than the more realistic source used in the simulations, making the simulated source brighter will only improve the results as the error per mode will decrease. The theoretical RMS wavefront error is ≈ 4 radian compared to the 3.48 radian used for the simulations; the small difference does not effect the results. The theoretical wavelength is 850 nm compared to the 790 nm used in simulations, and the telescope diameter used in the theoretical analysis is 8 m compared to the 1.5 m used in simulations. Despite the minor differences the sensitivity analysis can be compared for similar RMS wavefront errors. Details of the number of photons required by each wavefront sensor to reconstruct a given spatial frequency are listed in Table 3.2. The results obtained are quite encouraging and indicate that using the nlCWFS instead of the SHWFS will make it possible to observe dimmer exoplanets, as the nlCWFS requires significantly fewer photons to sense the wavefront.

Table 3.2: Sensitivity Comparison between the nlCWFS & the SHWFS

Spatial Frequency (CPA)	nlCWFS (photons)	SHWFS (photons)	Simulation $\frac{N_{SHWFS}}{N_{nlCWFS}}$	Theoretical[1] $\frac{N_{SHWFS}}{N_{nlCWFS}}$
1	10.9	695.2	63.4	71.4
2	7.1	171.2	24	25.0
3	6.6	72.5	11	15.0
4	6.0	40.9	6.8	9.0
5	5.9	26.5	5.9	6.5
6	5.6	19.1	3.4	5.0
7	5.4	14.6	2.7	3.5
8	5.3	11.7	2.2	3.5
9	5.3	9.7	1.8	3.0
10	5.3	8.3	1.6	3.0
11	5.0	7.1	1.4	not available
12	4.5	6.3	1.4	not available
13	4.1	5.6	1.4	not available
14	4.0	5.2	1.3	not available
15	4.0	5.3	1.3	not available
16	4.0	6.0	1.5	not available

The theoretical source is brighter than the simulated source and the theoretical RMS wavefront error is ≈ 4 radian compared to the 3.48 radian used for the simulations.[1]

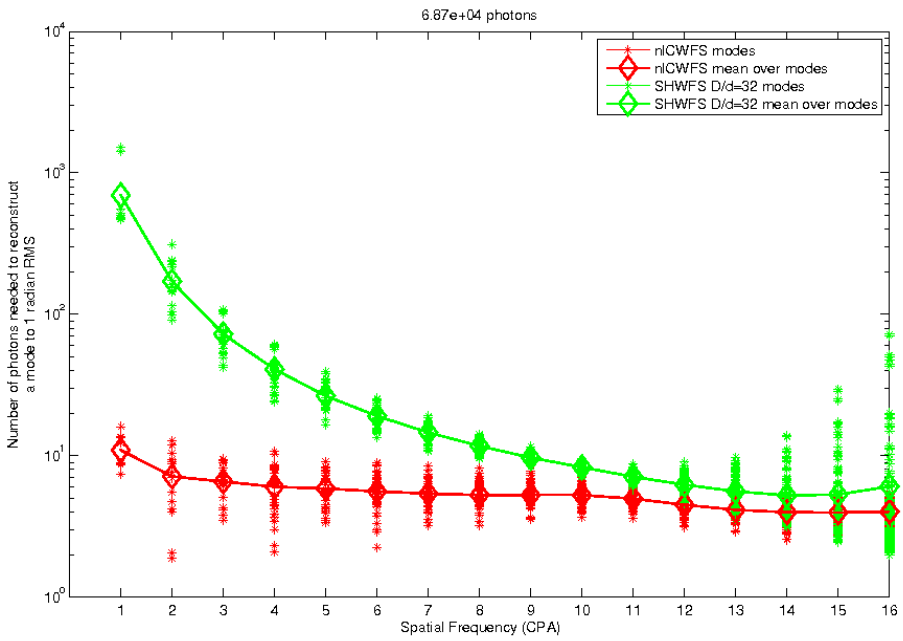

Figure 3.5: Comparison of the nlCWFS sensitivity with the SHWFS. The number of photons needed to reconstruct a mode to 1 radian RMS is plotted as a function of the CPA, for up to 16 spatial frequencies. The sensitivity curve for the nlCWFS is shown in red and that for the SHWFS is shown in green. The $*$ indicate the number of photons needed to reconstruct the modes. The $*$ represent the individual modes present in a spatial frequency. The diamond show the mean of the modes over the particular spatial frequencies.

3.4. Deriving Contrast

The goal of this dissertation is not only to detect dim objects but to detect dim objects nearby bright ones. We want to be able to image an exoplanet in close proximity to its host star and therefore are interested in obtaining a high contrast between the central PSF core and the surrounding envelope where an exoplanet may orbit. In this section we derive an expression for the contrast between the central star and the exoplanet that lies at an angular separation α.

A wavefront distorted by Kolmogorov turbulence may be described by its structure function as [16]:

$$D_\phi(r) = 6.88 \left(\frac{r}{r_0}\right)^{5/3} \tag{3.5}$$

here r_0 is Fried's coherence length. The Wiener spectrum $\phi(f)$ of the phase fluctuations is related to the structure function by:

$$D_\phi(r) = 2 \int df\ \phi(k)\ [1 - \cos(2\pi f \cdot r)] \tag{3.6}$$

from which the Wiener spectrum is found to be:

$$\phi(k) = \frac{0.023}{r_0^{5/3}\ f^{5/3}} \tag{3.7}$$

here f denotes spatial frequency and the Wiener distribution represents the power spectral density of the atmosphere. This is also referred to as the atmospheric transfer function. In order to determine the optical transfer function (OTF) for the whole imaging system the atmospheric transfer function is combined with the telescope transfer function. The combined OTF describes the complex amplitude of the received wavefront as a function of the spatial frequencies present in the optical aperture. The OTF can be computed from the phase structure function of the compensated wavefront. For a telescope aperture of diameter D, having an incident wavefront $W(\mathbf{r}) = e^{i\phi(\mathbf{r})}$, the OTF is [16]

$$OTF(\rho) = \frac{\int_D \int_D W(\mathbf{r}')\ W^*(\mathbf{r})\ d\mathbf{r}\ d\mathbf{r}'}{\int_D \int_D |W(\mathbf{r})|^2 d\mathbf{r^2}} \tag{3.8}$$

$$= \frac{1}{D^2} \int_D \int_D e^{i[\phi(\mathbf{r}')-\phi(\mathbf{r})]} d\mathbf{r} d\mathbf{r}' \tag{3.9}$$

here **r** is the 2D position in the aperture and ρ represents the displacement in the aperture. The corresponding spatial frequency in the image plane $f = \frac{\rho}{\lambda_i f'} = \frac{\alpha}{\lambda_i}$, where λ_i is the imaging wavelength, f' is the focal distance to the image plane, and $\alpha = \frac{\rho}{f'}$ is the angular displacement. The amplitude of a sine wave component of spatial frequency f is [11]:

$$A(f) = \frac{0.22\ \lambda_0}{f^{11/6}\ D\ r_0^{5/6}} \tag{3.10}$$

$A(f)$ represents the Fourier transform of the OTF and is referred to as the PSF. Fresnel propagating a complex field alternately produces a cosine component which represent OPD and a sine component which represents pure amplitude. The OPD component $A(f)_{OPD}$ and the amplitude component $A(f)_{amp}$ are [11]:

$$A(f)_{OPD} = \frac{0.22\ \lambda_0}{f^{11/6}\ D\ r_0^{5/6}}\ \sqrt{X(f,\lambda_i)} \tag{3.11}$$

$$A(f)_{amp} = \frac{2\pi\ 0.22\ \lambda_0}{f^{11/6}\ D\ r_0^{5/6}}\ \sqrt{Y(f,\lambda_i)} \tag{3.12}$$

where λ_0 is the wavelength at which r_0 is measured. $X(f,\lambda_i)$ and $Y(f,\lambda_i)$ are found by multiplying the respective propagated wavefronts by the C_n^2 profile, integrating over altitude and normalizing. For low altitude turbulence and/or low spatial frequencies, the Fresnel propagation distance is too short to allow for scintillation therefore $X(f,\lambda_i) = 1$ [11]. The intensity measured by an optical system as a result of a small phase aberration $d\phi$ is [27],

$$I(x,y) = |\text{PSF}(x,y)\ *\ \mathcal{F}[\exp(i\ d\phi(\boldsymbol{u})) - 1]|^2 \tag{3.13}$$

where the PSF is the ideal point spread function, $*$ is the convolution operation, $\mathcal{F}$ is the Fourier transform operator, and $\boldsymbol{u}$ is the 2D spatial frequency coordinate. If the phase error is small ($d\phi << 1$) then the resulting intensity is proportional to the Fourier transform of the phase error

$$I(x,y) \approx |\text{PSF}(x,y) \ * \ \mathcal{F}(d\phi(\boldsymbol{u})|^2 \tag{3.14}$$

consider a simple sine phase error

$$d\phi(\boldsymbol{u}) = \frac{2\pi h}{\lambda_i}\text{sin}(2\pi \boldsymbol{u}) \tag{3.15}$$

where h is the amplitude of a cosine wave in the aperture, such that $h << \lambda$. The cosine phase aberration will create two symmetric speckles on either side of the ideal PSF [11]

$$I(\alpha) = \text{PSF}(\alpha) + \left(\frac{\pi h}{\lambda_i}\right)^2 [\text{PSF}(\alpha + \text{f}\lambda_i) + \text{PSF}(\alpha - \text{f}\lambda_i)] \tag{3.16}$$

Contrast is found by taking the ratio of the ideal PSF and the off-axis PSF obtained at an angle α. By substituting $A(f)_{OPD}$ from Eq. 3.11, for h in Eq. 3.16, and making the substitution $f = \alpha/\lambda_i$, the contrast for the OPD component is obtained:

$$C_0(\alpha) = \frac{0.478 \ \lambda_0^2 \ \lambda_i^{5/3} \ X(\alpha/\lambda_i, \lambda_i)}{\alpha^{11/3} \ D^2 \ r_0^{5/3}} \tag{3.17}$$

In this dissertation, for a closed loop system, only two sources of error, photon noise and time lag are considered. Photon noise obeys Poisson statistics and depends on source brightness F, WFS sensitivity β, collection area A, and integration time t_{int}. Therefore the error due to photon noise is:

$$\Sigma = \frac{\beta}{\sqrt{N_{ph}}} \ = \frac{\beta}{\sqrt{F t_{int} A}} \ = \frac{\beta}{\sqrt{F t_{int} \pi D^2}} \tag{3.18}$$

here N is the number of photons, F is source flux in units of photons per area per time, A is area in units of meters squared, and t is integration time in seconds. The second error is due to time lag

between sensing and correcting the wavefront and the time scale on which atmospheric turbulence changes. This is computed by considering a sine wave of amplitude $A(f)$ and spatial frequency f.

$$A(f)\ \sin(2\pi \boldsymbol{u} f) \tag{3.19}$$

here $\boldsymbol{u}$ is the two dimensional variable in the pupil plane. The error in the sine wave is computed by taking its derivative as a function of spatial frequency. The derivative is:

$$A(f)\ \cos(2\pi \boldsymbol{u} f)\ 2\pi \boldsymbol{u} \tag{3.20}$$

for a cosine wave the maximum value is 1 and the minimum value is 0. For optimum interference the cosine aberration will return a signal of 1 which allows us to write equation 3.20 as:

$$A(f)\ 2\pi\ \boldsymbol{u}\ f \tag{3.21}$$

we can replace $\boldsymbol{u}$ with D for a cosine wave crossing an aperture D.

$$A(f)\ 2\pi\ D\ f \tag{3.22}$$

it takes a wave of spatial frequency f, traveling at velocity v, an amount of time t_c to move across an aperture D.

$$A(f)\ 2\pi\ vt_c\ f, \tag{3.23}$$

If we say that the integration time t_{int} equals the time t_c it takes for a cosine wave to cross the pupil then $t = t_{int} = t_c$. The total error added in quadrature can be written as follows [11]:

$$\sigma = \sqrt{(2\pi\ A(f)\ v\ t\ f)^2 + \Big(\frac{\lambda}{2\pi}\Big)^2 \Big(\frac{\beta}{\sqrt{tF\pi D^2}}\Big)^2} \tag{3.24}$$

the $(\frac{\lambda}{2\pi})^2$ in front of the photon noise error is included to convert from radians squared to meters

squared. In order to determine the time lag for which the total error given in Eq. 3.24 is a minimum we differentiate Eq. 3.24 with respect to time. Setting the derivative to zero will give us the minimum error.

$$\dot{\sigma} = \left[(2\pi\ A(f)\ v\ t\ f)^2 + \Big(\frac{\lambda}{2\pi}\Big)^2\Big(\frac{\beta}{\sqrt{tF\pi D^2}}\Big)^2\right]^{-1/2} 4\pi^2\ A(f)^2\ v^2\ t\ f^2 = 0 \tag{3.25}$$

Eq. 3.25 can be simplified to:

$$\dot{\sigma} = (2\pi\ A(f)\ v\ t\ f)^2 + \Big(\frac{\lambda_0}{2\pi}\Big)^2\Big(\frac{\beta^2}{tF\pi D^2}\Big) = 0 \tag{3.26}$$

solving Eq. 3.26 gives us the time lag for which the error is a minimum [11].

$$t^3 = \Big(\frac{\lambda}{2\pi}\Big)^2\Big(\frac{\beta^2}{F\pi D^2}\Big)\Big(\frac{1}{(2\pi\ A(f)\ v\ f)^2}\Big) \tag{3.27}$$

we substitute $A(f)_{OPD}$ from Eq. 3.11 into Eq. 3.27.

$$t^3 = \Big(\frac{\lambda}{2\pi}\Big)^2\ \Big(\frac{1}{2\pi v f}\Big)^2\ \frac{\beta^2\ f^{11/3}\ D^2\ r_0^{5/3}}{0.0484\ F\ \pi\ D^2\lambda_0^2\ X(f,\lambda_i)} \tag{3.28}$$

$$t = 0.1616\Big(\frac{\lambda}{\lambda_0}\Big)^{2/3}\frac{\beta^{2/3}\ f^{5/9}\ r_0^{5/9}}{F^{1/3}\ v^{2/3}\ X^{1/3}\ (f,\lambda_i)} \tag{3.29}$$

t as given by Eq. 3.29 is the time lag that gives minimum error if the only errors considered are photon noise and error due to time lag between wavefront sensing plus correction and the rate of change of the atmosphere. The corresponding residual error (assuming a perfect deformable mirror and a noiseless detector) is obtained by substituting t into Eq. 3.24.

$$\sigma_{res} = \sqrt{\frac{0.2268\ \lambda^{4/3}\ \lambda_0^{2/3}\ \beta^{4/3}\ v^{2/3}\ X(f,\lambda_i)^{1/3}}{F^{2/3}\ D^2\ f^{5/9}\ r_0^{5/9}} + \frac{0.1567\ \lambda^{4/3}\ \lambda_0^{2/3}\ \beta^{4/3}\ v^{2/3}\ X(\kappa,\lambda_i)^{1/3}}{F^{2/3}\ D^2\ f^{5/9}\ r_0^{5/9}}} \tag{3.30}$$

the residual error or the minimum amplitude of the aberrated wavefront can then be written as:

$$\sigma_{res} = h = \sqrt{0.3835 \frac{\lambda^{4/3}\ \lambda_0^{2/3}\ \beta^{4/3}\ v^{2/3}\ X(f,\lambda_i)^{1/3}}{F^{2/3}\ D^2\ f^{5/9}\ r_0^{5/9}}} \tag{3.31}$$

The off-axis PSF gives the off-axis intensity distribution:

$$I(\alpha) = \left(\frac{\pi h}{\lambda_i}\right)^2 [PSF(\alpha + \mathbf{f}\lambda) + PSF(\alpha - \mathbf{f}\lambda)] \tag{3.32}$$

$$I(\alpha) = \left(\frac{\pi}{\lambda_i}\right)^2 \left[0.3835\ \frac{\lambda_i^{5/9}\lambda^{4/3}\ \lambda_0^{2/3}\ \beta^{4/3}\ v^{2/3}\ X(\alpha/\lambda_i,\lambda_i)^{1/3}}{F^{2/3}\ D^2\ r_0^{5/9}\ \alpha^{5/9}}\right] \tag{3.33}$$

where h is the amplitude of the aberrated wavefront across the aperture and the substitution $f = \alpha/\lambda$ is made in Eq. 3.31. The residual error produces a symmetric pair of speckles [27] from which the contrast is derived. The contrast between the central, ideal PSF and a point α angle away is [11]:

$$C(\alpha) = 3.785\ \frac{\lambda^{4/3}\ \lambda_0^{2/3}\ \beta^{4/3}\ v^{2/3}\ X(\alpha/\lambda_i,\lambda_i)^{1/3}}{\lambda_i^{13/9}\ F^{2/3}\ D^2\ r_0^{5/9}\ \alpha^{5/9}} \tag{3.34}$$

where λ_0 is the wavelength at which r_0 is measured, λ_i is the wavelength at which the final image is obtained, and λ is the wavefront sensing wavelength.

3.5. Contrast: Direct comparison between the nlCWFS and the SHWFS

The atmosphere is dominated by low order aberrations which scatter light at small angular separations where an exoplanet might reside. In order to be able to detect the exoplanet it is necessary to use a wavefront sensor optimized to sensing low order modes. Since the SHWFS divides the pupil light into subapertures it limits interference to occur between points limited to the subaperture thereby loosing sensitivity to low order aberrations that require interference between points much further away. The nlCWFS is sensitive to low and high order aberrations because it allows interference between points that are separated by the pupil diameter D and also allows interference between points with much smaller separation. The PSF obtained with the SHWFS is seeing limited (SHWFS subaperture d is typically the size of r_0) where as the nlCWFS delivers a diffraction

limited PSF. The difference allows the nlCWFS to image a source that is $(D/r_0)^2$ less bright. In background limited situations the nlCWFS has a gain in sensitivity of D^4, D^2 gain due to the diffraction limit of the telescope and D^2 gain due to the telescopes collecting area. Whereas conventional wavefront sensors only benefit from the D^2 gain due to the collecting power. The difference is especially important for extremely large telescopes.

Contrast is computed using Eq. 3.34 and the β values obtained from simulating the nlCWFS and the SHWFS. The other parameters that go into Eq. 3.34 are listed in Table3.3. The contrast obtained for both wavefront sensors when reconstructing spatial frequencies 1 to 16 is listed in Table3.4. The results are promising and show that at low spatial frequencies the nlCWFS can deliver contrasts that are 10 to 16 times higher than those delivered by the SHWFS. According to Eq. 3.35 this difference will allow the nlCWFS to detect an object that is dimmer by about $\Delta m \approx 3$ at the lowest spatial frequency.

$$\Delta m = -2.5 \log_{10} \frac{C_{nlCWFS}}{C_{SHWFS}} \tag{3.35}$$

here m is the apparent magnitude, C_{nlCWFS} is the contrast obtained with the nlCWFS and C_{SHWFS} is the contrast obtained with the SHWFS. Between spatial frequencies of two and eight the difference in contrast obtained between the two wavefront sensors will allow the nlCWFS to detect objects that are dimmer by almost one or two magnitudes.

Table 3.3: Contrast Parameters

Parameter	Symbol	unit	value used
Telescope diameter	D	m	1.5
Detection wavelength	λ_i	m	3.18×10^{-6}
WFS wavelength	λ	m	790×10^{-9}
Seeing wavelength	λ_0	m	790×10^{-9}
Fried parameter	r_0	m	0.12
Wind speed	v	m s^{-1}	12.5
Source brightness	F	ph s^{-1} m^{-2}	3.89×10^7, m $= 10$
Angular separation	α	rad	$\lambda/D = 0.1''$

Table 3.4: Contrast Comparison between the nlCWFS & the SHWFS

Spatial Frequency		β	Contrast
1	nlCWFS	3.31	1.00×10^{-4}
	SHWFS	26.37	1.60×10^{-3}
2	nlCWFS	2.67	7.50×10^{-5}
	SHWFS	13.08	6.00×10^{-4}
3	nlCWFS	2.56	7.10×10^{-5}
	SHWFS	8.51	4.00×10^{-4}
4	nlCWFS	2.46	6.71×10^{-5}
	SHWFS	6.40	2.00×10^{-4}
5	nlCWFS	2.42	6.58×10^{-5}
	SHWFS	5.15	2.00×10^{-4}
6	nlCWFS	2.37	6.38×10^{-5}
	SHWFS	4.37	1.00×10^{-4}
7	nlCWFS	2.32	6.23×10^{-5}
	SHWFS	3.82	1.00×10^{-4}
8	nlCWFS	2.30	6.13×10^{-5}
	SHWFS	3.43	1.00×10^{-4}
9	nlCWFS	2.30	6.13×10^{-5}
	SHWFS	3.11	1.00×10^{-4}
10	nlCWFS	2.29	6.12×10^{-5}
	SHWFS	2.88	1.00×10^{-4}
11	nlCWFS	2.23	5.89×10^{-5}
	SHWFS	2.67	1.00×10^{-4}
12	nlCWFS	2.12	5.51×10^{-5}
	SHWFS	21.25	1.00×10^{-4}
13	nlCWFS	2.04	5.23×10^{-5}
	SHWFS	2.50	1.00×10^{-4}
14	nlCWFS	2.00	5.09×10^{-5}
	SHWFS	2.37	1.00×10^{-4}
15	nlCWFS	1.99	5.08×10^{-5}
	SHWFS	2.29	1.00×10^{-4}
16	nlCWFS	2.00	5.12×10^{-5}
	SHWFS	2.31	1.00×10^{-4}

4. CHAPTER FOUR

"The true method of knowledge is experiment."

- William Blake

4.1. Laboratory Demonstration

In this chapter I explore how well the nlCWFS is able to sense an aberrated wavefront generated in the laboratory, compared to the SHWFS. I am interested in seeing how well the nlCWFS is able to reconstruct the wavefront. Since the nlCWFS is designed to work over the visible spectrum a polychromatic design to allow for chromatic compensation is developed.

4.1.1. Sensing Defocus

The goal is to introduce a simple aberration such as defocus and record how well the nlCWFS is able to sense the aberration. The SHWFS serves as the truth measurement. A laboratory experiment is set up to measure a wavefront error with both the nlCWFS and the SHWFS. The experimental layout is shown in Figure 4.1. A 635 nm He-Ne laser source of constant and uniform brightness is used. A collimated beam passes through the pupil which is common to both the SHWFS leg and the nlCWFS leg. Beyond the pupil, light is split to the two legs by the use of a 50-50 beamsplitter. Both the nlCWFS and the SHWFS legs have afocal relays that re-size the collimated beam and relay the pupil. The lenses used for the two afocal relays are different and are chosen in accordance with the available space in each path and the beam footprint required on the lenslet array for the SHWFS, and the detector for the nlCWFS. The SHWFS lenslet array has a pitch $= 96\,\mu$m, and a focal length $= 1400\,\mu$m. The pupil size at the SH lenslet array is 1 mm and illuminates about ten subapertures across the pupil. The SHWFS detector has $6\,\mu$m pixels. A sample image taken with the SHWFS is show in Figure 4.2. For the nlCWFS the detector pixel size is $16\,\mu$m and the size of the relayed pupil is 0.5 mm.

Defocus is the single aberration introduced by moving the collimating lens which is common to both arms. The nlCWFS camera is mounted on a motorized linear stage which translates the camera to the pupil and to conjugate Fresnel planes on either side of the pupil. An image taken at the pupil, and a sample of images taken at different Fresnel planes are show in Figure 4.3. The wavefront is recorded at several Fresnel plane distances on either side of the re-imaged pupil and at the pupil plane. The nlCWFS reconstruction algorithm only needs the wavefront recorded in a few Fresnel planes however 25 planes are used in this experiment to allow the reconstructor flexibility. A Gerchberg-Saxton based iterative algorithm is used to carry out the non-linear wavefront reconstruction. The reconstructed wavefront is decomposed into Zernike modes to determine the contribution defocus has on the wavefront. The SH wavefront reconstruction algorithm measures wavefront slopes and converts them into a wavefront map. The algorithm uses a mathematical model to determine how each Zernike [40] influences the SH spot to shift within the subaperture. The effect of the Zernike on the spot shift is known as the influence function. The influence function is inverted to obtain the reconstruction matrix, which allows one to relate spot motion or wavefront slope to a summation of Zernikes or wavefront aberration. I measure the RMS wavefront error, due to defocus, using the nlCWFS and the SHWFS and compare the two results. Table 4.2.1 lists the experimental parameters for both wavefront sensors. The RMS wavefront error obtained with the nlCWFS is 14.94 radian and the RMS wavefront obtained with the SHWFS is 13.58 radian. The rms wavefront error obtained with the two wavefront sensors agree within $10\,\%$. This establishes that the nlCWFS can both sense and reconstruct an aberration introduced in the laboratory as well as the established, and widely used, SHWFS.

Table 1: Comparison between nlCWFS & SHWFS

Wavefront sensor	nlCWFS	SHWFS
Defocus	$0.03\,\mu$m	$0.03\,\mu$m
camera pixel size	$16\,\mu$m	$6\,\mu$m
pupil size at CCD	$0.5\,$mm	$1\,$mm
subapertures	-	80
no. of Fresnel planes used	25	-
Fresnel plane spacing	$0.003\,\mu$m	-
RMS wavefront error	$14.94\,$rad	$13.58\,$rad

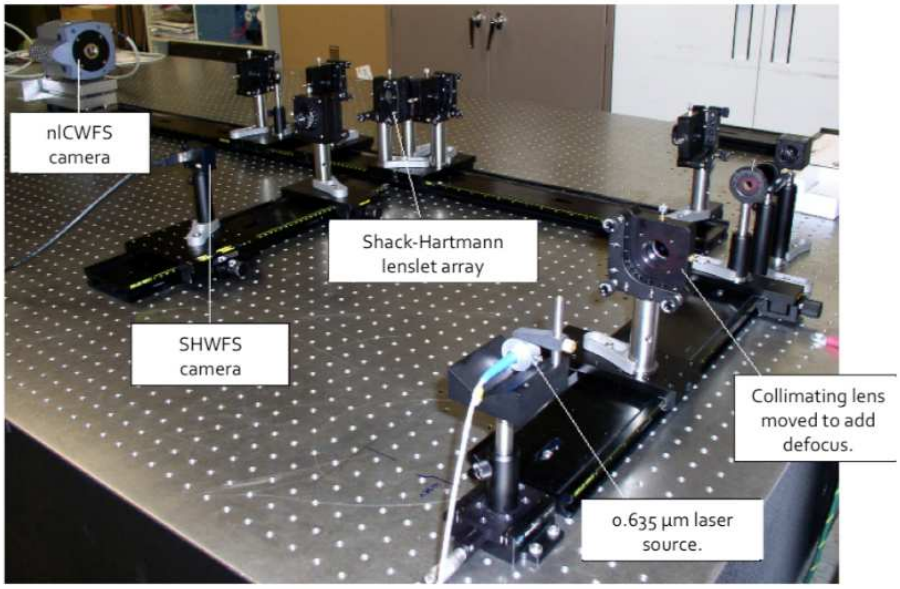

Figure 4.1: Laboratory experimental setup to compare the nlCWFS with the SHWFS. Both legs of the experiment are shown.

4.1.2. Reconstructing a turbulent wavefront with the nlCWFS

After establishing that the nlCWFS is able to accurately sense and reconstruct a Zernike mode, I want to introduce it to an aberrated wavefront prescribed with the Kolmogorov [22] spectrum. The experimental set-up is the same as shown in Figure 4.1 except, this time, only the nlCWFS path is

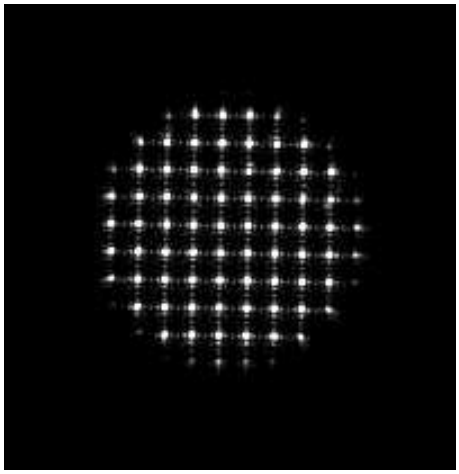

Figure 4.2: A sample image taken with the SHWFS. The image is taken using a laser of $\lambda = 0.635\,\mu$m. The SH lenslet array has a pitch of $96\,\mu$m and a focal length of $1400\,\mu$m. With a $1\,$mm pupil diameter about ten Shack-Hartmann subapertures across the pupil are illuminated.

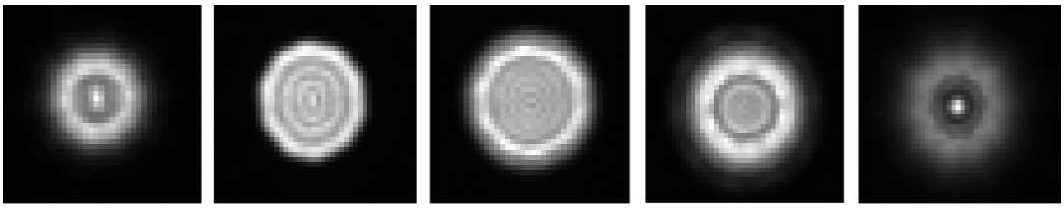

Figure 4.3: A sample of images taken with the nlCWFS are shown. The central image is taken at the pupil. The images on either side of the pupil are taken at a sampling of a few different Fresnel planes.

used. A point source is produced by a He-Ne 635 nm laser which is propagated to a collimating lens. The collimated beam emerging from the lens is masked by an aperture, that serves as the pupil. The masked beam is passed through an afocal relay which re-sizes the beam diameter and relays the pupil onto the detector. A phase screen consisting of two near index matched materials, machined with a phase profile described by Kolmogorov statistics [31] is used to create an atmospheric-like turbulence. The phase screen is placed as close to the pupil as is possible. The phase screen distorts the pristine beam produced by the laser, before it reaches the nlCWFS detector. As described above the nlCWFS is mounted on a translation stage which is, remotely controlled and translated to Fresnel planes on either side of the re-imaged pupil plane. Images recorded in 19 Fresnel planes are shown in Figure 4.4. There is a separation of 0.0317263 m between each Fresnel plane.

The objective of the experiment is to use the nlCWFS detector to sense the aberrated wavefront and determine how well the nlCWFS reconstruction algorithm is able to reconstruct the field in each of the Fresnel planes. The end goal is to be able to reconstruct the phase in the pupil. Images recorded in the 19 Fresnel planes are fed to the Gerchberg-Saxton (GS) [8] reconstruction algorithm so that the wavefront propagation can be carried out. From looking at the measured intensities it seems that the pupil plane is at Fresnel plane 13. In the pupil plane instead of seeing a smooth intensity field, structure is seen because the turbulence phase screens were place in front of the physical pupil and were not placed in the pupil. The pupil plane phase shown in Figure 4.5 is reconstructed using the GS reconstruction algorithm. Since the laboratory data is not as pristine as the idealistic simulated field, the GS code written for a simulated field is considerably modified to adapt it to laboratory data. For instance the amplitude constraints previously applied at the pupil plane are no longer valid for laboratory data since the laboratory pupil field is not a smooth intensity field. This is a result of hardware limitations which caused me to place the phase screens in front of the pupil instead of in the pupil. Another modification uses a larger number of Fresnel planes (19) in order to provide sufficient phase information to the reconstruction algorithm. The laboratory acquired fields have the camera output format and not the ".mat" format of fields simulated using Matlab therefore the data input structure is changed. In addition to this the laboratory

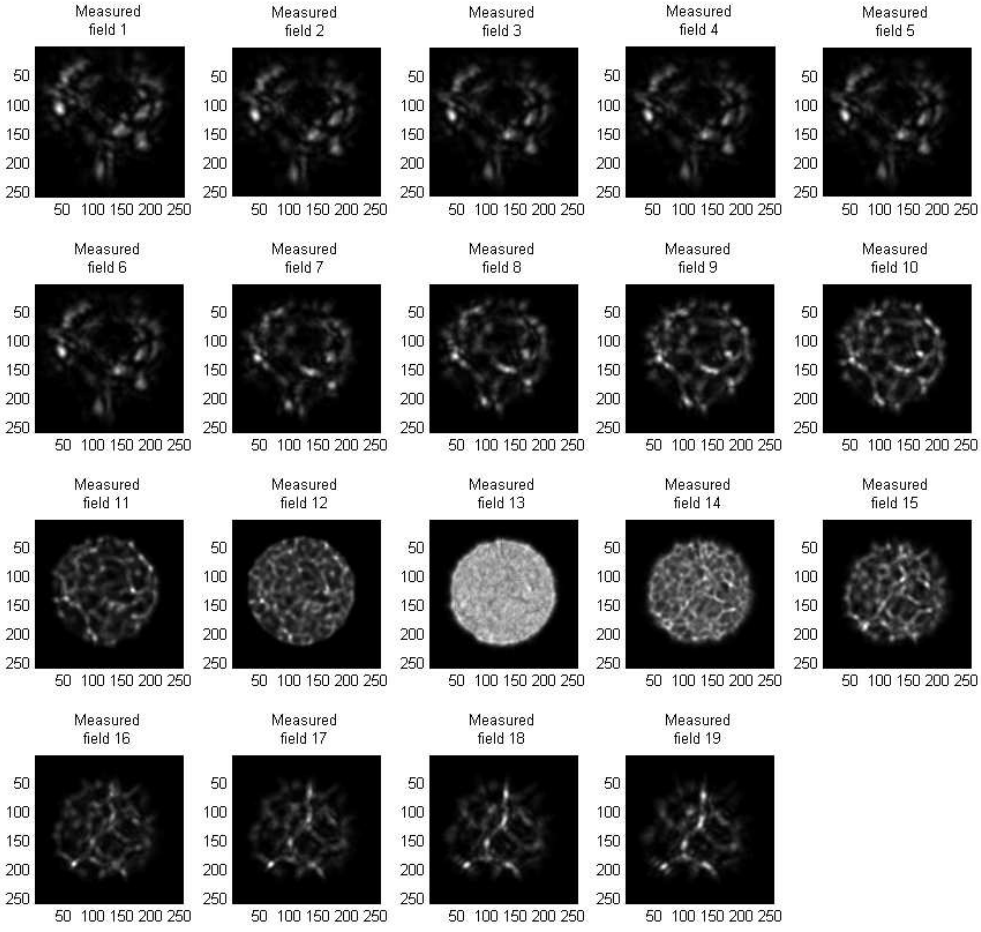

Figure 4.4: Intensity recorded in 19 Fresnel planes by the nlCWFS detector. The pupil plane lies close to Fresnel plane 13.

data has to be prepared before it can be fed to the GS algorithm. A "dark" image is subtracted from all the recorded images. All the intensity fields are centered and a mask is applied to each of the images to suppress noise propagation. A 256×256 pixel circular mask is applied to fields 1 through 12. A 180×180 pixel circular mask is applied to fields $13 - 16$. No mask is applied to the remaining three fields $17 - 19$. A smoothing function is applied to each of the complex fields to suppress aliasing. The smoothing function is determined empirically, fields 1 through 11 and fields $17, 18$, and 19 are smoothed using a 13 pixel wide Gaussian function. The remaining fields are smoothed using a 5 pixel wide Gaussian function.

As there is no truth measurement of the pupil plane phase, reconstructed fields in each of the Fresnel planes are compared to the measured intensities to validate the reconstruction. Intensity fields for four of the Fresnel planes, measured and reconstructed, are shown in Figure 4.6. From looking at the measured and reconstructed images one can see that the agreement is very good.

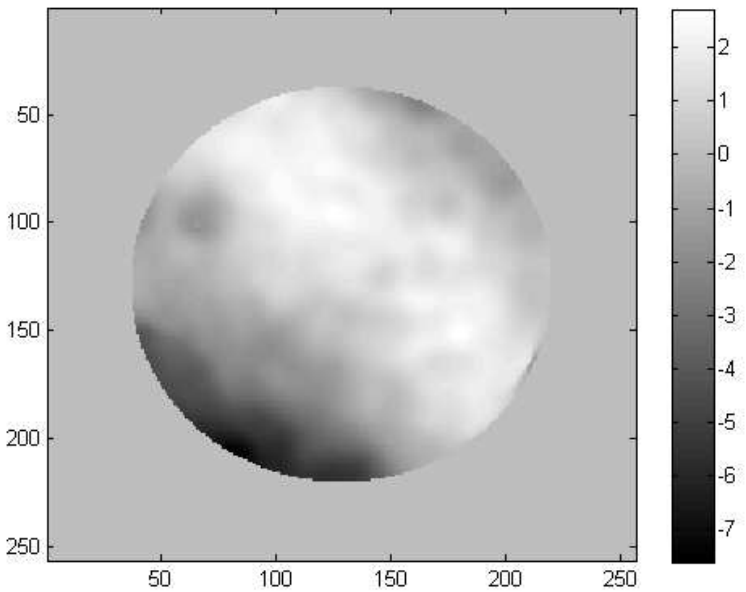

Figure 4.5: Gerchberg-Saxton reconstructed pupil phase.

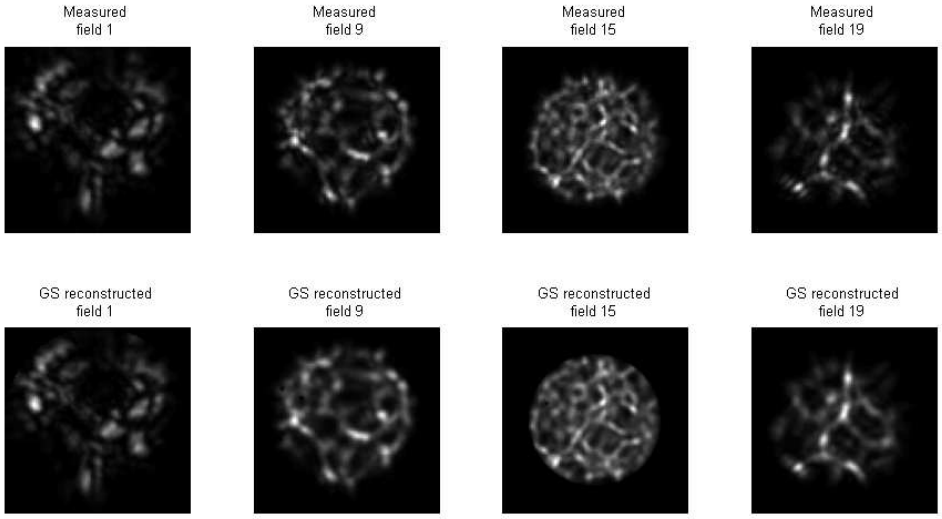

Figure 4.6: The top row shows the intensity fields measured in four Fresnel planes. The bottom row shows the Gerchberg-Saxton reconstruction of the fields in the four Fresnel planes.

4.2. Chromatic Compensation

4.2.1. Polychromatic Design

The nlCWFS relies on diffraction-limited speckles in the Fresnel propagated plane images to achieve its sensitivity. However if you have a polychromatic source axial chromatic and lateral chromatic aberrations will cause the speckles to blur. Figure 4.7 illustrates longitudinal chromatic aberration resulting when two wavelengths are present. Longitudinal chromatic aberration will cause the speckles to blur, however this can be easily corrected with the use of achromats. The problem we face in designing the nlCWFS is not just limited to wavelength dependent defocus and magnification, in addition, the nlCWFS needs to access speckled images in different Fresnel propagated planes where the Fresnel propagation distance is wavelength dependent,

$$z = \frac{1}{2|f|^2\lambda} \tag{4.1}$$

In Eq. 4.1 z is the Fresnel propagation distance, f is spatial frequency, and λ is the observation wavelength; z and f are related to λ for a fixed Fresnel number. The goal is to have a fixed Fresnel

number across a spectral band, on a detector, see Figure 4.8. We do not want wavelength dependent blurring in the imaged Fresnel planes. The polychromatic design of the optics is complex because the intent is not to correct chromatic aberration but instead introduce a prescribed amount of wavelength and spatial frequency dependent chromatic defocus.

For each Fresnel plane used in the reconstruction algorithm a unique combination of chromatic re-imaging optics (CRO) is required. It has been determined, from simulations, that it is possible to reconstruct the wavefront if speckled images are measured in four Fresnel planes. As a result four unique CRO systems need to be designed. The Fresnel propagation distances used in the design of the CRO are obtained from parameters set in the initial simulations carried out by Guyon [13]. These are the Fresnel propagation distances z_{sim} that awarded successful wavefront reconstruction. The simulated z_{sim} distances are for a pupil diameter = $8\,$m and $\lambda = 850\,$nm. The equivalent distances z_{lab} are found for the lab where the pupil diameter = $1\,$mm, and range of wavelengths spans, $490\,$nm, $590\,$nm, and $660\,$nm. The conversions are shown in Table 1. The pupil diameter is constrained by the size of the detector on which the four Fresnel planes are to be simultaneously imaged. The ratio of the simulated and lab Fresnel propagation distances z_{sim} and z_{lab} are related to the simulated and lab wavelengths λ and pupil diameters D through Eq. 4.2:

$$z_{lab} = \frac{\lambda_{sim}}{\lambda_{lab}} \left[\frac{D_{lab}}{D_{sim}} \right]^2 z_{sim} \tag{4.2}$$

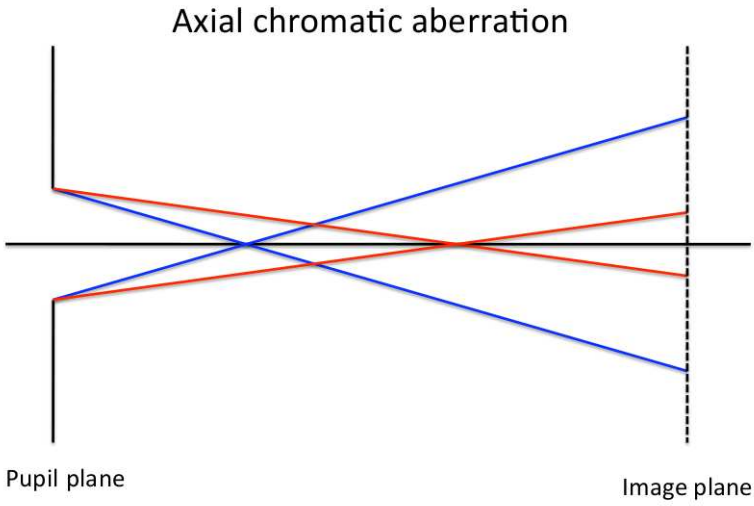

Figure 4.7: For a polychromatic source different wavelengths come to focus at different distances along the optical axis. This wavelength dependent defocus is called axial chromatic aberration where shorter wavelengths focus closer than longer wavelengths. Wavelength dependent magnification in the image plane causes the blue image to be larger than the red image.

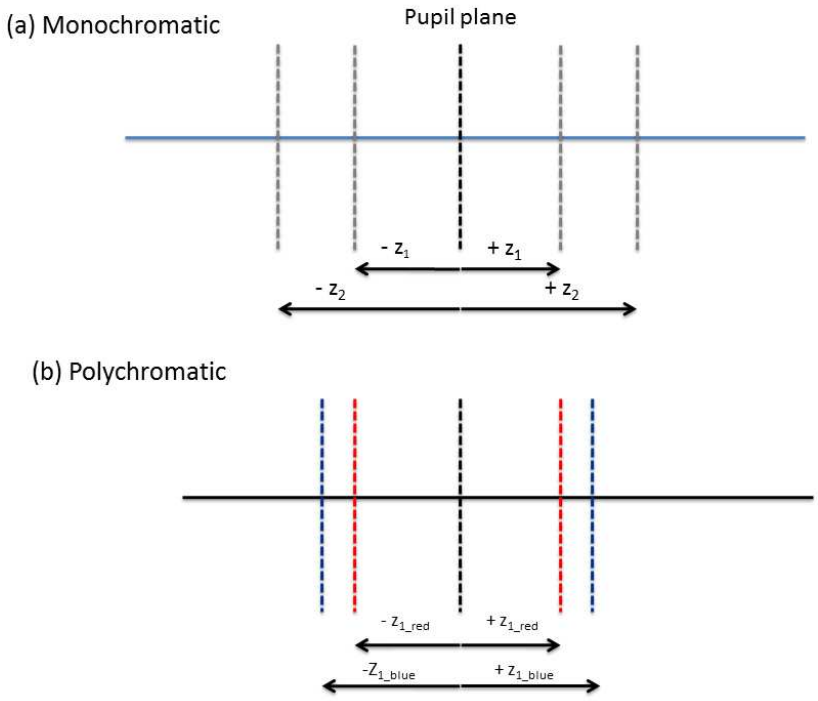

Figure 4.8: (a) shows the pupil plane and Fresnel propagated distances z_1 and z_2 on either side of the pupil plane. Each distance z has a particular spatial frequency associated with it. 4.8 (b) shows how z_1 changes with wavelength. Fresnel propagated distances z_{1-blue} and z_{1-red} correspond to a single spatial frequency but are sensed at a different wavelengths. The red and the blue planes have a common Fresnel number.

Table 1: Conversion from simulated parameters to lab parameters

Simulation: $D = 8\,\text{m}$ $\lambda = 850\,\text{nm}$, $z = 3500\,\text{km}$	
Lab: $D = 1\,\text{mm}$ λ (nm)	z (m)
490	0.0949
590	0.0788
660	0.0704
Simulation: $D = 8\,\text{m}$ $\lambda = 850\,\text{nm}$, $z = 2500\,\text{km}$	
Lab: $D = 1\,\text{mm}$ λ (nm)	z (m)
490	0.0678
590	0.0563
660	0.0530

An afocal relay is used to relay the pupil to the detector plane. The relay demagnifies the pupil so that it has a $1\,\text{mm}$ footprint on the detector. The afocal relay is shown in Figure 4.9, where ϕ_1 and ϕ_2 denote the power of lens 1 and lens 2, respectively. The location of lens 2 and the detector plane are fixed. The detector plane is conjugated to the propagated pupil plane or the Fresnel plane. With monochromatic light the Fresnel plane is easily relayed to a conjugate location. However with polychromatic light the Fresnel plane location becomes wavelength dependent and there is a different conjugate location for each wavelength. In order to re-image the wavelength dependent planes onto a common detector we introduce the CRO with power ϕ_{CRO} , see Figure 4.10. The CRO will eventually consists of several refractive elements however we start by treating it as a single element and determine the power needed to bring a defocus of δf to form an image in the detector plane. Gaussian reduction is used to determine ϕ_{CRO}. In Figure 4.10 the distance from lens 2 to the detector plane is d_d. The combined power of lens 1 and CRO is obtained by performing a Gaussian reduction and is denoted by ϕ_{1-CRO}. The distance d_d is related to, the power of lens 1, the combined power of lens 1 and the CRO, and to the spacing t_1 between lens 1 and the CRO by:

$$d_d = \frac{\phi_{CRO}}{\phi_{1-CRO}} t_1 \tag{4.3}$$

the formula for Gaussian reduction is:

$$\phi_{1-CRO} = \phi_1 + \phi_{CRO} - \phi_1 \phi_{CRO} \tag{4.4}$$

the distance f_f from the principal plane P, defined for lens 1 and the CRO, is called the front focal length. The front focal distance FFD is equal to:

$$FFD = f_f + d_d \tag{4.5}$$

substituting for f_f and d_d we obtain:

$$FFD = \frac{-1}{\phi_{1-CRO}} - \frac{\phi_{CRO}}{\phi_{1-CRO}} t_1 \tag{4.6}$$

For each respective wavelength we substitute FFD with FFD$-\delta$f to account for the shifted plane, see Figure 4.10, and use the definition $\phi_1 = \frac{1}{f_1}$. We plug in Eq. 4.3 and Eq. 4.4 into Eq. 4.6 and solve for ϕ_{CRO} to obtain the power for the chromatic re-imaging optic.

$$\phi_{CRO} = \frac{\frac{-1}{f_1 - \delta f} - \phi_1}{\frac{1 - \phi_1 t_1 - t_1}{f_1 - \delta_f}} \tag{4.7}$$

Table 2 lists the required power of the CRO that will bring a pupil defocus of δf to form an image on the detector.

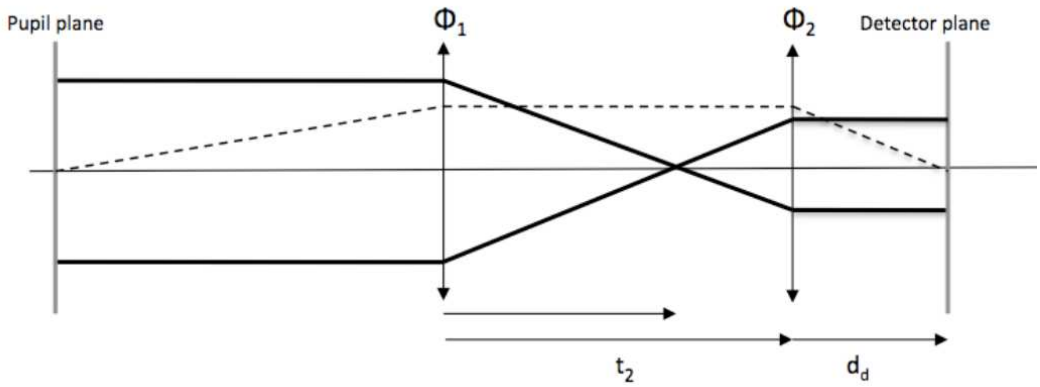

Figure 4.9: An afocal relay containing lens 1 and lens 2 with power ϕ_1 and ϕ_2, respectively is used to re-image the pupil on to the detector. The solid lines going from the pupil to image plane trace the marginal rays and the dotted line traces the chief ray.

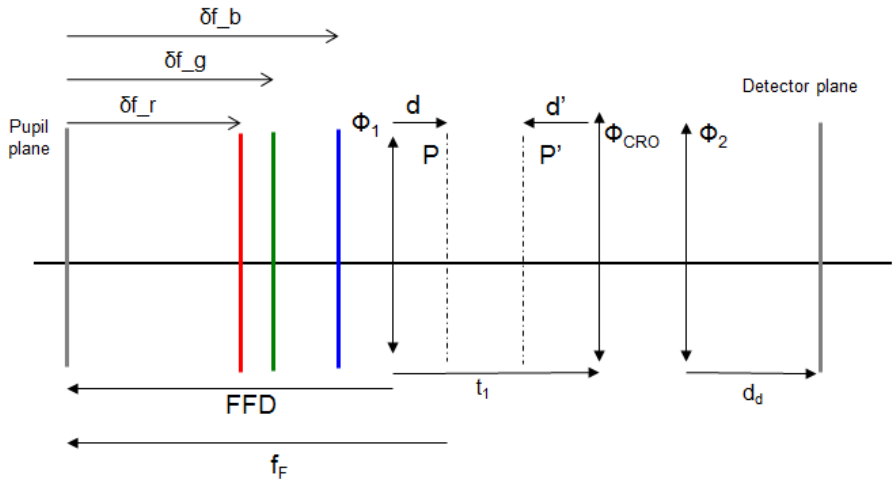

Figure 4.10: The detector plane is fixed and is common to all wavelength dependent pupils. The defocus δf_r shows the shift in the pupil plane due to the red wavelength, δf_g shows the shift in the pupil plane due to the green wavelength, δf_b shows the shift in the pupil due to the blue wavelength. The introduction of the chromatic re-imaging optics (CRO) allows the red, green, and blue pupil to be imaged in a common image plane called the detector plane. The combined power of the chromatic re-imaging optics is ϕ_{CRO}.

Table 2: Power of the chromatic re-imaging optics (CRO) for given Fresnel propagation distance and wavelength.

Conjugated to	λ μm	δf mm	f_{CRO} mm	ϕ_{CRO} mm^{-1}
3500 km at 850 nm with 8 m pupil	490	94.89	1686.16	0.00059
	590	78.81	2030.20	0.00049
	660	70.45	2271.11	0.00044
2500 km at 850 nm with 8 m pupil	490	67.76	2361.28	0.00042
	590	56.28	2842.93	0.00035
	660	50.31	3180.28	0.00031

Professor José Sasián has designed a CRO for one of the four Fresnel paths, specifically the one corresponding to $z_{sim} = +3500$ km. The strong chromatism that needs to be introduced requires an eight-element design, the detail of the lenses is shown in Figure 4.11. I mounted the eight lenses with the prescribed spacing into the lens barrel shown in Figure 4.12. Figure 4.13 illustrates how the CRO prescribes the wavelength dependent defocus. The red line shows the wavelength dependent shift of the imaged pupil. The strong beam compression from the telescope primary mirror (6 to 10 m) to the camera (≈ 1 mm) requires these optics to be designed for a large field-of-view ($> 1^o$). A Zemax ray trace was carried out to ensure that the introduced chromatic aberration remains valid over field-of-views ranging from $0 - 2.2$ degrees.

4.2.2. Laboratory Integration of the CRO

Once the CRO is built with the specified optics and prescribed effective power, its correct integration into the nlCWFS optical path is important in order to obtain the desired chromatic aberration. Figure 4.14 shows the placement of the CRO with respect to the pupil. The conjugate pupil plane shown is the relayed pupil, when achromats are used. The red, green, and blue lines following the pupil are the respective wavelength dependent Fresnel plane locations. The CRO is sandwiched between the afocal system formed by lens L1 and lens L2. According to Eq. 4.1 the propagation

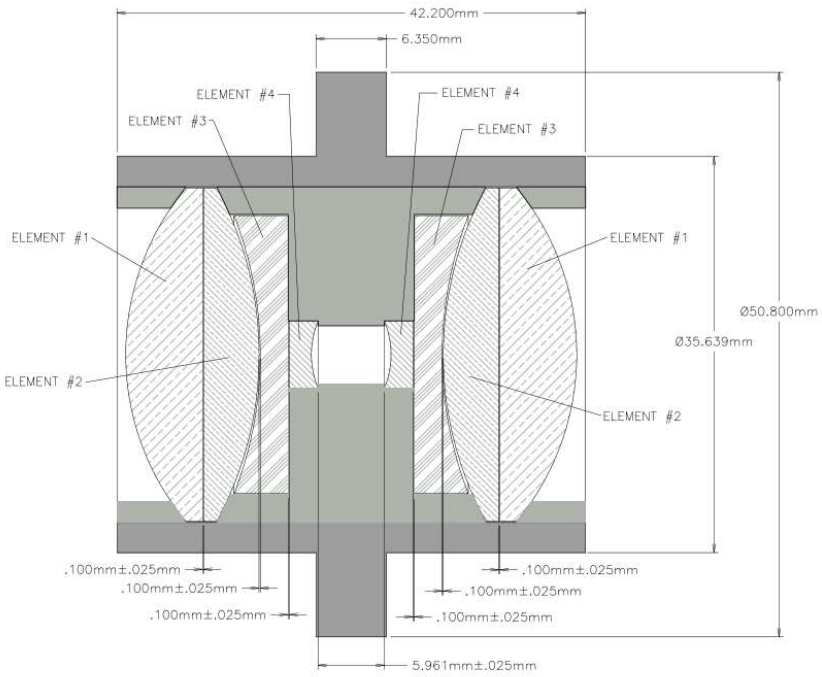

Figure 4.11: The chromatic re-imaging optics (CRO) consists of an eight element assembly. The design shown in this figure is for one of the four channels of the nlCWFS.

Figure 4.12: The eight element chromatic re-imaging optics (CRO) mounted in a lens barrel.

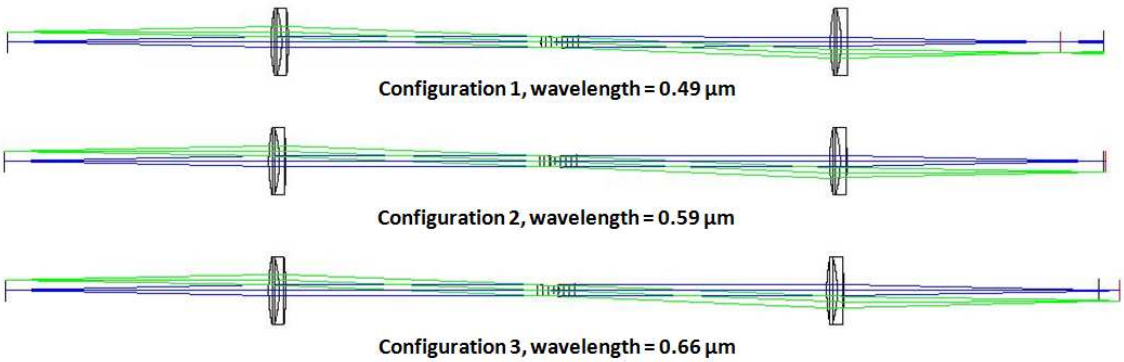

Figure 4.13: The design shows a one-to-one afocal relay with the chromatic re-imaging optics (CRO) inserted in between the relay lenses. The three designs show how the CRO shifts each re-imaged pupil location depending on the wavelength. The vertical, red line in front of the relay represents the re-imaged pupil.

distance z must be chosen to be inversely proportional to the wavelength λ. Figure 4.14 shows how the red pupil is formed at a distance z_{660} from L1. Here the subscript 660 represents the observational wavelength $\lambda = 660\,\text{nm}$. Similarly the green pupil is formed a distance z_{589} from L1 and the blue pupil is formed a distance z_{490} from L1. In order to image sharp speckles the red, green, and blue planes need to overlap in the detector plane. The chromatic re-imaging optics (CRO) are designed to compensate for these wavelength dependent shifts so that the red, green and blue planes are all imaged simultaneously onto the detector without any wavelength dependent magnification. The CRO introduces a prescribed amount of wavelength dependent defocus that allows for the propagated plane to remain sharp in the detector plane over the entire visible band. The integration of the single designed CRO is discussed below.

The designed CRO corresponds to $z_{sim} = 3500\,\text{km}$. Since the Fresnel number is related to the observation wavelength λ, pupil diameter a, and Fresnel propagation distance z by the formula:

$$N_f = \frac{a^2}{\lambda z} \tag{4.8}$$

this Fresnel propagation distance being discussed corresponds to $N_f = 5.4$. The Fresnel numbers associated with the other three propagated distances that have produced successful wavefront reconstruction in simulations are, $N_f = -5.4, \pm 7.5$. The observational wavelengths and pupil diam-

eters associated with N_{f1} are listed in Table 4.1.

Table 4.1: Wavelength and aperture dependent Fresnel Scaling.

N_f	λ (nm)	a (m)	z m
$+5.4$	850	4	3500×10^{3}
$+5.4$	660	0.5×10^{-3}	70.43×10^{-3}
$+5.4$	589	0.5×10^{-3}	78.92×10^{-3}
$+5.4$	490	0.5×10^{-3}	94.86×10^{-3}

The Zemax modeled separation, between the red and the green pupil is $\Delta z_1 = 7.856\,\text{mm}$ and, between the green and the blue pupil is $\Delta z_2 = 15.245\,\text{mm}$. The CRO is designed such that if the relayed pupil is located a distance z_{ref} from the first lens (ϕ_1) of the afocal relay, see Fig. 4.14, then the red, green, and blue planes will be imaged onto a common detector plane with no axial or lateral chromatic aberrations. The correct positioning of the conjugate pupil is critical or else alignment errors will lead to chromatic aberrations. The method to determine z_{ref} the distance of the relayed pupil from Lens 1 is outlined below. Eq. 4.1 relates the Fresnel propagation distance with wavelength and spatial frequency; this formula can be extended to develop a relationship between two different Fresnel propagation planes and wavelengths.

$$\frac{z_1}{z_2} = \frac{f_2^2 \lambda_2}{f_1^2 \lambda_1} \tag{4.9}$$

here λ_1 and λ_2 refer to the two observation wavelengths, z_1 and z_2 refer to the wavelength dependent Fresnel propagation distances. Since we are interested in sensing a common spatial frequency for both wavelengths $f_1 = f_2$. Eq. 4.9 can be rearranged to solve for z_2. Eq. 4.10 is used to determine the wavelength dependent shift from the relayed pupil location. For channel 1 z_{ref} is $172\,\text{mm}$.

$$z_2 + z_{ref} = z_1 + z_{ref} \frac{\lambda_2}{\lambda_1} \tag{4.10}$$

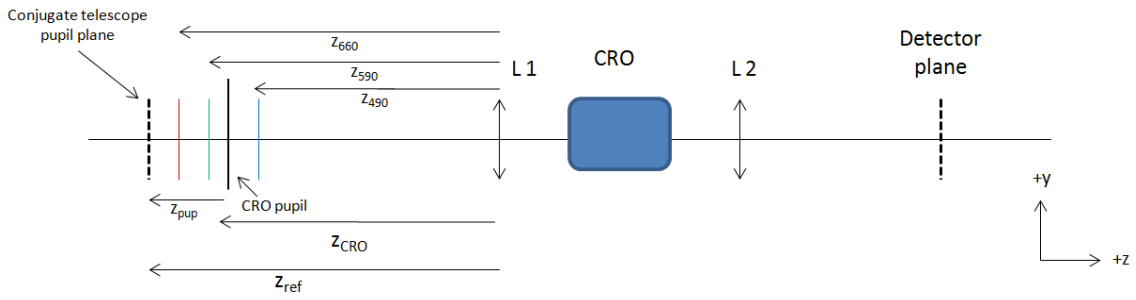

Figure 4.14: Shows the location of the CRO pupil plane and the wavelength dependent shifts in the pupil plane due to Fresnel propagation. The red, green, and blue pupils are shown at a distance z_{660}, z_{589}, and z_{490} respectively from lens 1 (L1). The chromatic re-imaging optics (CRO) is sandwiched between a 1-to-1 afocal relay formed by L1 and lens 2 (L2). By using Eq. 4.10 we calculate z_{ref} the location of the conjugate telescope pupil from L1. The CRO is designed to introduce a prescribed amount of chromaticity so that each wavelength dependent, Fresnel propagated, pupil plane is imaged on to a common detector plain without any axial or lateral chromatic aberrations.

4.2.3. Laboratory Results obtained with the CRO

It is necessary to experimentally verify that the CRO is introducing the designed chromatic aberration. In order to carry out the verification a point source (an LED with a $5\,\mu$m pinhole) is placed 98 mm in front of lens 1 (L1), see Fig. 4.15. The point source is imaged through L2, the CRO, and lens 1 (L1), and is viewed on a white screen placed behind L2. The screen is moved to find the sharpest image location. The CRO is designed to shift the focus as a function of wavelength. When a 625 nm LED is used the sharpest focus is found 113 mm behind L2. For a 530 nm LED source the sharpest focus is found 102 mm behind L2. These wavelength dependent focus locations agree well with the the CRO design specifications and verify CRO design conjugates.

Next I test the wavelength dependent CRO pupil imaging. For this experiment we use a 635 nm laser diode to illuminate an iris placed 172 mm in front of L1. The iris is imaged through L1, the CRO, and L2. A CCD is used to record image frames every 3.9 mm over a distance spanning from 90 mm to 160 mm behind L2. The iris is imaged through the above setup a second time, with the CRO removed. For the iris imaged through the CRO it takes seven frames for a dark Fresnel ring to turn into a bright Fresnel ring and for an iris imaged without the CRO it takes nine image frames for a dark Fresnel ring to turn into a bright Fresnel ring. These results are shown in

Fig. 4.16 and Fig. 4.17 The difference of two image frames corresponds exactly with our design shift of $z_{red} = 7.8$ mm. We carry out a similar test using a 530 nm LED and find that the conversion difference of a dark Fresnel ring to a bright one, between imaging the iris with and with out the CRO, is off-set by the design specification of $z_{blue} = 0.9$ mm. This experiment validates that the CRO performance is in accordance with design specifications.

To test the performance of the CRO we introduce a broad-band source, a white light LED which has a spectral range of 430 nm to 630 nm. The pupil relayed to the detector is measured in the conjugate pupil plane and in several planes on either side of the pupil plane [29, 30]. We compared images recorded in white light, with and with out the CRO inserted, and images obtained using a monochromatic source, a 625 nm laser diode. The monochromatic images are shown in Fig. 4.18. The white light images with no CRO are shown in Fig. 4.19 and the white light images with the CRO are shown in Fig. 4.20. The propagation distances for the images in Figures 4.18, 4.19, and 4.20 are identical. As expected we see the speckles to be very sharp in monochromatic light. In polychromatic light the speckles are slightly blurred but still appear better than expected. When polychromatic light passes through the CRO the speckles blur even further, indicating that we have not achieved the designed chromatic compensation.

In an attempt to understand why white light speckles blur after passing through the CRO; we image the pupil through the CRO at different wavelengths, using a 530 nm LED, a 590 nm LED and a 625 nm LED. We see the pupil location move as a function of wavelength indicating that the CRO is shifting the pupil location as expected. We observe a 20 to $40\,\mu$m change in the pupil size as a function of wavelength. This amount of magnification will affect the sharpness of a $100\,\mu$m speckle however it does not explain the extent of blurring that we see. We need to explore other factors such as miss alignment, diffraction, and dispersion from other optics in the beam path. The phase screens being used to generate turbulence are dispersive and this would alter the chromaticity the CRO introduces. However it needs to be determined whether the phase screens are introducing the level of dispersion being seen.

In conclusion we have built and tested the CRO for one of the four paths of the nlCWFS. I can

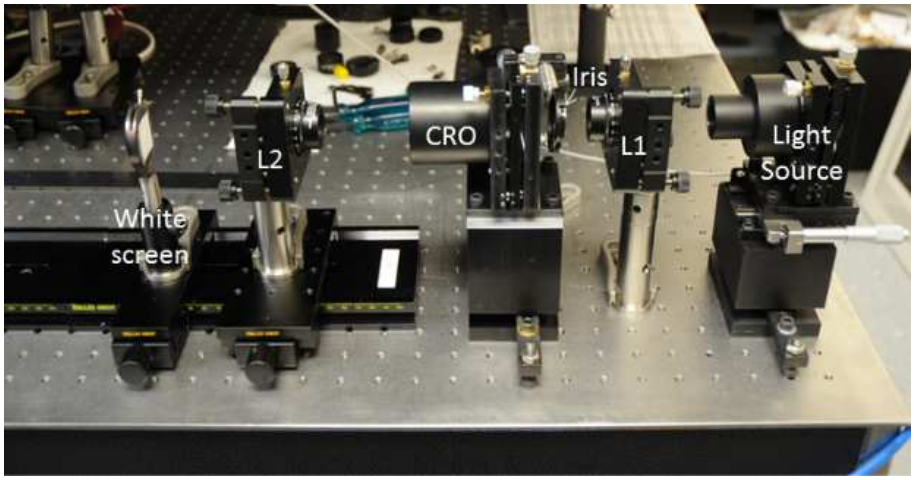

Figure 4.15: Laboratory setup to test that the CRO makes a sharp image of the point source at the correct distance from L2 for a given wavelength. The pinhole mounted in front of the light source serves as the point source. Three wavelengths 530 nm, 590 nm, and 625 nm were tested.

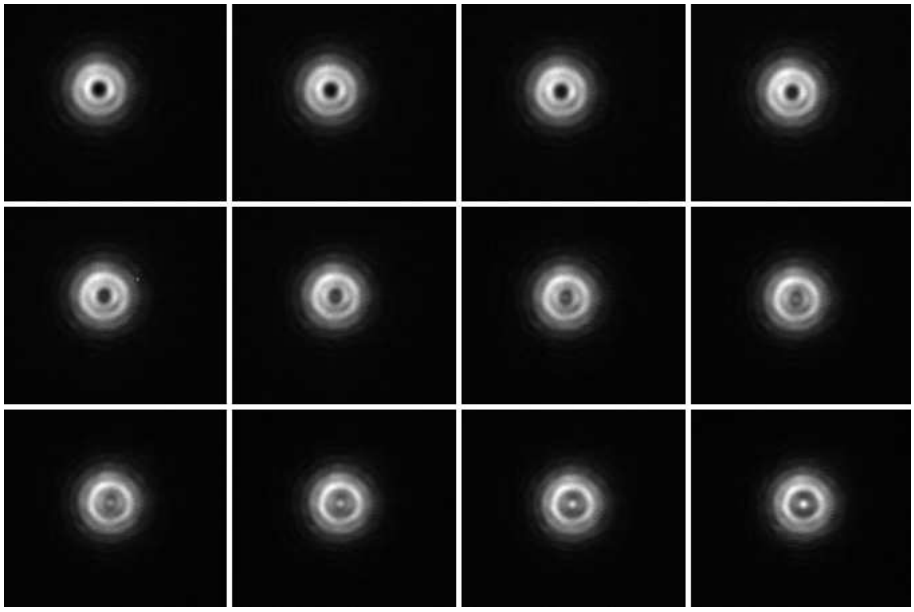

Figure 4.16: Fresnel propagated pupil plane re-imaged through the CRO. The Fresnel propagated pupil is 172 mm in front of L1. It is imaged through L1, the CRO, and L2. The images shown are recorded from a distance of 90 mm to 137 mm behind L2. An image is recorded every 3.9 mm. You can see the dark Fresnel ring turn into a bright Fresnel ring in the seventh image.

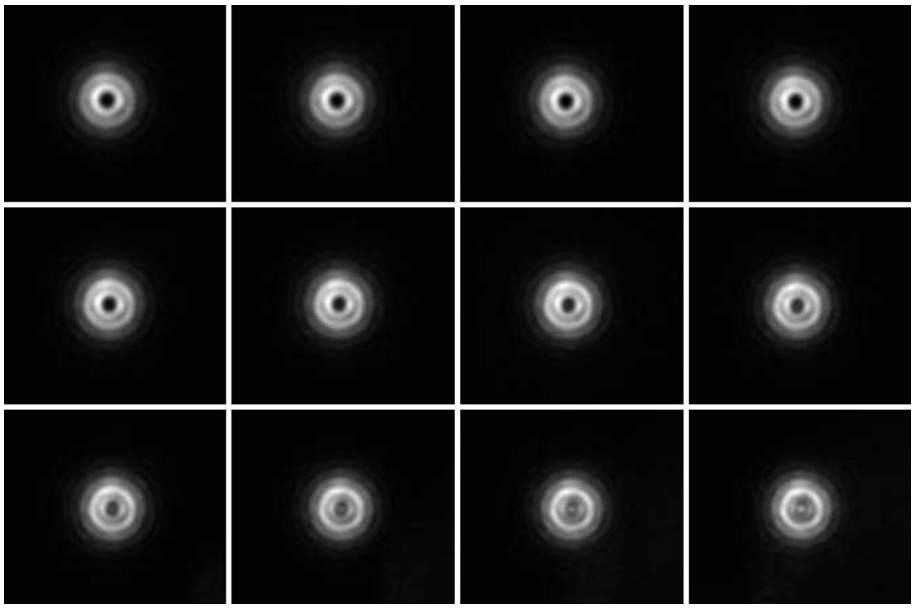

Figure 4.17: Fresnel propagated pupil plane re-imaged with out the CRO. The Fresnel propagated pupil is 172 mm in front of L1. It is imaged through L1, the CRO, and L2. The images shown are recorded from a distance of 90 mm to 137 mm behind L2. An image is recorded every 3.9 mm. You can see the dark Fresnel ring turn into a bright Fresnel ring in the ninth image.

see the expected inverse wavelength dependent pupil shift as we illuminate the CRO with different wavelengths and we do not see significant pupil magnification with wavelength. However when phase screens are used to generate turbulence, the resulting speckles blur as broadband light passes through the CRO. A likely explanation for the chromatic blurring is the dispersion caused by the phase screens. The phase screens used are made of two near-index matched acrylic plates and are coated for 1550 nm. When broadband light passes through the phase screens it suffers from dispersion, the extend of dispersion is unknown. Further investigation in to the source and extent of dispersion was not carried out as the CRO design has been dropped in favor of a design that splits the Fresnel planes in wavelength using dichroics. The optical design using dichroics is detailed in chapter 5.

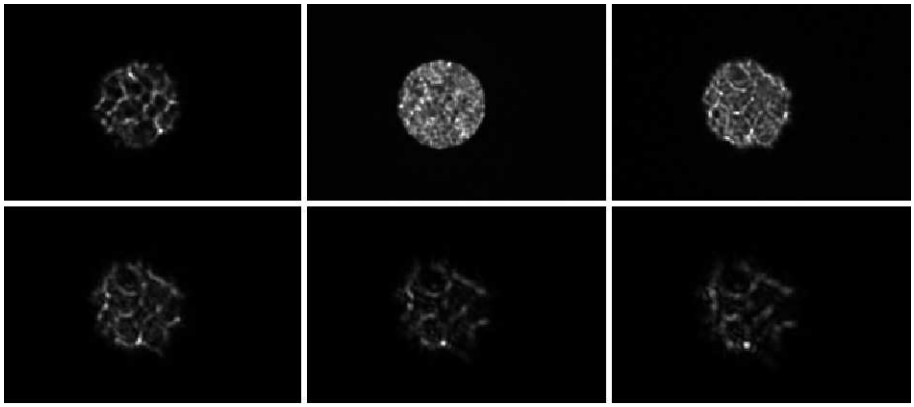

Figure 4.18: Images of the pupil plane propagated through the CRO at $\lambda = 625\,\text{nm}$, A $625\,\text{nm}$ LED is used as the source. The phase plates are placed close to the pupil. The pupil is imaged through the CRO and is relayed to the detector plane, where it is measured. Additional images are recorded in planes on either side of the pupil plane. The speckles are sharp in all the recorded planes.

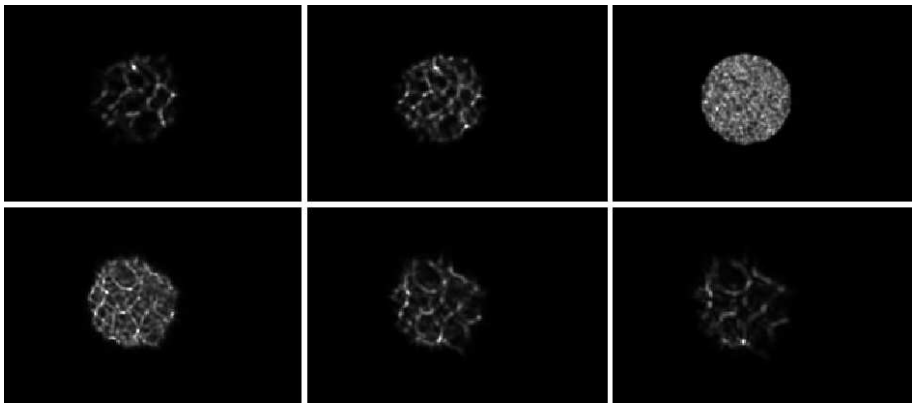

Figure 4.19: Broad-band images of the pupil propagated with out the CRO. A white light LED is used as the source. The phase plates are placed close to the pupil. The pupil is relayed to the detector where it is recorded. Additional images are recorded in planes on either side of the pupil plane. The speckles appear to be slightly blurred.

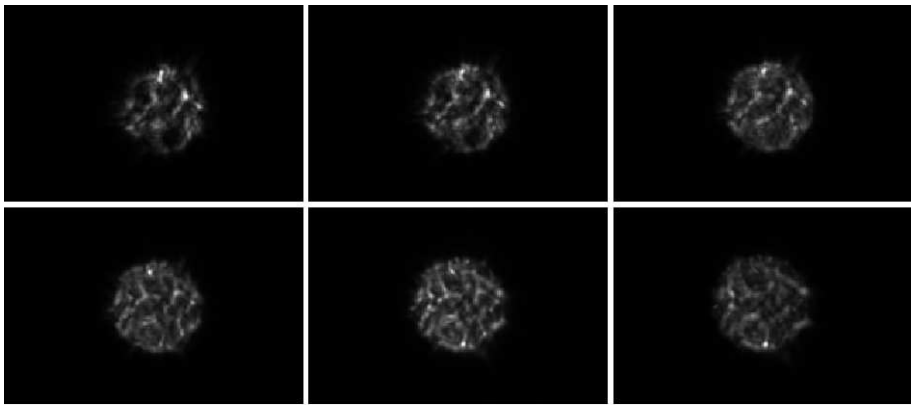

Figure 4.20: Broad-band images of the pupil propagated with the CRO. A white light LED is used as the source. The phase plates are placed close to the pupil. The pupil is imaged through the CRO and then relayed to the detector where it is recorded. Additional images are recorded in planes on either side of the pupil plane. The speckles appear to be greatly blurred in all the planes.

5. CHAPTER FIVE

"Partave-khur se hai shabnam ko fana'a ki taaleem
Main bhee hoon ik inaayat ki nazar hone tak"

"Dew learns the lesson of mortality from sunlight
Similarly, my journey will be complete once starlight shines on me"
- Mirza Ghalib

5.1. nlCWFS-Generation 2 Optical Design Using Dichroics

In this section I discuss the second generation of the nlCWFS optical design. The nlCWFS operates in the visible and requires images measured in at least four Fresnel planes. The location of the Fresnel plane relative to the pupil is inversely related to the wavelength. Therefore in order to image sharp speckles in the Fresnel planes chromatic compensation needs to be applied. In chapter 4 I discussed using the chromatic re-imaging optics (CRO) to apply a prescribed amount of wavelength dependent shift to each Fresnel plane in order to correct the dispersion. The results of using the CRO in the laboratory are not conclusive because the phase screens used to generate turbulence are dispersive. Since the amount of dispersion is not know and has not been studied it is not possible to compensate for the phase screen dispersion in the CRO optical design. The unavailability of dispersion-free phase screens and general complexity of the CRO design led us to pursue an alternate avenue.

In the second iteration of the nlCWFS optical design the Fresnel planes are split in color with the use of dichroics. The dichroic solution is not perfect as it restricts the spectral bandwidth across which chromatic effects are experienced, but does not correct for the chromatic effects. Each dichroic reflects a limited band-width of $\leq 100\,\text{nm}$ which should result in negligible blurring

of speckles. The first dichroic reflects blue light between $380 - 480$ nm and forms channel 1. The second dichroic reflects green light between $520 - 610$ nm and forms channel 2. The third dichroic reflects orange light between $675 - 760$ nm and forms channel 3. The fourth channel receives light transmitted by the third dichroic and is sensitive to red light between $830 - 900$ nm. Maintaining the Fresnel numbers of ± 5.4 and ± 7.5 and using the central wavelength from each band the Fresnel propagation distances are calculated using Eq. 4.8[1]. The theoretical and experimentally measured Fresnel propagated distances relative to the pupil plane are listed in Table 5.1. The experimental distance measurement for Fresnel planes 1 and 3 is marked NA for "not available" as those two Fresnel planes are not accessible due to the hardware design. Figure 5.1 shows the relayed pupil plane and lays out how the four Fresnel planes are split in wavelength using dichroics D1, D2, and D3. Fresnel planes 1 and 3 are formed on the left side of the pupil plane and Fresnel planes 2 and 4 are formed on the right side of the pupil plane. Eleven, half-inch mirrors are used to direct light through the four channels. Light from each of the four channels is collected by the doublet L4 which images each of the Fresnel planes onto a common detector. The doublet L4 consists of two achromats, which have an effective focal length of 300 mm each, cemented together making the combined effective focal length of L4 equal to 151.3 mm at $0.43\,\mu$m. When a single lens was used the dominant aberration observed was $0.8\,\lambda$ of distortion. Switching to a doublet reduced the distortion to $0.0003\,\lambda$

L4 has a 40 mm diameter, which is large enough to accommodate beam and speckle diffraction over the propagation distances in the four channels. The distance between the pupil plane and L4 is different through each of the four channels; this ensures that the distance of each of the Fresnel planes to L4 is constant at 277.21 mm. The detector used is the Andor iXon3 897 EMCCD, it has 512×512 active pixels and each pixel size is $16 \times 16\,\mu$m. The detector has an 8.2×8.2 mm imaging area which makes it difficult to simultaneously image four 0.98 mm diameter spots on the detector. A careful geometrical analysis followed by a Zemax raytrace was performed to determine the angles at which light from the four paths should be incident on L4 in order to image the spots

[1]Fresnel numbers of ± 5.5 and ± 7.5 are used because they led to successful reconstruction of simulated data

on the detector. All distances between the pupil and L4 traced through each of the four channels are listed in Table 5.2. Figure 5.2 shows the four channels traced through the actual hardware.

The schematic shown in Figure 5.3 shows the incident light from one of the paths imaged by L4 on to the detector. I need to make sure that light from the four paths does not vignette at L4 and is able to image the 0.96 mm diameter spot on the detector's imaging area. The ray height at L4 must be less than 20 mm, the radius of L4. height; the ray height is arbitrarily selected. The distance t_1 is equal to d_{20}. The incident angle at L4 can be determined by the following equation.

$$\theta_1 = \frac{y_1}{t_1} \tag{5.1}$$

For small angles where $\theta = \sin\theta$ we can use the paraxial equations for refraction to determine the angle θ_1':

$$\theta_1' = \theta_1 - y_1\phi_{L4} \tag{5.2}$$

here ϕ_{L4} is the power of the lens L4 which is equal to $\frac{1}{f_{L4}}$. Next I find the distance t_2 by using the relation

$$t_2 = \frac{y_1}{\theta_1'} \tag{5.3}$$

since I set the distance between the Fresnel planes and L4 to be 277.21 mm I can use the Gaussian imaging equation to determine the distance between L4 and the detector. This distance is marked t_1' in Figure 5.3.

$$\frac{n'}{t_1'} = \frac{n}{-277.21} + \frac{1}{f_4} \tag{5.4}$$

here n' and n are the index of refraction in the image plane and the object plane, respectively. I find $t_1' = 331.659$. t_3 can be found by subtracting t_2 from t_1'. Finally I can obtain the ray height at the detector by using the relation.

$$y_1' = \theta_1' \; t_3 \tag{5.5}$$

As mentioned earlier I want to ensure that the ray height does not't exceed the detector imaging area. If the ray height does exceed the detector imaging area I change either the ray height y_1 or the distance t_1 and re-work the above calculations. These are first order calculations which give me an idea of the type of distances, angles and lens diameters that will work. Before the design was implemented a Zemax raytrace was carried out which gave detailed information about the aberrations associated with each configuration. The Zemax raytrace was extracted into CAD to better illustrate the rays being refracting off of L4 and hitting the detector, see Figure 5.4. The aberrations present in each of the four spots imaged on the detector are listed in Table 5.3.

Table 5.1: Wavelength Dependent Fresnel Planes.

Fresnel Plane	Central wavelength (nm)	Theoretical distance (mm)	Experimental distance (mm)
1	430	77.21	NA
2	564	58.87	61
3	642	72.38	NA
4	865	53.72	45

5.2. Building the nlCWFS for the 6.5 m MMT Telescope

This section provides an overview of the 6.5 m MMT Natural Guide Star (NGS) adaptive optics system with emphasis on the components that are used to measure wavefronts and on those that direct light to the wavefront sensors. The 6.5 m MMT adaptive optics system is unique in that it employs an adaptive secondary mirror [24]. Using an existing element as the deformable mirror eliminates extra optics that would otherwise cause loss of optical throughput and increase in thermal emissivity of the optical path. This improves performance by cutting integration times and allows imaging of fainter objects. Since the secondary is the deformable mirror, a largely corrected

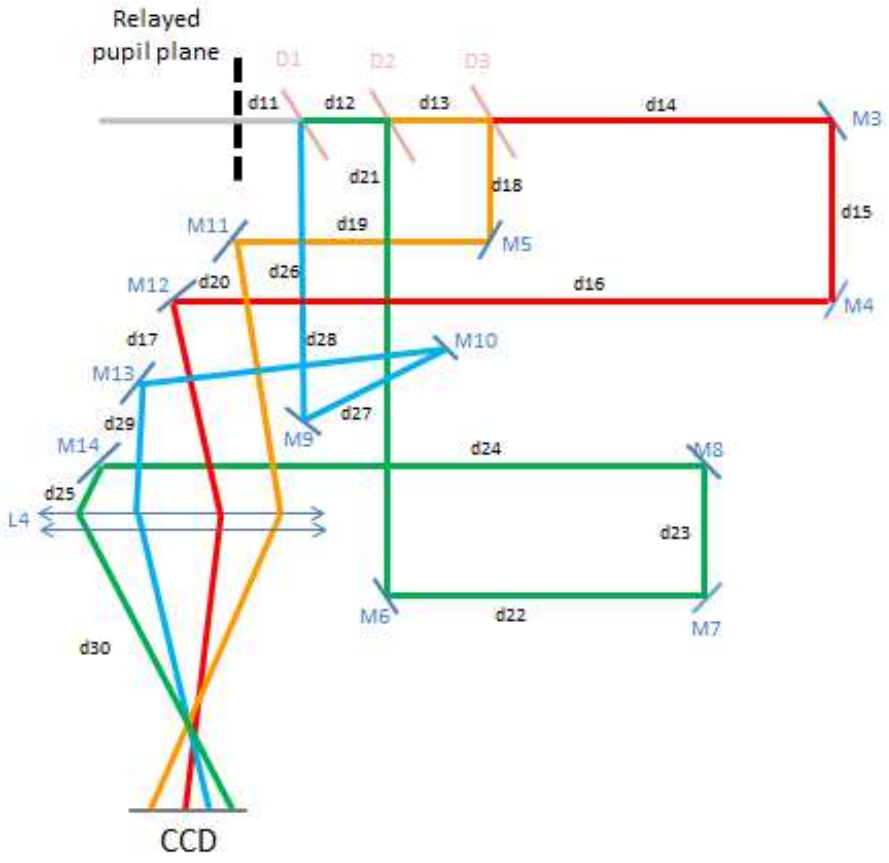

Figure 5.1: The layout shows the optical creation of the four wavelength dependent Fresnel planes with the use of dichroics D1, D2, and D3. Fresnel planes 1 and 3 lie to the left of the re-imaged pupil plane and Fresnel planes 2 and 4 lie to the right of the pupil plane. Blue light reflected by dichroic D1 forms channel 1, green light reflected by dichroic D2, forms channel 2, orange light reflected by dichroic D3 forms channel 3, and red light transmitted by dichroic D3 forms channel 4. Lens L4 images the four Fresnel planes on to the CCD.

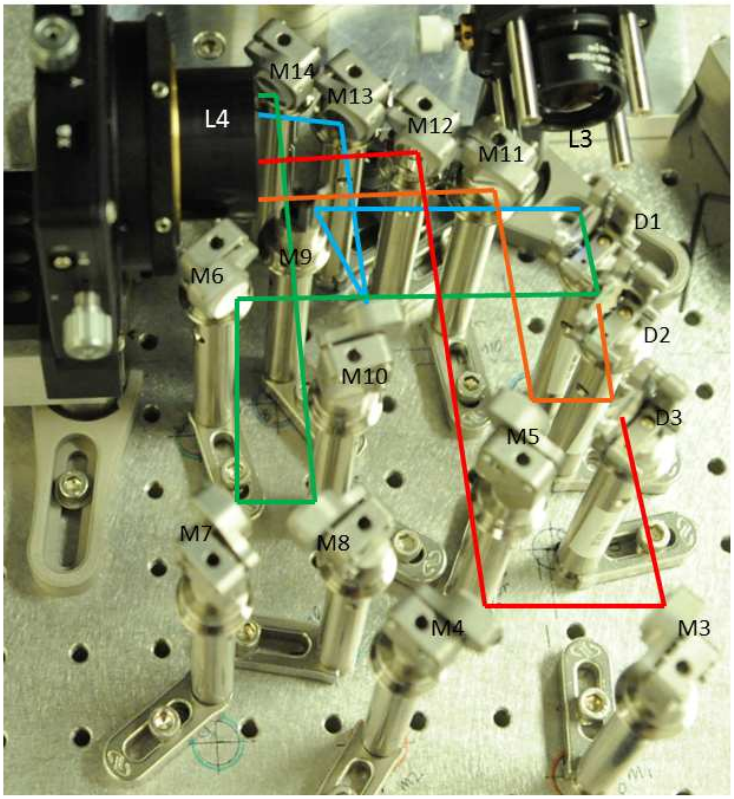

Figure 5.2: The optical path traced through the hardware for the four channels is shown. The relayed pupil plane lies between lens L4 and dichroic D1. All the channels lead to the doublet L4 which images the four Fresnel planes on to a common detector.

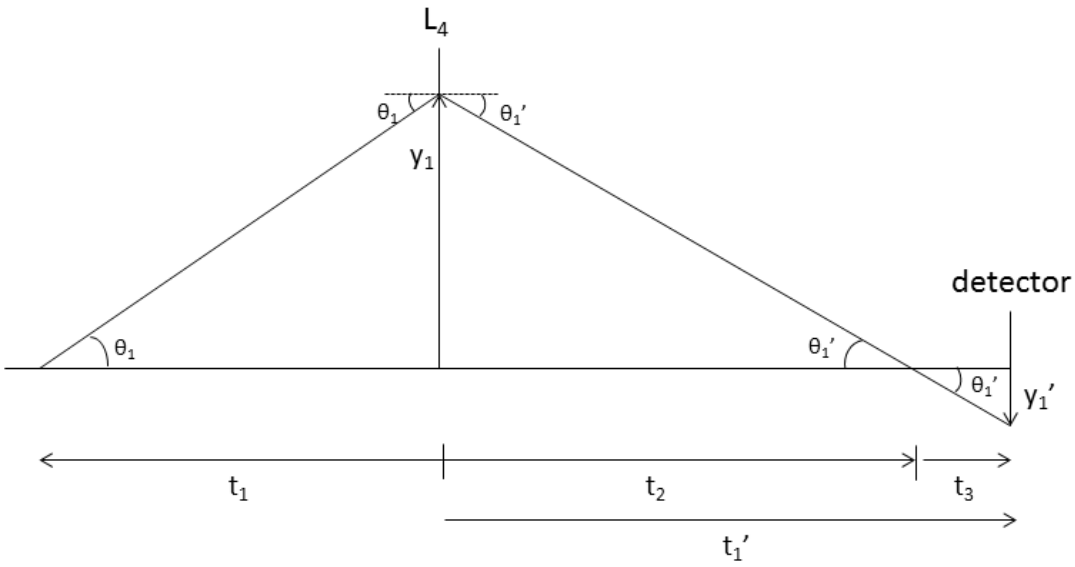

Figure 5.3: Paraxial raytrace. A first order model showing a raytrace through lens L4 which refracts the ray onto the detector. y_1 is the ray height at L4 and y_1' is the ray height at the detector. The paraxial raytrace is only valid for small angles and is initially done to get a rough estimate of whether or not it will be possible to fit four beams on a single detector. A detailed Zemax raytrace followed this process.

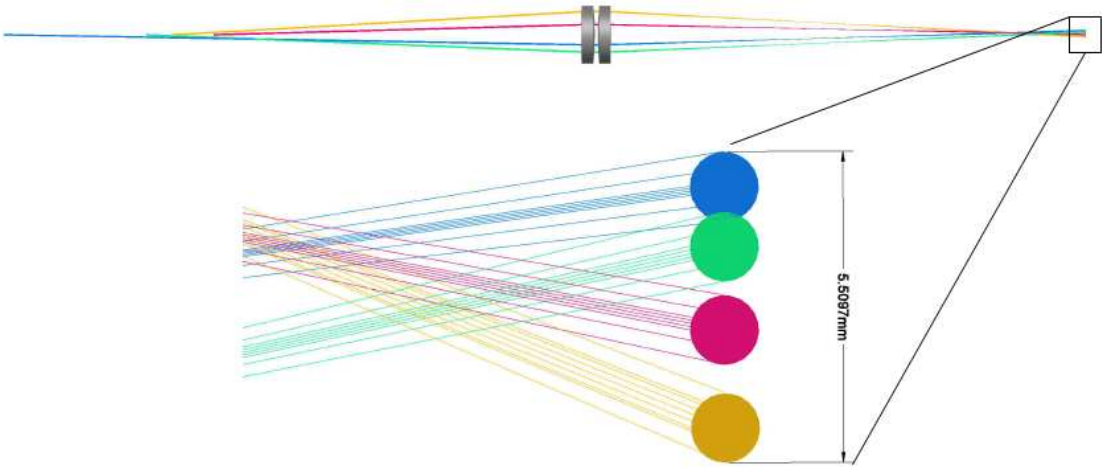

Figure 5.4: Rays from the four channels are seen incident on L4. L4 images the four Fresnel planes onto the detector. The Zemax raytrace is carried out to ensure that there is no vignetting at L4 and that the four spots fit on the detector. The figure shown is a CAD extraction of the Zemax model. The Zemax model was done by me and the CAD extraction was done by Andrea Tuffli.

Table 5.2: 4 Channel Assembly

Distance title	Theoretical separation (mm)	Experimental separation (mm)
d11	10	NA[2]
d12	25	32
d13	25	28
d14	58	43
d15	40	45
d16	128	123
d17	45	48
d18	20	25
d19	60	65
d20	65	65
d21	100	100
d22	55	50
d23	20	30
d24	120	115
d25	5	5
d26	70	70
d27	35	29
d28	60	59
d29	24	24
d30	332	332

Table 5.3: Aberrations

Central wavelength (nm)	Coma W_{131} (λ)	Field Curvature W_{220} (λ)	Astigmatism W_{222} (λ)	Distortion W_{311} (λ)
430	0	0.0002	0.001	0.0064
564	0	0	0.0009	0.0182
642	0.0002	0.0014	0.0009	0
865	0.0001	0.0002	0	0.0034

beam is seen by any instrument mounted at Cassegrain focus with out the need to reconfigure the adaptive optics system. In order to use the nlCWFS with the 6.5 m MMT, the nlCWFS optics have to either be built on to or attached to a structure referred to as the top-box. A description of the

top-box follows.

5.2.1. Natural Guide Star Top-box

The $1.8\,$m diameter structure called the top-box consists of a $100\,$mm thick octagonal optics bed cast out of aluminum. The top-box houses the SHWFS, and all the optics that direct light to the wavefront sensor. The basic top-box optical layout is shown in Figure 5.5 where light comes from the telescope and is focused to the SHWFS. Large cutouts made in the panels give access to the top-box interior. The nlCWFS breadboard is bolted onto the top-box through one of these panels. Here I focus only on the optics that direct light from a NGS to the wavefront sensors, for a detailed description of the top-box optics please refer to Michael Hart's paper [25].

The f/15 beam from the telescope enters the top-box from above. Before the light comes to focus, it encounters a dichroic beamsplitter which transmits infrared light and reflects visible light ($< 1\,\mu$m). Visible light from the reference star is reflected upward from the dichroic beamsplitter at a 30 degree angle to the incoming beam. The light rays go through the f/15 focus and reflect at a 60 degree angle, from a small fold mirror, into the plane of the optics bed. The light is then collimated by an off-axis paraboloid, called OAP1, and sent to a steering mirror. OAP1 forms a real image of the entrance pupil, which is the secondary mirror, on the steering mirror. For this reason the steering mirror is called the pupil-steering mirror (PSM). The PSM is used to center the NGS in the field of the wavefront sensor while the telescope is pointed at the science object. Collimated light is reflected from the PSM and is focused by a second off-axis paraboloid, OAP2, to a point in front of the wavefront sensor. OAP2 relays the intermediate image of the pupil, formed by OAP1 at the PSM to infinity [20].

5.2.2. Integrating the nlCWFS with the 6.5 m MMT Telescope Top-box

In this section I discuss integrating the nlCWFS optics with the top-box. A cube beamsplitter (BS1) is placed in the optical path between OAP2 and the SHWFS, to reflect $50\,\%$ of the light to the nlCWFS optics. The other half of the light is transmitted to the MMT AO SHWFS. The

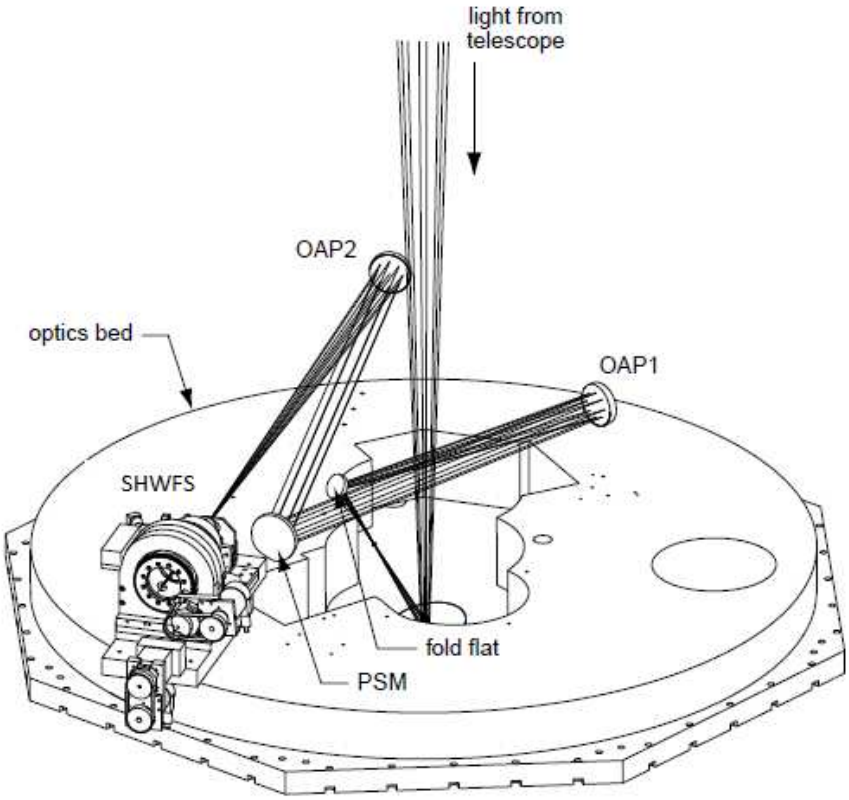

Figure 5.5: Basic top-box optical layout. Light from the telescope is shown entering the top-box from above. The light reflects from the dichroic beamsplitter and goes through the f/15 focus. The light is folded into the plane of the optics bed, where it is, collimated by OAP1, reflected by the PSM, and focused by OAP2 into the SHWFS [20].

diversion of light to the nlCWFS optics is illustrated in the schematic shown in Figure 5.6. The beamsplitter reflects light to mirror M1 which directs light to mirror M2. M1 and M2 are mounted on Newport precision rotation stages, they allow for 360^{o} continuous rotation and can be remotely operated with a stepper motor. Mirrors M1 and M2 are used to align the pupil and focal planes. The f/23 beam comes to focus in between M1 and M2. The f/23 focus is located $566.96\,$mm from BS1 and $5\,$mm from M2. The beam diameter at OAP2 is $55.5\,$mm and it focuses an f/23 beam. The beam diameters at the nlCWFS optical components are found by using the f-ratio and the spacing between the optical elements BS1, M1, M2, and the f/23 focal point. The formula that relates the f-ratio, the intermediate spacing, and the beam diameter is:

$$D_{element} = \frac{d}{f/\#} \tag{5.6}$$

where $D_{element}$ is the beam diameter at the optical element, d is distance from the optical element to the focus, and the focal ratio $f/\# = f/D$ gives the ratio between the focal length of the optical element and the beam diameter at the optical element. The beam diameter at BS1 is:

$$D_{BS1} = \frac{d_2}{f/\#} = \frac{566.96}{23} = 24.65\,\text{mm} \tag{5.7}$$

here d_2 is the distance between BS1 and the focal point. The beam diameter at M1 is:

$$D_{M1} = \frac{d_3}{f/\#} = \frac{200}{23} = 16.35\,\text{mm} \tag{5.8}$$

here d_3 is the distance between M1 and the focal point. The beam diameter at M2 is:

$$D_{M2} = \frac{d_5}{f/\#} = \frac{5}{23} = 0.22\,\text{mm} \tag{5.9}$$

here d_5 is the distance between M2 and the focal point. The beam sizes at key elements and their distance to the f/23 focus are listed in Table 5.4. A lens L1 placed after M2 will re-image the pupil formed at the PSM by OAP1. The pupil at the PSM has a diameter of $55.5\,$mm, I want to signifi-

cantly demagnify this pupil before it enters the four channels. Magnification can be expressed as a ratio of two focal lengths. The focal length of OAP2 is 1269.4 mm. Using a 45 mm focal length lens will allow for a $3.54\,\%$ demagnification of the original pupil. The ratio of the two focal lengths gives the beam magnification and determining the beam size after L1 is a simple matter of multiplying the magnification with the beam diameter at OAP2.

$$m_{L1} = \frac{f_{L1}}{f_{OAP2}} = 0.0354 \tag{5.10}$$

$$D_{L1} = m_{L1} * D_{OAP2} = 1.96\,\text{mm} \tag{5.11}$$

Since the PSM lies 1269.4 mm in front of OAP2 it lies 2584.5 mm in front of L1. The Gaussian imaging equations can be used to determine the location of the re-imaged pupil with respect to L1.

$$\frac{n'}{z'} = \frac{n}{z} + \frac{1}{f} \tag{5.12}$$

here n' and n refer to the refractive index in the medium where the image and object are formed, respectively. z' and z refer to the respective image and object distance from the lens, and f is the focal length of the imaging lens. The re-imaged pupil is formed 45.798 mm in front of L1. I want to further demagnify the almost 2 mm beam in order to keep the Fresnel distances short. Recall that the Fresnel distance scales as the square of the beam radius. Using an afocal relay where lens L2 has a focal length of 60 mm and lens L3 has a focal length of 30 mm I can demagnify the incoming beam by $50\,\%$. The re-imaged pupil has a diameter of 0.98 mm. The Gaussian imaging equation is used again to determine that the re-imaged pupil lies 35 mm behind L3. The re-imaged pupil is designed to lie 10 mm in front of the first dichroic D1.

The actual hardware and optics for the nlCWFS is built on a 4 ft $\times$ 1 ft $\times$ 2.4 in breadboard so that it can be bolted to the top-box through one of its side panels. The breadboard mounted with the optics and the hardware is shown in Figure 5.7. All the components discussed in this section are shown as well as the four channel assembly discussed in section 5.1.

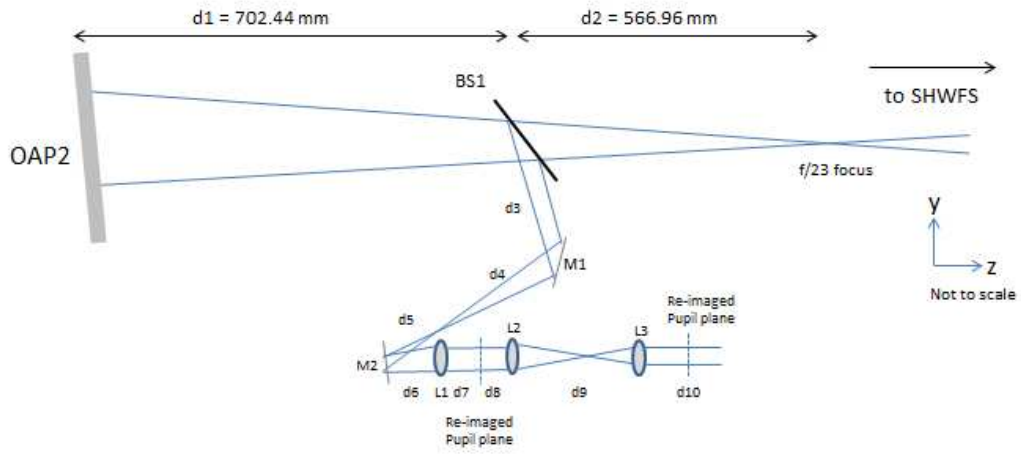

Figure 5.6: Shows the schematic of how light being focused by OAP2 is intersected by BS1, before the focal point, to direct half the light to the nlCWFS optics. The remainder of the light is transmitted by the BS1 to the SHWFS.

Table 5.4: Optical beam parameters

Optical element	Beam diameter (mm)	Distance to f/23 (mm)
OAP2	55.5	1269.4
BS1	24.65	566.96
M1	16.35	365
M2	0.22	-5
L1	1.96	-45
L2	1.96	-130.79
L3	0.98	-220.79

A solid-works design was carried out by Manny Montoyo to facilitate the mounting of the nlCWFS breadboard onto the top-box. Figure 5.8 shows one of the views of the solid-works design where the nlCWFS breadboard is mounted onto the top-box through one of its side-panels. Light from OAP2 is intersected by BS1 and directed to the nlCWFS optics.

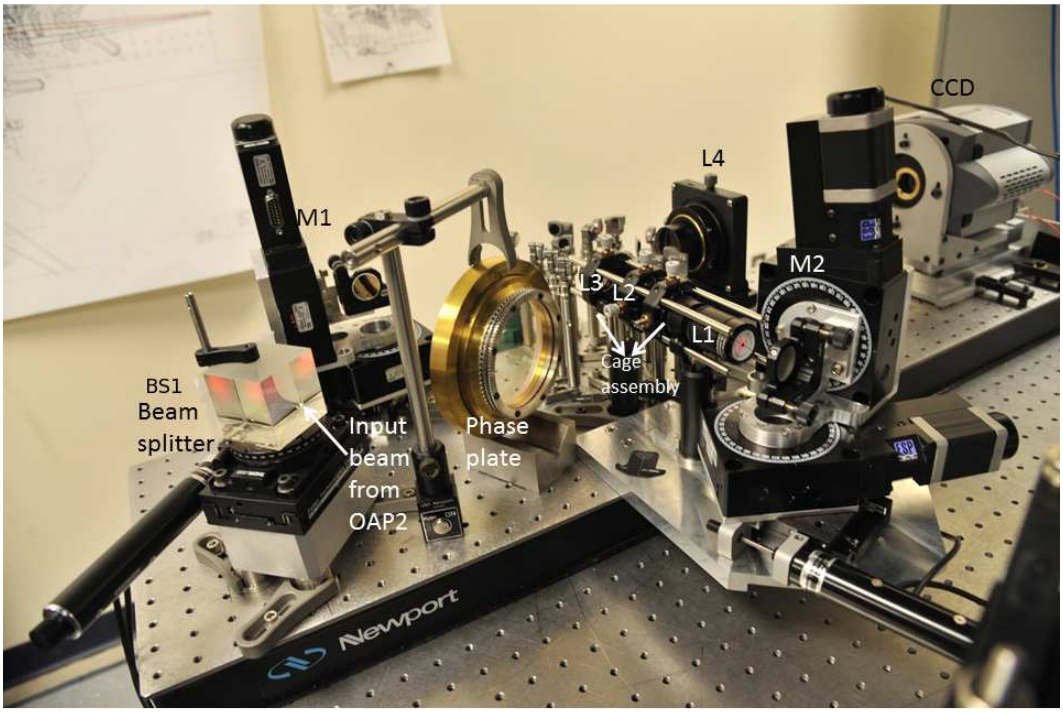

Figure 5.7: The nlCWFS optics and CCD built on a breadboard. Light from the telescope is intercepted by the beam splitter which reflects light to M1. M1 reflects the light, which comes to a focus 5 mm from M2. M2 redirects the expanding beam to L1 which collimates the beam and images the pupil. The pupil is demagnified and re-imaged by the afocal relay made up of L2 and L3. The pupil light is split by dichroics into four channels. L4 images the four Fresnel planes onto a single CCD. The phase plate is inserted on a make-shift stage in case turbulence needs to be introduced in to path.

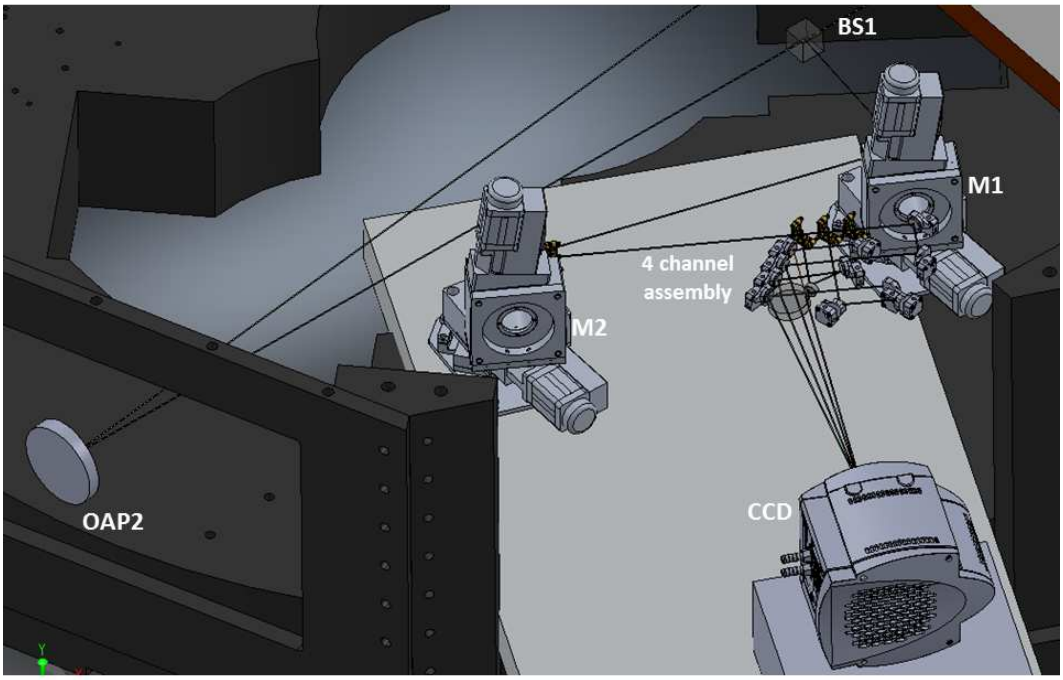

Figure 5.8: Mechanical drawing shown the nlCWFS breadboard bolted on to the top box through a side panel. Light from OAP2 is intersected by a beamsplitter BS1 before the f/23 focus. BS1 reflects $50\,\%$ of the light to the nlCWFS optics and transmits $50\,\%$ of the light to the MMT AO SHWFS, which is not shown in this figure. Light from BS1 is sent to M1, M2 and on to the four channel assembly. After light passes through the four channel assembly the four Fresnel planes are imaged onto the CCD.

5.2.3. Observing with the nlCWFS-Generation 2

The first 6.5 m MMT observing run using the nlCWFS was carried out by Johanan Codona, Kelsey Miller, and Phil Scott in December of 2013. Mounting the nlCWFS breadboard to the top-box for the observing run proved to be quite challenging. Mirrors M1, M2, and the cage assembly holding lenses L1, L2, and L3 had to be removed to fit the breadboard through the panel. After the breadboard was mounted to the top-box Kelsey Miller and Phil Scott were able to align the nlCWFS optics to the top-box laser. Three of the four spots were seen on the detector. It is unclear whether the fourth spot was too dim to make it through the fourth dichroic or was unaligned. With star light only two spots could be seen on the CCD. This can potentially result from misalignment of the top-box laser. It can also be caused due to a shift in the nlCWFS optics after they were aligned to the top-box laser. Due to misalignment errors data obtained from this run was not very useful. The effort was however, hugely beneficial in identifying the challenges with the nlCWFS-Generation 2 optical design. It was clear that aligning four spots on a single detector was challenging, especially in a limited amount of time which is the situation for an observing run since the instrument is mounted to the top-box hours before the observation. The unavailability of a coudé path makes alignment even more challenging. The lessons learned from this observing run led to a nlCWFS-Generation 3 optical design which is discussed in the next section.

5.3. nlCWFS-Generation 3 Optical Design

The single detector design of Generation 2 was motivated by the eventual goal of doing simultaneous real-time reconstruction. The single detector design proved challenging to align and there was a need to acquire on-sky data for algorithm development and to prove the nlCWFS concept on sky. As a result Olivier Guyon and Johanan Codona developed and built the nlCWFS-Generation 3 design which uses several cameras and allows for multiple-Fresnel planes without making co-alignment difficult. Light from OAP2 is split by a 50-50 beamsplitter between the nlCWFS and the AO SHWFS. Light coming to the nlCWFS is split four ways using 50-50 beamsplitters, see

Figure 5.9. Each of the four cameras receive $12.5\,\%$ of the light. The four cameras used are Canon SL1 DSLR cameras, each camera is $22.3 \times 14.9\,$mm in size, has a pixel size of $4.3\,\mu$m, and has a read-out-noise of 3 electrons. The camera can record in three colors RGGB, which automatically implements the dichroic mechanism of the Generation 2 design, leading to the simultaneous acquisition of three Fresnel planes per camera. A total of 12 Fresnel planes are recorded. Initially the size of the Fresnel planes imaged on the camera was too large; in order to fix this problem a lens is used to image a smaller field onto the cameras. The f/23 beam focused by the MMT OAP2 is re-imaged by a sequence of lenses. The four Fresnel plane cameras marked as DSLRs in Figure 5.9 are placed before the re-imaged focal plane. A fifth Canon SL1 DSLR camera splits $10\,\%$ of the light from fourth Fresnel plane camera to form a focal plane camera. A Canon DSLR 60D camera splits $10\,\%$ of the light from the third Fresnel plane camera to direct light to the second SHWFS. A secon SHWFS in addition to the MMT AO SHWFS is used so that synchronized data can be obtained with the nlCWFS and the SHWFS cameras. This is necessary since the MMT AO SHWFS has a different frame rate than the nlCWFS cameras being used. A master shutter is used ahead of all the cameras to allow for simultaneous data acquisition. The simultaneous acquisition of the data with the nlCWFS and the SHWFS will allow us to compare wavefront sensing and reconstruction performed by the two sensors. The reconstruction is not performed in real time.

For the observation run Guyon and Codona successfully mounted the nlCWFS optics to the top-box and were able to align the nlCWFS optics to the alignment laser. The star Arcturus was successfully observed with all six cameras. Both open loop and closed loop data was obtained; for closed loop data the loop was only closed on the MMT AO SHWFS. The nlCWFS and the second SHWFS benefited from seeing a corrected beam. This was a successful observing run in which the star was imaged in all the cameras. Representative images obtained with each of the cameras are shown in Figures 5.10, 5.11, 5.12, 5.13, 5.14, 5.14. The size of the imaged star can be seen to change as it is imaged in different Fresnel planes. Since Arcturus is a red star the images obtained in the blue band are comparatively dim. We are currently in the process of analyzing and reducing the data. I hope to be able to use the 12 Fresnel planes and reconstruct the wavefront in the pupil

using the nlCWFS reconstruction algorithm.

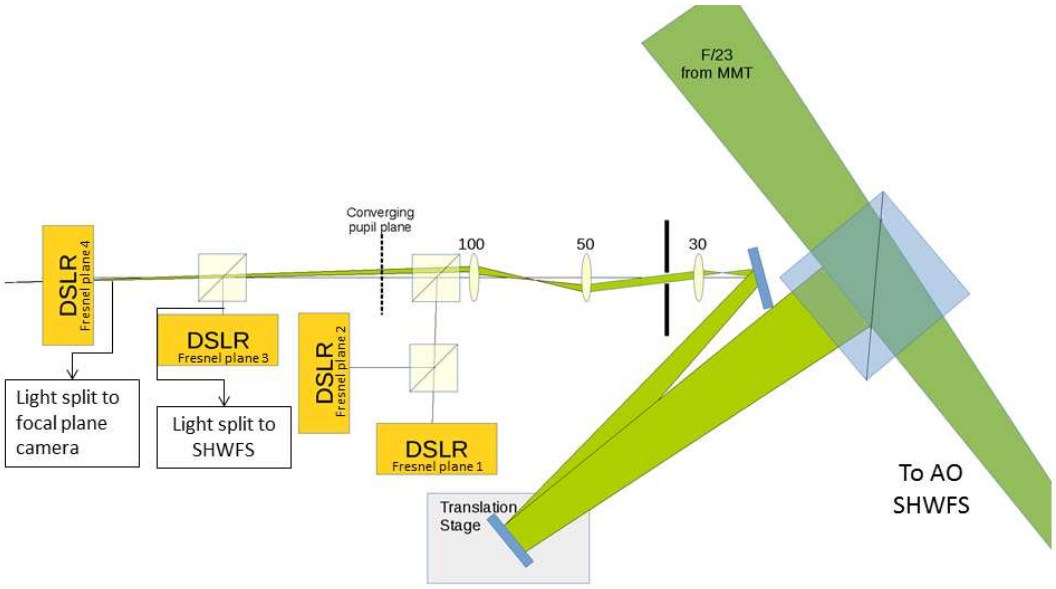

Figure 5.9: The figure shows the nlCWFS-Generation 3 optical design. The four DSLR cameras shown are Fresnel plane cameras. The RGGB nature of the cameras allows for the simultaneous acquisition of three Fresnel planes per camera. $10\,\%$ of the light is split from the Fresnel plane 4 camera to form the focal plane camera and. Similarly $10\,\%$ of the light is split from the Fresnel plane 3 camera to send light to the SHWFS. The Generation 3 optical design layout is provided by Johanan Codona.

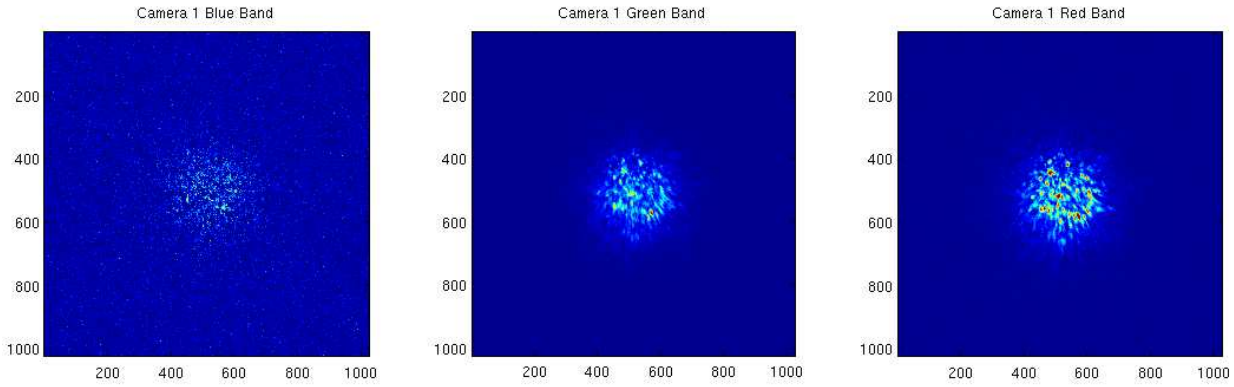

Figure 5.10: Arcturus imaged in the blue, green, and red band with camera 1.

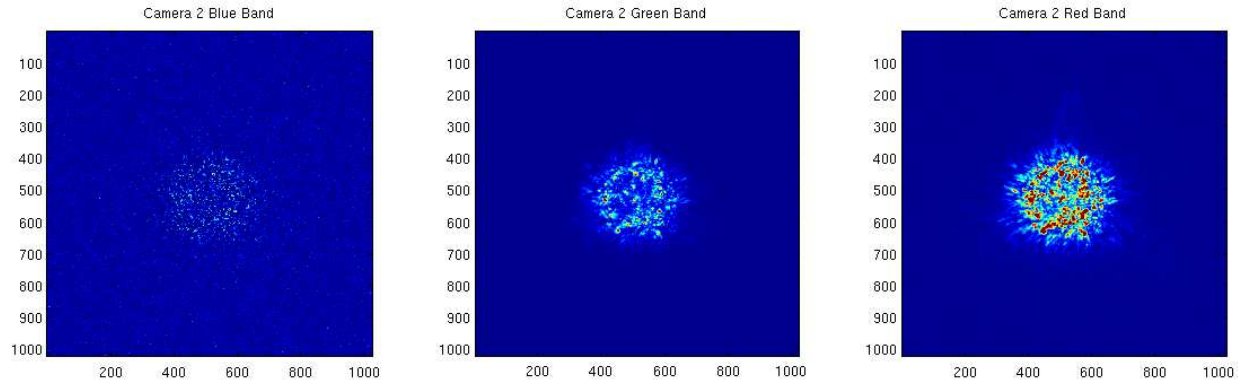

Figure 5.11: Arcturus imaged in the blue, green, and red band with camera 2.

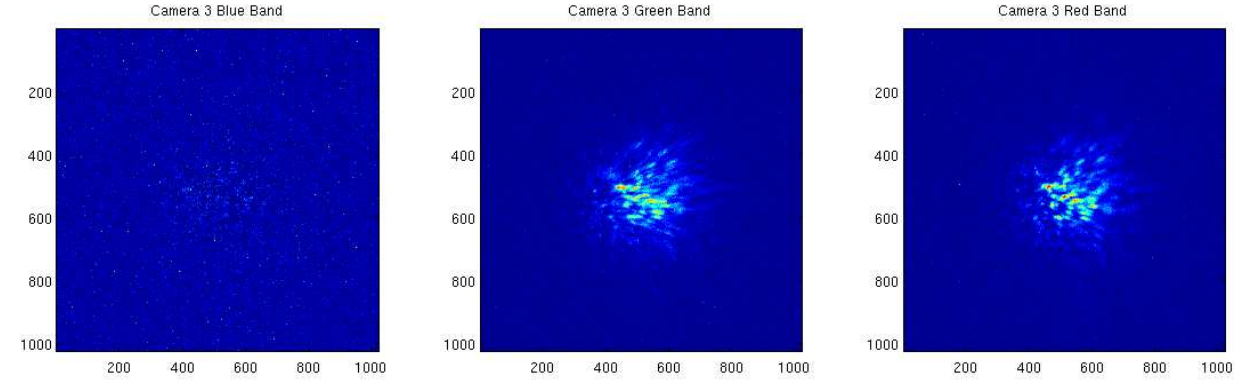

Figure 5.12: Arcturus imaged in the blue, green, and red band with camera 3.

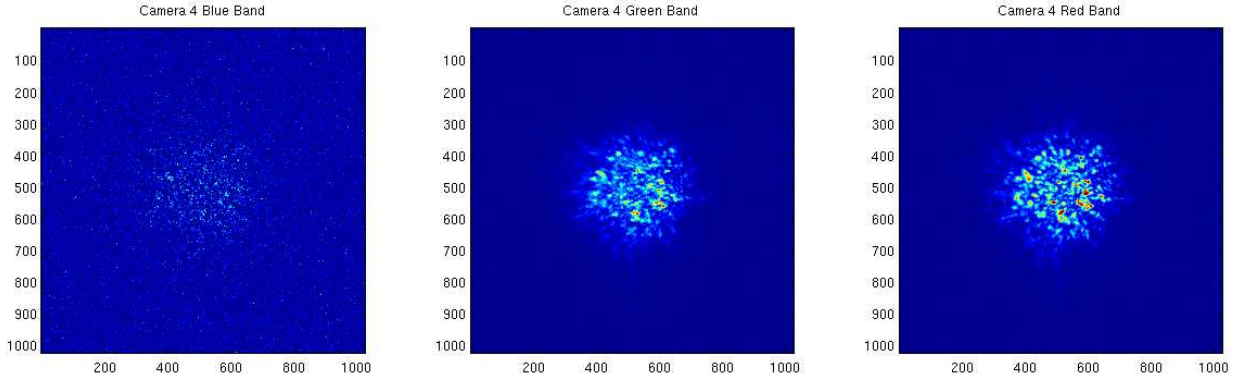

Figure 5.13: Arcturus imaged in the blue, green, and red band with camera 4.

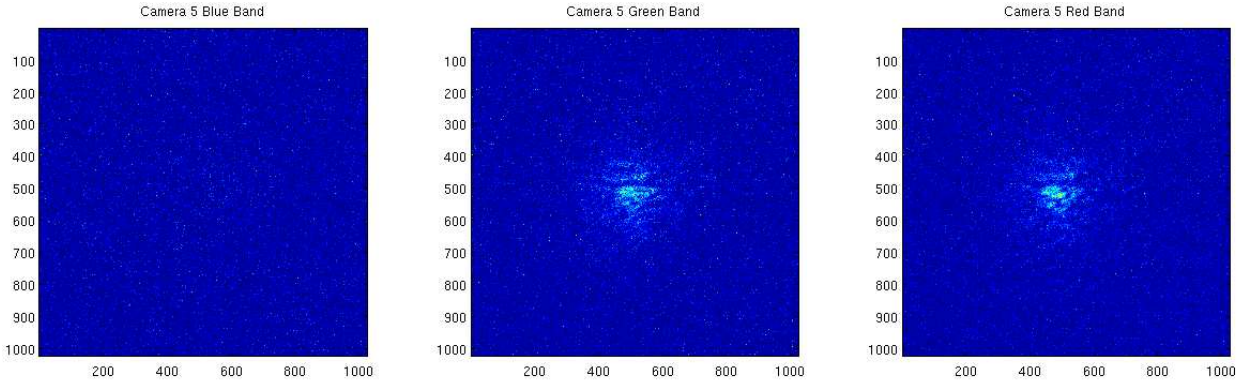

Figure 5.14: Arcturus imaged in the blue, green, and red band with the focal plane camera.

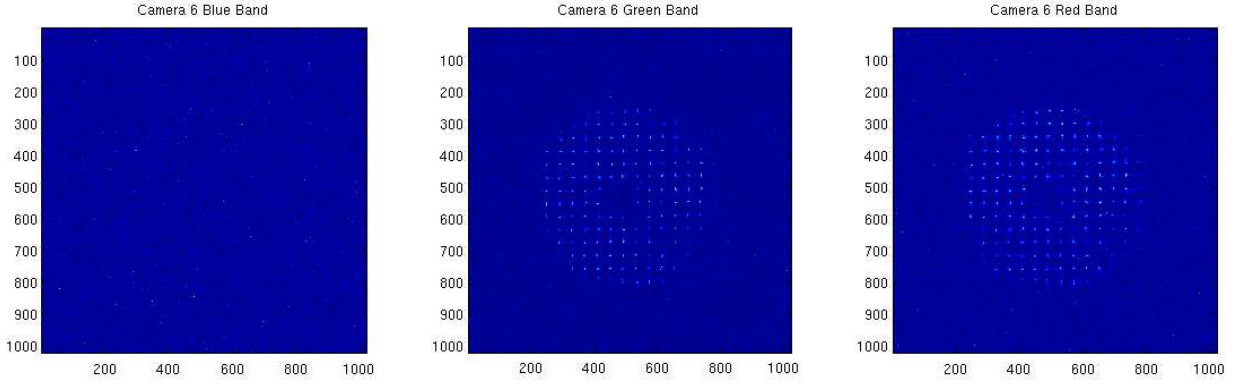

Figure 5.15: Arcturus imaged in the blue, green, and red band with the second SHWFS camera.

6. CHAPTER SIX

"Sukoon mahal hai qudrat ke kaarkhane mein
Sabat aik taghiyar ko hai zamane mein

The universe is in continuous turmoil
the only thing constant is change itself"
- Allama Iqbal

6.1. Conclusion

In this dissertation I develop a highly sensitive non-linear Curvature Wavefront Sensor (nlCWFS) which is able to operate at the sensitivity limit imposed by fundamental physics. The nlCWFS is a diffraction-limited wavefront sensor because it uses the full spatial coherence of the pupil plane as opposed to conventional wavefront sensors, that operate at the seeing limit. In order to maintain its diffraction limited sensitivity, the nlCWFS technique is best suited for high precision AO on bright natural guide stars (NGS). The nlCWFS is optimal for extreme AO and visible AO systems which require high-accuracy control of low-order modes. It is ideal for direct imaging of exoplanets and circumstellar disks around nearby stars, where achieved performance is measured by how large a contrast can be obtained between the central PSF and a point at a separation of one to a few (λ/D). High contrasts are achieved by maintaining wavefront control accuracy and exquisite control of low-order modes is essential for high contrast coronagraphic imaging. The nlCWFS has been tested in the laboratory and on-sky, in open loop.

The journey of developing the nlCWFS began with carrying out realistic simulations comparing the performance of the nlCWFS with the established and widely used Shack-Hartmann Wavefront sensor (SHWFS). The simulations produced promising results and delivered high contrasts for the nlCWFS compared to the SHWFS. When the lowest spatial frequencies were con-

sidered, for a $1.5\,$m telescope at $\lambda = 790\,$nm, and $D/r_0 = 12.7$ the high contrast detection limit at $0.11\,$arcseconds from $m = 10$ star is 3 magnitudes deeper with the nlCWFS than with the SHWFS. Since the nlCWFS operates in the non-linear regime in order to maintain sensitivity to low-order modes, an unconventional non-linear reconstructor had to be developed. An iterative Gerchberg-Saxton reconstructor was chosen, of course other faster algorithms may exist. Results obtained from the simulations encouraged me to setup a laboratory experiment which would verify that laboratory data obtained in the non-linear regime could be used to reconstruct the pupil plane wavefront. Phase screens prescribed with Kolmogorov statistics were used to generated the turbulent wavefront in the pupil plane. The laboratory demonstration showed that the nlCWFS reconstruction algorithm was able to reconstruct the wavefront in all the Fresnel planes where data was acquired.

As light over the entire visible band is used to create the visible nlCWFS, chromatic compensation is needed to keep speckles from blurring which would result in the nlCWFS losing its diffraction-limited sensing ability. Since the nlCWFS relies on data acquired in Fresnel planes on either side of the pupil plane the chromatic blurring of speckles is even more significant than it would be in an unpropagated plane. The first optical design to compensate chromatic aberration consisted of an assembly of optics called the Chromatic Re-imaging Optics (CRO). The CRO introduced a prescribed amount of wavelength dependent focus which compensated for chromatic aberration. Speckles recorded with the CRO showed blurring which could result from incorrect placement of the CRO with respect to the pupil plane or due to the fact that the phase screens used are optimized for $1550\,$nm and introduce chromatic aberrations at other wavelengths. The CRO results were not explored in depth as the CRO design was dropped in favor of a simpler design using dichroics. In the second optical design of the nlCWFS dichroics were used to create four wavelength dependent Fresnel planes. The dichroic design does not completely resolve visible band chromaticity but it reduces the band over which chromatic aberration can occur, to $\approx 100\,$nm which is sufficient.

In 2012 the nlCWFS optical design implemented with dichroics was integrated with the $6.5\,$m

MMT NGS AO system. The design imaged the four planes on a common detector which proved to be quite challenging to align especially when the alignment had to be done with the nlCWFS mounted to the NGS topbox with limited access to the optics, and in a short period of time. The first observation taught us that it was extremely difficult to image all four Fresnel planes on to a single detector. This insight led to the development of the third nlCWFS optical design which used a separate camera for each Fresnel plane and also incorporated a focal plane camera. The third nlCWFS optical design uses RGGB cameras which allow the imaging of three wavelength dependent Fresnel planes per camera and therefore maintains the chromatic compensation introduced in the second nlCWFS optical design. In February of 2015 we were able to successfully observe the star Arcturus in all four Fresnel plane cameras. In addition simultaneous wavefront sensing was carried out with the SHWFS. Both the nlCWFS and the SHWFS benefited from seeing a corrected beam as the loop was closed on the MMT AO SHWFS. Calibration and reduction of the observational data is currently underway and will provide a comparison of the on-sky performance of the nlCWFS and the SHWFS.

6.2. Future Applications for the nlCWFS

In the last two decades over 700 exoplanets and over 2000 candidates have been discovered [3]. Advances in AO, infrared detectors, and image processing algorithms have made it possible to directly image several of these exoplanets. High contrast imaging systems utilizing algorithms and techniques such as Locally Optimized Combination of Images (LOCI) [23], Principal Component Analysis (PCA) [1] [35], Angular diffraction Imaging (ADI) [3] [37], advanced coronagraphy [15], nulling interferometry, and phase apodization enable imaging and characterization of Jupiter-mass and in future of Earth-mass planets around nearby stars. At the most basic level these algorithms and techniques work by deepening the contrast by suppressing the PSF of the host star. These techniques rely on exquisite wavefront control, because residual wavefront errors result in speckle noise and leakage which make it difficult to identify a potential exoplanet hiding in the central PSF wing. One of the reasons for poor wavefront control is that current AO systems image in the

near-IR and perform wavefront sensing in the visible. As a result the PSF contrast limit is set by chromatic scintillation that results from Fresnel propagation and could be a factor of two deeper if wavefront sensing and scientific imaging were performed at the same wavelength [11]. The nlCWFS's ability to accurately measure wavefront errors with high efficiency makes it possible to achieve high contrast imaging at shorter wavelengths than previously possible. The other reason why conventional wavefront sensors are unable to deliver residual wavefront errors below $100\,\mathrm{nm}$, in visible is because they are seeing-limited. The nlCWFS is a diffraction-limited wavefront sensor which will greatly enhance performance on $m_v = 12 - 14$ guide stars.

The Gemini Planet Imager (GPI) is a dedicated facility for direct imaging and spectroscopically characterizing exoplanets [26]. GPI is deployed on the $8.1\,\mathrm{m}$ Gemini south telescope. It combines a very high-order adaptive optics system with a diffraction-suppressing coronagraph. PSF from a bright star consists of a static airy pattern and time-varying speckles which are the result of imperfect wavefront correction by the AO system. Over long exposures the fast varying speckles average out and the slow varying speckles (resulting from aberrated optical surfaces) can be calibrated out. If the phase measurements used to control the AO system are biased, the residual phase will not have a zero mean and the speckle pattern will have a persistent component which can be mistaken for a planet [26]. GPI uses a SHWFS based AO system to control the wavefront error. However SHWFS, especially those used for high-order AO systems, are susceptible to aliasing [26] and noise-propagation [14]. Since the SHWFS splits the pupil into subapertures it loses sensitivity to low order modes that dominate atmospheric turbulence and scatter light at narrow angles where a planet is likely to be found and limit wavefront control accuracy. Using a diffraction-limited wavefront sensor such as the nlCWFS will allow better speckle suppression and will deliver high quality wavefront correction to the coronagraphic imager. For the Gemini telescope where typically $r_0 = 0.18\,\mathrm{m}$ replacing the SHWFS with the nlCWFS will result in a gain in sensitivity of (D/r_0) for tip-tilt. This means that, for measuring tip-tilt, the nlCWFS will deliver the same wavefront accuracy as the SHWFS when observing a source that has 1975 times fewer photons. Accurately sensing and correcting tip/tilt is extremely important since it dominates atmospheric

turbulence and is especially important in coronagraphs to ensure the star remains behind the focal plane mask. The gain for higher order modes goes as (X/r_0) where X is the interference spacing required to measure the higher order modes. Operating with the SHWFS GPI is able to measure 10^6 contrast for Beta Pictoris b at 0.75 arcseconds [26]; if GPI was operated with the nlCWFS it could obtain better contrasts at a smaller inner working angle (IWA). The gain in sensitivity can also be translated to smaller integration times on brighter targets. The Spectro-Polarimetric High-Contrast Exoplanet REsearch (SPHERE) instrument on the Very large Telescope (VLT) is another mission dedicated to direct imaging of exoplanets. It uses a coronagraph to block the central star light and polarized filters to extract the signal from the dusty disc. The AO system for SPHERE is based on a SHWFS [28] [34]. The same sensitivity arguments made above in favor of using the nlCWFS in place of the SHWFS apply here. Having a diffraction-limited wavefront sensor will improve the detection limit of dim exoplanets. Images of the planetary system HR 8799 obtained with the SH based MMT AO system at L' and M band place some of the most stringent constraints on planets nearby stars [18] [21] [17]. The nlCWFS will immediately enable better contrast at closer separations, by reducing the residual halo at $3-5\ \lambda/D$ by a factor of two to five from the current SHWFS. This is particularly important for low background L' observations, where the noise at a few λ/D is dominated by residual speckle noise [12].

Some telescopes, such as the Large Binocular Telescope (LBT), the Subaru Cornagraphic Extreme Adaptive Optics (SCExAO) system, and the European Extremely Large Telescope (E-ELT), have selected the Pyramid wavefront sensor (PYWFS) for high contrast imaging. The PYWFS has proven to be more sensitive than the SH and the conventional Curvature wavefront sensors [11]. Simulations carried out by Guyon [13] based on mode perturbation theory show that the linear fixed PYWFS is about as sensitive as the nlCWFS for small perturbations but when the wavefront is less than ideal the linear PYWFS loses sensitivity to low spatial frequencies. The PYWFS splits the focal plane into four quadrants which are re-imaged onto a CCD by a relay lens. In effect four images of the pupil plane are obtained. Deviation of the focal plane spot produces contrast variation in the four quadrants from which slopes are measured. The slopes encode the

wavefront error. In presence of an aberrated PSF the poor sensitivity of the linear fixed PYWFS results both from the linear constraint and the optical range limitation due to the fact that the inner parts of the PSF can spend a significant fraction of the time completely in a single quadrant; this results in poor optical signal for low order aberrations [13]. If a non-linear PYWFS is used some sensitivity to low order modes is restored but is still an order of magnitude below that obtained with the nlCWFS [13]. In addition the non-linear PYWFS reconstructor suffers the same complexity and speed limitation that challenges the nlCWFS. H and K_s band observations of the planetary system HR 8799 with the LBT have enabled the detection of the inner most planet HR8799e [5]. The First-Light Adaptive Optics (FLAO) system on the LBT has been able to obtain 10^{-4} contrast at 0.4 arcseconds [6]. Based on results from the mode perturbation analysis carried out by Guyon [13] the nlCWFS can improve the sensitivity of the detection by an order of magnitude.

There is a need to provide the upcoming extreme-AO systems with a better alternative which maintains sensitivity over all spatial frequencies. The key to observing Jupiter-mass and eventually earth-mass planets in the habitable zone is to obtain a deeper contrast between the central PSF peak and a point $1\ \lambda/D$ to a few λ/D away where an exoplanet could be found. Using a diffraction-limited wavefront sensor like the nlCWFS, will result in an increase in sensitivity, and enable the deeper contrast. Since the nlCWFS can optimally operate in poor seeing it can be used for fast tracking systems where one cannot wait for several iterations of the closed loop. Systems that have a need to place the wavefront sensor before the DM can benefit from the nlCWFS as well as Multi Conjugate Adaptive Optics (MCAO) systems that don't have a DM conjugated to every plane. The nlCWFS is ideal for short-exposure imaging of relatively brighter targets. The object of interest can often be fainter than the background, in these situations the nlCWFS sensitivity scales as D^4, D^2 gain due to collecting power, and D^2 gain due to angular resolution. Whereas sensitivity of conventional wavefront sensors only scales as D^2, gain due to collecting power. The difference is significant for extremely large telescopes like the 25.4 m Giant Magellan Telescope (GMT), the Thirty Meter Telescope (TMT), and the 39.3 m European Extremely Large Telescope (E-ELT). The difference is especially important for the next generation of 100 m class telescopes.

REFERENCES

[1] A. Amara and S. P. Quanz. PYNPOINT: an image processing package for finding exoplanets. *MNRAS*, 427:948–955, December 2012.

[2] H. H. Barrett and K. J. Myers. *Foundations of image science*. Wiley-Interscience, 2004.

[3] E. Bendek, R. Belikov, E. Pluzhnik, and O. Guyon. Compatibility of a Diffractive Pupil and Coronagraphic Imaging. *PASP*, 125:204–212, February 2013.

[4] J. T. Brennan, H. P. Roberts, and C. D. Zimmerman. *A Wave Optics Simulation System*. the Optical Sciences Company, September 2013.

[5] S. Esposito, D. Mesa, A. Skemer, C. Arcidiacono, R. U. Claudi, S. Desidera, R. Gratton, F. Mannucci, F. Marzari, E. Masciadri, L. Close, P. Hinz, C. Kulesa, D. McCarthy, J. Males, G. Agapito, J. Argomedo, K. Boutsia, R. Briguglio, G. Brusa, L. Busoni, G. Cresci, L. Fini, A. Fontana, J. C. Guerra, J. M. Hill, D. Miller, D. Paris, E. Pinna, A. Puglisi, F. Quiros-Pacheco, A. Riccardi, P. Stefanini, V. Testa, M. Xompero, and C. Woodward. LBT observations of the HR 8799 planetary system. First detection of HR 8799e in H band. *Appl.Opt*, 549:A52, January 2013.

[6] S. Esposito, A. Riccardi, E. Pinna, A. Puglisi, F. Quirós-Pacheco, C. Arcidiacono, M. Xompero, R. Briguglio, G. Agapito, L. Busoni, L. Fini, J. Argomedo, A. Gherardi, G. Brusa, D. Miller, J. C. Guerra, P. Stefanini, and P. Salinari. Large Binocular Telescope Adaptive Optics System: new achievements and perspectives in adaptive optics. In *Society of Photo-Optical Instrumentation Engineers (SPIE) Conference Series*, volume 8149 of *Society of Photo-Optical Instrumentation Engineers (SPIE) Conference Series*, page 2, October 2011.

[7] D. L. Fried. Optical Resolution Through a Randomly Inhomogeneous Medium for Very Long and Very Short Exposures. *Journal of the Optical Society of America (1917-1983)*, 56:1372, October 1966.

[8] R. W. Gerchberg and W. O. Saxton. A practical algorithm for determination of the phase from image and diffraction planes. *Optik*, 35:237–246, December 1972.

[9] J. W. Goodman. *Introduction to Fourier Optics*. Roberts & Company, December 2004.

[10] D. P. Greenwood. Bandwidth specification for adaptive optics systems. *Journal of the Optical Society of America (1917-1983)*, 67:390–393, March 1977.

[11] O. Guyon. Limits of Adaptive Optics for High-Contrast Imaging. *ApJ*, 629:592–614, August 2005.

[12] O. Guyon. . *NSF proposal*, 2010.

[13] O. Guyon. High Sensitivity Wavefront Sensing with a Nonlinear Curvature Wavefront Sensor. *PASP*, 122:49–62, January 2010.

[14] O. Guyon, C. Blain, H. Takami, Y. Hayano, M. Hattori, and M. Watanabe. Improving the Sensitivity of Astronomical Curvature Wavefront Sensor Using Dual-Stroke Curvature. *PASP*, 120:655–664, May 2008.

[15] O. Guyon, Y. Hayano, M. Tamura, T. Kudo, S. Oya, Y. Minowa, O. Lai, N. Jovanovic, N. Takato, J. Kasdin, T. Groff, M. Hayashi, N. Arimoto, H. Takami, C. Bradley, H. Sugai, G. Perrin, P. Tuthill, and B. Mazin. Adaptive optics at the Subaru telescope: current capabilities and development. In *Society of Photo-Optical Instrumentation Engineers (SPIE) Conference Series*, volume 9148 of *Society of Photo-Optical Instrumentation Engineers (SPIE) Conference Series*, page 1, August 2014.

[16] J. W. Hardy. *Adaptive Optics for Astronomical Telescopes*. Oxford University Press, July 1998.

[17] A. N. Heinze, P. M. Hinz, M. Kenworthy, D. Miller, and S. Sivanandam. Deep L'- and M-band Imaging for Planets around Vega and ϵ Eridani. *ApJ*, 688:583–596, November 2008.

[18] P. M. Hinz, A. N. Heinze, S. Sivanandam, D. L. Miller, M. A. Kenworthy, G. Brusa, M. Freed, and J. R. P. Angel. Thermal Infrared Constraint to a Planetary Companion of Vega with the MMT Adaptive Optics System. *ApJ*, 653:1486–1492, December 2006.

[19] R. E. Hufnagel and N. R. Stanley. Modulation Transfer Function Associated with Image Transmission through Turbulent Media. *Journal of the Optical Society of America (1917-1983)*, 54:52, January 1964.

[20] R. L. Johnson. *Calibration and testing of the 6.5 m MMT adaptive optics system*. PhD thesis, THE UNIVERSITY OF ARIZONA, October 2001.

[21] M. A. Kenworthy, J. L. Codona, P. M. Hinz, J. R. P. Angel, A. Heinze, and S. Sivanandam. First On-Sky High-Contrast Imaging with an Apodizing Phase Plate. *ApJ*, 660:762–769, May 2007.

[22] A. N. Kolmogorov. the local structure of turbulence in incompressible viscous fluids for very large Reynolds' numbers. *Turbulence, Classic Papers on Statistical Theory*, 1961.

[23] D. Lafrenière, C. Marois, R. Doyon, D. Nadeau, and É. Artigau. A New Algorithm for Point-Spread Function Subtraction in High-Contrast Imaging: A Demonstration with Angular Differential Imaging. *ApJ*, 660:770–780, May 2007.

[24] M. Lloyd-Hart. Thermal Performance Enhancement of Adaptive Optics by Use of a Deformable Secondary Mirror. *PASP*, 112:264–272, February 2000.

[25] M. Lloyd-Hart, J. R. P. Angel, D. G. Sandler, T. K. Barrett, P. C. McGuire, T. A. Rhoadarmer, D. G. Bruns, S. M. Miller, D. W. McCarthy, and M. Cheselka. Infrared adaptive optics system for the 6.5-m MMT: system status and prototype results. In D. Bonaccini and R. K. Tyson, editors, *Adaptive Optical System Technologies*, volume 3353 of *Society of Photo-Optical Instrumentation Engineers (SPIE) Conference Series*, pages 82–93, September 1998.

[26] B. Macintosh, J. R. Graham, P. Ingraham, Q. Konopacky, C. Marois, M. Perrin, L. Poyneer, B. Bauman, T. Barman, A. S. Burrows, A. Cardwell, J. Chilcote, R. J. De Rosa, D. Dillon, R. Doyon, J. Dunn, D. Erikson, M. P. Fitzgerald, D. Gavel, S. Goodsell, M. Hartung, P. Hibon, P. Kalas, J. Larkin, J. Maire, F. Marchis, M. S. Marley, J. McBride, M. Millar-Blanchaer, K. Morzinski, A. Norton, B. R. Oppenheimer, D. Palmer, J. Patience, L. Pueyo, F. Rantakyro, N. Sadakuni, L. Saddlemyer, D. Savransky, A. Serio, R. Soummer, A. Sivaramakrishnan, I. Song, S. Thomas, J. K. Wallace, S. Wiktorowicz, and S. Wolff. First light of the Gemini Planet Imager. *Proceedings of the National Academy of Science*, 111:12661–12666, September 2014.

[27] F. Malbet, J. W. Yu, and M. Shao. High-Dynamic-Range Imaging Using a Deformable Mirror for Space Coronography. *PASP*, 107:386, April 1995.

[28] P. Martinez, E. A. Carpentier, and M. Kasper. Laboratory Demonstration of Efficient XAO Coronagraphy in the Context of SPHERE. *PASP*, 122:916–923, August 2010.

[29] M. Mateen, V. Garrel, M. Hart, and O. Guyon. Results from the laboratory demonstration of the nonlinear curvature wavefront sensor. In *Society of Photo-Optical Instrumentation Engineers (SPIE) Conference Series*, volume 7736 of *Society of Photo-Optical Instrumentation Engineers (SPIE) Conference Series*, page 19, July 2010.

[30] M. Mateen, O. Guyon, and M. Hart. A sensitivity comparison between the non-linear curvature wavefront sensor and the Shack-Hartmann wavefront sensor in broadband. In *Second International Conference on Adaptive Optics for Extremely Large Telescopes. Online at ¡A href=”http://ao4elt2.lesia.obspm.fr”¿http://ao4elt2.lesia.obspm.fr¡/A¿, id.39*, page 39, September 2011.

[31] T. Rhoadarmer and J. R. P. Angel. Low-cost,broadband static phase plate for generating atmosphericlike turbulence. *Applied Optics*, 40:2946–2955, June 2001.

[32] F. Roddier. Curvature sensing and compensation: a new concept in adaptive optics. *AO*, 27:1223–1225, April 1988.

[33] F. Roddier, M. Northcott, and J. E. Graves. A simple low-order adaptive optics system for near-infrared applications. *PASP*, 103:131–149, January 1991.

[34] J.-F. Sauvage, T. Fusco, C. Petit, S. Meimon, E. Fedrigo, M. Suarez Valles, M. Kasper, N. Hubin, J.-L. Beuzit, J. Charton, A. Costille, P. Rabou, ., D. Mouillet, P. Baudoz, T. Buey, A. Sevin, F. Wildi, and K. Dohlen. SAXO, the eXtreme Adaptive Optics System of SPHERE: overview and calibration procedure. In *Society of Photo-Optical Instrumentation Engineers (SPIE) Conference Series*, volume 7736 of *Society of Photo-Optical Instrumentation Engineers (SPIE) Conference Series*, page 0, July 2010.

[35] R. Soummer, L. Pueyo, and J. Larkin. Detection and Characterization of Exoplanets and Disks Using Projections on Karhunen-Loève Eigenimages. *ApJL*, 755:L28, August 2012.

[36] W. H. F. Talbot. Facts relating to optical science. *Philos. Mag.*, 9:401, 1836.

[37] C. Thalmann, M. Janson, E. Buenzli, T. D. Brandt, J. P. Wisniewski, C. Dominik, J. Carson, M. W. McElwain, T. Currie, G. R. Knapp, A. Moro-Martín, T. Usuda, L. Abe, W. Brandner, S. Egner, M. Feldt, T. Golota, M. Goto, O. Guyon, J. Hashimoto, Y. Hayano, M. Hayashi, S. Hayashi, T. Henning, K. W. Hodapp, M. Ishii, M. Iye, R. Kandori, T. Kudo, N. Kusakabe, M. Kuzuhara, J. Kwon, T. Matsuo, S. Mayama, S. Miyama, J.-I. Morino, T. Nishimura, T.-S. Pyo, E. Serabyn, H. Suto, R. Suzuki, M. Takami, N. Takato, H. Terada, D. Tomono, E. L. Turner, M. Watanabe, T. Yamada, H. Takami, and M. Tamura. Imaging Discovery of the Debris Disk around HIP 79977. *ApJL*, 763:L29, February 2013.

[38] J. T. Trauger and W. A. Traub. A laboratory demonstration of the capability to image an Earth-like extrasolar planet. *Nature*, 446:771–773, April 2007.

[39] A. G. Tyler, P. Merritt, Q. R. Fugate, and J. T. Brennan. Adaptive Optics: Theory and Applications, TR-1424. *Optical Sciences Company, Placentia*, June 1998.

[40] F. Zernike. Beugungstheorie des schneidenver-fahrens und seiner verbesserten form, der phasenkontrastmethode. *Physica*, 1:689–704, May 1934.